

# THESIS TITLE

Pruthvi Mehta

2022

# Contents

<b>1</b>	<b>Introduction</b>	<b>5</b>
1.1	Introduction . . . . .	5
1.1.1	Neutrino Physics . . . . .	5
1.1.2	History of Neutrino Physics . . . . .	5
1.1.3	The Solar Neutrino Problem . . . . .	6
1.1.4	Neutrino Oscillation Theory . . . . .	10
1.1.5	Neutrino-nucleus interactions in Super-Kamiokande Gd . . . . .	13
1.1.6	Supernova Relic Neutrinos . . . . .	18
1.1.7	Physics motivation behind Super-Kamiokande Gadolinium Upgrade	30
<b>2</b>	<b>The Tokai-to-Kamioka experiment</b>	<b>32</b>
2.1	The Tokai-to-Kamioka experiment . . . . .	32
2.1.1	Neutrino beam production . . . . .	33
2.1.2	Near detectors . . . . .	35
<b>3</b>	<b>The Super Kamiokande Detector</b>	<b>43</b>
3.1	The Super-Kamiokande detector . . . . .	43
3.1.1	Background and detector design . . . . .	43
3.1.2	Data aquisition system . . . . .	46
3.2	Event Reconstruction . . . . .	48
3.2.1	Vertex Reconstruction . . . . .	48
3.2.2	Direction Reconstruction . . . . .	49
3.2.3	Energy reconstruction . . . . .	52
3.3	Super-Kamiokande Gadolinium Upgrade . . . . .	53
3.3.1	Americium/Beryllium Calibration . . . . .	54

3.3.2	The EGADS project . . . . .	54
3.3.3	Gadolinium loading into Super-Kamiokande . . . . .	55
<b>4</b>	<b>Super-Kamiokande Detector Calibration</b>	<b>61</b>
4.1	Inner detector calibration . . . . .	61
4.1.1	PMT High-voltage setting calibration . . . . .	61
4.1.2	Relative gain calibration . . . . .	62
4.1.3	Absolute gain calibration . . . . .	63
4.1.4	Relative quantum efficiency measurement . . . . .	65
4.1.5	Timing information calibration . . . . .	67
4.1.6	Measurement of light reflection on the black sheet and the PMTs . . . . .	69
<b>5</b>	<b>The UK Light Injection System</b>	<b>78</b>
5.1	The UK Light Injection System Electronics and Optics . . . . .	78
5.2	Optics test stand measurements . . . . .	80
5.3	First commissioning data from UKLI . . . . .	81
5.4	Implementation of UKLI in SK Simulation . . . . .	88
<b>6</b>	<b>Neutron Tagging and NCQE Interactions with the SK-Gd Upgrade</b>	<b>100</b>
6.1	Event Simulation . . . . .	101
6.1.1	Neutrino flux . . . . .	102
6.1.2	Primary interaction . . . . .	104
6.1.3	Detector response and interactions in the detector medium . . . . .	106
6.2	Event Reconstruction . . . . .	109
6.2.1	Bonsai output reconstruction quantities . . . . .	109
6.2.2	Comparison of BONSAI reconstruction output variables between SKDETSIM versions . . . . .	113
6.2.3	NCQE event selection . . . . .	121
6.2.4	Charged current event (CC) interaction cut . . . . .	125
6.2.5	Prompt event NCQE reduction cut plots . . . . .	125
6.3	Secondary selection . . . . .	129
6.3.1	True neutron tagging information . . . . .	129
6.3.2	Primary selection criteria . . . . .	134
6.3.3	Secondary selection criteria . . . . .	135

<b>7 Systematic uncertainty calculations</b>	<b>152</b>
7.1 Systematic uncertainty calculation methodology . . . . .	152
7.2 Gamma production from neutron capture detector response . . . . .	153
7.3 Neutrino beam flux uncertainty . . . . .	154
7.4 Neutrino cross section uncertainty . . . . .	155
7.5 Pion final state interaction (FSI) and secondary interaction (SI) uncertainties	156
7.6 Nucleon final state interactions . . . . .	159
7.7 Muon and pion capture on Oxygen-16 . . . . .	161
7.8 Nucleon SI . . . . .	164
7.8.1 MICAP uncertainty calculation . . . . .	164
7.8.2 HETC uncertainty calculation . . . . .	166
7.9 Uncertainty due to PMT gain simulation . . . . .	168
7.9.1 Final systematic error . . . . .	169
<b>8 Conclusion</b>	<b>170</b>
<b>A Appendix A</b>	<b>177</b>

# Chapter 1

## Introduction

### 1.1 Introduction

#### 1.1.1 Neutrino Physics

There are a plethora of physics phenomenon in which neutrinos are involved, including beta decay, fusion, and supernovae. As part of the Standard Model, they are described as being Dirac fermions with no electric charge with three flavours: the electron neutrino, the muon neutrino and the tau neutrino, corresponding with their associated leptons: the electron, muon and tauon. Prior to the discovery of neutrino oscillations, it was believed that neutrinos were massless, but they in fact have small but non zero masses ( $\leq 1\text{eV}$ ) [1]. This chapter will discuss a brief history of neutrino physics including the discovery of neutrino oscillations, the manner in which neutrinos interact with nuclei in the Super-Kamiokande detector, and the motivation behind an NCQE neutron tagging analysis.

#### 1.1.2 History of Neutrino Physics

To correct a violation of energy and momentum conservation discovered in beta-decay, Wolfgang Pauli put forward the idea of a neutrino as a solution [2]. He originally named this particle the “neutron”, prior to Chadwick’s discovery of the actual neutron two years later. Enrico Fermi then proposed to call it the neutrino, Italian for “little neutral one”. In 1934, Enrico Fermi’s theory of beta decay stated that a neutron could decay to a proton, electron and an antineutrino and in 1956 [3], Clyde Cowan and Frederick Reines directly confirmed the existence of neutrinos [4], by detecting the electron antineutrino

originating from inverse beta decay produced from nuclear reactor or fission products. In inverse beta decay an electron antineutrino interacts with a proton to produce a neutron and positrons.

These positrons pair-annihilate with electrons and produce two 0.5 MeV gamma rays and scintillator material was placed in a tank of water, which was used to detect the gamma photons, and the scintillator light produced flashes of visible light which were detected by photomultiplier tubes. Cadmium chloride was used to detect the coincident neutron, which after exciting and de-exciting, emits a gamma ray within 5 microseconds after the pair-annihilation gammas are detected. In 1962, Lederman, Schwartz and Steinberger detected the muon neutrino [5]. To discover the muon neutrino, the AGS (Alternating Gradient Synchrotron) at Brookhaven was used - the AGS's beam of protons was used to produce a shower of pions after slamming into a beryllium target. These pions would travel toward a 5,000-ton steel wall (constructed from old battleship plates!) and they would decay into muons and neutrinos, but only neutrinos would be able to pass through the steel wall into a spark chamber filled with neon. As neutrinos coursed through this chamber, one neutrino would occasionally hit a proton in an aluminium nucleus which would produce muon tracks, instead of the showers produced from electrons, proving that there were muon neutrinos in the neutrinos that passed through the chamber.

In 2000 the DONUT collaboration (Direct Observation of NU Tau) at Fermilab detected the existence of the tau neutrino [6]. A beam of neutrinos (which they expected to contain tau neutrinos) was fired at iron plates with alternating layers of emulsion, and very very small number of these tau neutrinos interacted with an iron nucleus to produce the tau lepton, which decayed leaving a track in the emulsion. These tracks contained a kink, which were a sign of the tau neutrino, and only four such tracks were detected out of a possible six million.

### 1.1.3 The Solar Neutrino Problem

The Standard Solar Model predicts that most of the solar neutrino flux (about 90%) come from the proton-proton chain reaction, where the solar neutrinos produced have energies below 0.4 MeV. Figure 1.1 shows the processes which make up the pp chain, along with the branching percentages where it produces a neutrino.

Only experiments that use Gallium can detect neutrinos with this energy, whereas ex-



Figure 1.1: Proton-proton chain cycle with branching percentages shown



Figure 1.2: Solar neutrino fluxes predicted by Bachall's Standard Solar Model, and which experiments are able to detect them. [7]

periments whose detector medium is Chlorine can observe neutrinos from  $^7\text{Be}$  (production equation of which is shown in Figure 1.1). Experiments whose detector medium is water (such as Super-Kamiokande and SNO) can only see the  $^8\text{B}$  neutrinos, as shown in Figure 1.2.

In the 1960s, the Homestake experiment made the first measurement of solar electron neutrino flux [8]. The experiment used a perchloroethylene-based detector, placed 1,478 metres underground in the Homestake Gold Mine in South Dakota. When an electron neutrino interacts with  $^{37}\text{Cl}$  in the perchloroethylene, the  $^{37}\text{Cl}$  becomes a radioactive isotope of  $^{37}\text{Ar}$  which is extracted by bubbling helium through the tank, and then counted in order to determine how many neutrinos had been captured. The theoretical solar neutrino flux calculated by John Bachall was about three times as much as Raymond Davis' results from the experiment: with Bachall's calculations predicting a solar neutrino flux of  $8.1 \pm 1.2$

SNU, whereas the Homestake experimental results showed a flux of  $2.56 \pm 0.25$  SNU. These results were consistent with those from the subsequent Kamiokande, SAGE and GALLEX experiments. Super-Kamiokande's main detection channel for solar neutrinos is the elastic-scattering channel, which has a minimum energy threshold value (recoil electron kinetic energy) of 5 MeV. In this channel, Super-Kamiokande observed a solar neutrino capture rate of  $0.45 \pm 0.02$  SNU, while the solar neutrino model prediction was  $1.0 \pm 0.2$  SNU. Turning our attention to the results of the Gallium experiments, namely SAGE and GALLEX, they also showed a discrepancy regarding the solar model predictions. Due to their sensitivity to the bulk of the proton-proton chain neutrino flux, they have a larger solar neutrino capture flux rate, with SAGE observing  $70.8 \pm 5.0$  SNU, and GALLEX observing  $77.5 \pm 8.0$  SNU, while the model prediction was  $129 \pm 9.0$  SNU, a difference of about 40%. This discrepancy of experimental results compared with the Standard Solar Model prediction became known as the Solar Neutrino Problem.

The way to combat this discrepancy and prove that the cause of the Solar Neutrino Problem was neutrino oscillations was finding a way to detect solar neutrino flux which was not dependent on neutrino flavour. Due to these experiments only detecting solar neutrinos through charged current interactions, they wouldn't be able to detect muon or tau neutrinos. However, with the Sudbury Neutrino Observatory (SNO) experiment this would change, as SNO used heavy water  $D_2O$  as its detector medium. Deuteron consists of a proton and a neutron and due to how little energy it takes to break it apart (2.2 MeV), an electron, muon or tau neutrino can very easily break it apart, so that SNO can detect the final state neutron then muon and tau neutrinos would be visible to the detector. The three main channels SNO uses to detect neutrinos is the elastic scattering channel, the charged current channel, and the neutral current channel. Elastic scattering allows SNO to see muon and tau neutrino flux given by  $\phi(\nu_e + 0.15(\phi(\nu_\mu) + (\nu_\tau)))$ . The most important neutrino interaction channel regarding SNO being able to measure the muon and tau neutrino flux is the neutral current (NC) channel (shown in Equation 1.1), as it allows SNO to measure the total flux.

$$\nu + d \rightarrow n + p + \nu \quad (1.1)$$

Using these two reaction channels, along with the charged current channel (CC), which can only measure electron neutrino flux, SNO was able to measure the individual neutrino flavour fluxes, shown in Equation 1.2.

$$\begin{aligned}\phi_{CC} &= \phi(\nu_e) = 1.76 \pm 0.0110^{-8} \text{ cm}^{-2} \text{ s}^{-1} \\ \phi_{ES} &= \phi(\nu_e) + 0.15(\phi(\nu_\mu) + \phi(\nu_\tau)) = 2.39 \pm 0.2610^{-8} \text{ cm}^{-2} \text{ s}^{-1} \\ \phi_{NC} &= \phi(\nu_e) + \phi(\nu_\mu) + \phi(\nu_\tau) = 5.09 \pm 0.6310^{-8} \text{ cm}^{-2} \text{ s}^{-1}\end{aligned}\tag{1.2}$$

From Equation 1.2, you can see that the flux of muon and tau neutrinos from the Sun is  $\phi(\nu_\mu) + \phi(\nu_\tau) - \phi(\nu_e) = 3.33 \pm 0.62$ , which is 3 times that of the value for  $\phi(\nu_e)$ , and as we know that the Sun only produces  $\nu_e$ , it means that the neutrinos must be changing flavour to mu and tau neutrinos on their journey to Earth, definitely solving the solar neutrino problem.

#### 1.1.4 Neutrino Oscillation Theory

In 1957, Bruno Pontecorvo postulated that neutrinos could transition from neutrinos to antineutrinos and vice versa (similarly to how two kinds of neutral kaons  $\bar{K}_0$ , and  $K_0$  were found to oscillate) [9]. Neutrino flavour oscillation theory was then developed by Maki, Nakagawa and Sakata in 1962. The PMNS matrix (Pontecorvo-Maki-Nakagawa-Sakata matrix) is the neutrino analogue of the Cabibbo-Kobayashi-Masakawa quark mixing matrix [10], and is shown in Equation 1.3 as  $(U_{\alpha i}^*)$  which shows the relationship between the mass and flavour eigenstates for a neutrino with a definite flavour of  $\alpha$  and a definite mass of  $m_i$ .

$$\begin{aligned}|\nu_\alpha\rangle &= \sum_i U_{\alpha i}^* |\nu_i\rangle \\ |\nu_i\rangle &= \sum_\alpha U_{\alpha i} |\nu_\alpha\rangle\end{aligned}\tag{1.3}$$

In Equation 1.3, the terms  $U_{\alpha i}^*$  and  $U_{\alpha i}$  are the complex conjugate and normal PMNS matrix. Equation 1.4 shows the 3x3 form of the PMNS matrix, where  $c_{ij} = \cos\theta_{ij}$  and  $s_{ij} = \sin\theta_{ij}$ .

$$\begin{aligned}
U &= \begin{pmatrix} 1 & 0 & 0 \\ 0 & c_{23} & s_{23} \\ 0 & -s_{23} & c_{23} \end{pmatrix} \begin{pmatrix} c_{13} & 0 & s_{13}e^{-i\delta_{CP}} \\ 0 & 1 & 0 \\ -s_{13}e^{i\delta_{CP}} & 0 & c_{13} \end{pmatrix} \begin{pmatrix} c_{12} & s_{12} & 0 \\ -s_{12} & c_{12} & 0 \\ 0 & 0 & 1 \end{pmatrix} \quad (1.4) \\
&= \begin{pmatrix} c_{12}s_{13} & s_{12}c_{13} & s_{13}e^{-i\delta_{CP}} \\ -s_{12}c_{23} - c_{12}s_{13}s_{23}e^{i\delta_{CP}} & c_{12}c_{23} - s_{12}s_{13}s_{23}e^{i\delta_{CP}} & c_{13}s_{23} \\ s_{12}s_{23} - c_{12}s_{13}c_{23}e^{i\delta_{CP}} & c_{12}s_{23} - s_{12}s_{13}c_{23}e^{i\delta_{CP}} & c_{13}c_{23} \end{pmatrix}
\end{aligned}$$

In Equation 1.4, if the  $\sin \delta_{CP}$  terms are not equal to 0, it means that there will be imaginary terms in the matrix, which will contribute to CP (charge-parity) violation. The angles  $\theta_{12}$ ,  $\theta_{23}$  and  $\theta_{13}$  are mixing angles.

### Two-flavour neutrino oscillations in vacuum

If a neutrino is produced in the flavour state  $|\nu_\alpha\rangle$  in a vacuum, using the PMNS matrix for the relationship between the mass eigenstate and the flavour eigenstate, propagating the neutrino according to the time-dependent Schrodinger equation with no potential would yield a solution to this equation as a plane wave, shown in Equation 1.5.

$$i\frac{\partial}{\partial t} |\nu_i(x, t)\rangle = E |\nu_i(x, t)\rangle = -\frac{1}{2m_i} \frac{\partial^2}{\partial x^2} |\nu_i(x, t)\rangle \quad (1.5)$$

The solution to Equation 1.5 is a plane wave of the form shown in Equation 1.6.

$$|\nu_k(x, t)\rangle = e^{-i(E_k t - p_k x)} |\nu_k(0, 0)\rangle = e^{-i\phi_k} |\nu_k(0, 0)\rangle \quad (1.6)$$

The probability of oscillation to flavour state  $|\nu_\beta\rangle$  at time  $t$  is given by Equation 1.7.

$$\begin{aligned}
P(\nu_\alpha \rightarrow \nu_\beta) &= |\langle \nu_\beta | \nu_\alpha(t) \rangle|^2 \quad (1.7) \\
&= \sum_{i,j} (U_{\beta i}^*)(U_{\beta i})(U_{\alpha j})(U_{\beta j}^*) e^{-i(E_i - E_j)t}
\end{aligned}$$

For a two-flavour oscillation probability calculation, the matrix which transforms a vector in flavour basis into mass basis is simply a 2x2 rotation matrix (where  $\theta$  is the mixing angle) so that:

$$\begin{pmatrix} \nu_\alpha \\ \nu_\beta \end{pmatrix} = \begin{pmatrix} \cos \theta & \sin \theta \\ -\sin \theta & \cos \theta \end{pmatrix} \begin{pmatrix} \nu_1 \\ \nu_2 \end{pmatrix}$$

One could calculate the probability of a neutrino of flavour  $\alpha$  oscillating into a neutrino of flavour  $\beta$  by using the formula in Equation 1.8. Here  $L$  is the distance travelled by the neutrino in kilometres,  $\Delta m^2$  is the difference between the mass eigenstates, and  $E$  is the difference between the energy of the mass eigenstates (where an assumption has been made that the mass eigenstates are the same for both.) The survival probability of a neutrino of flavour  $\alpha$  (i.e. the probability of generating  $\nu_\alpha$  and detecting  $\nu_\alpha$ ) is  $P(\nu_\alpha \rightarrow \nu_\alpha) = 1 - P(\nu_\alpha \rightarrow \nu_\beta)$  for two flavour oscillations.

$$P(\nu_\alpha \rightarrow \nu_\beta) = \sin^2(2\theta) \sin^2\left(1.27\Delta m^2 \frac{L}{E_\nu}\right) \quad (1.8)$$

### Neutrino oscillation matter effects

The presence of dense matter affects the vacuum neutrino oscillation probability, since neutrinos interact via the weak interaction with matter. This is called the Mikheyev-Smirnov-Wolfenstein (MSW) effect: due to ordinary matter containing only electrons, and muons and tauons, the charge current interactions only affects electron neutrinos and creates an additional potential which affects the vacuum oscillation probability for electron neutrinos, shown in Equation 1.9, where  $G_F$  is the Fermi coupling constant, and  $n_e$  is the number density of electrons in the matter, where the positive sign applies to neutrinos, and the negative sign applies to anti-neutrinos.

$$V_{CC} = \pm \sqrt{2} G_F n_e \quad (1.9)$$

Replacing  $\Delta m^2$  with  $\Delta m_M^2$  and  $\sin^2 \theta$  with  $\sin^2 \theta_M$  gives the two flavour oscillation probability modified to take into affect the MSW effect (shown in Equation 1.10, where the factor of  $A = 2|V_{CC}|E$ ).

$$\begin{aligned} \sin 2\theta_M &= \frac{\sin 2\theta}{\sqrt{\sin^2 2\theta + (\cos 2\theta - A/\Delta m^2)^2}} \\ \Delta m_M^2 &= \Delta m^2 \sqrt{\sin^2 2\theta + (\cos 2\theta - A/\Delta m^2)^2} \end{aligned} \quad (1.10)$$



Figure 1.3: Feynman diagrams of charged-current (left) and neutral-current (right) neutrino interactions

### 1.1.5 Neutrino-nucleus interactions in Super-Kamiokande Gd

Understanding neutrino interaction modes, and understanding neutrino nucleus interaction modes, in particular the neutral current quasielastic reaction is key to understanding this analysis.

There are two main types of neutrino interaction: charged-current (CC) and neutral current (NC). The former occurs when a  $W^\pm$  boson is involved in a nuclear exchange, and the latter occurs when a  $Z^0$  is involved (see Figure 1.3).

One such interaction, and often the simplest interaction, is neutrino-electron elastic scattering ( $\nu + e^- \rightarrow \nu + e^-$ ), which occurs when a neutrino scatters off an electron with a virtual vector boson being exchanged. This type of scattering is used in the detection of low energy neutrinos, primarily those from the sun. Figure 1.4 shows the Feynman diagrams for this kind of interaction.

There are multiple types of neutrino-nucleus interactions that occur which can be either charged current or neutral current interactions. These are given in order of momentum transfer ( $q^2$ ), with the lowest neutrino energies producing quasi-elastic scattering for charged current interactions, and elastic scattering for neutral current interactions, up to deep inelastic scattering where the target nucleus breaks up.

Starting off with the neutrino-nucleus interaction with the lowest  $q^2$ , the Feynman diagrams for NC elastic and CCQE interactions by a muon neutrino interacting with a neutron are shown in Figure 1.5.

The type of interaction that occurs at higher neutrino energies, i.e. with more  $q^2$  avail-



Figure 1.4: Feynman diagrams of neutral-current (left) and charged-current (right) neutrino-electron scattering



Figure 1.5: Feynman diagram for  $\nu_\mu$  NC elastic scattering (left) and  $\nu_\mu$  CCQE scattering (right)

able is resonance production. Single mesons can also be produced via neutrino-nucleon reactions: these are mostly pions, but some kaons and eta particles can also be produced. Here a neutrino with a high enough energy interacts with and excites a nucleon, producing a resonant baryon which decays to a nucleon and a single pion (shown in Equation 1.11), where  $N$  and  $N'$  are nucleons.

$$\begin{aligned} \nu_l + N &\rightarrow l + N^* \\ N^* &\rightarrow \pi + N' \end{aligned} \tag{1.11}$$

The resonant baryon produced during the reaction is usually a  $\Delta(1232)$  resonance. Single pion final states can also be produced by a neutrino which scatters off an entire nucleus ( $X$ ), shown in Equation 1.12 for the charged current reactions and Equation 1.13 for neutral current reactions.

$$\nu_l + X \rightarrow l^- + X + \pi^+, \quad \bar{\nu}_l + X \rightarrow l^+ + X + \pi^- \tag{1.12}$$

$$\nu_l + X \rightarrow \nu_l + X + \pi^0, \quad \bar{\nu}_l + X \rightarrow \bar{\nu}_l + X + \pi^0 \tag{1.13}$$

At higher energies (above 1 GeV), neutrino interactions can also produce kaons in the final state, due to the higher energies being able to produce strange quarks.

At even higher energies and greater  $q^2$ , deep inelastic scattering is able to occur. Deep inelastic scattering is a type of neutrino interaction where the neutrino scatters off a quark inside the proton or neutron involved in the exchange, via a W (CC) or Z (NC) boson (Equation 1.14), shown in Figure 1.6.

$$\begin{aligned} \nu_l + N &\rightarrow l^- + X, \quad \bar{\nu}_l + N \rightarrow l^+ + X(\text{CC}) \\ \nu_l + N &\rightarrow \nu_l + X, \quad \bar{\nu}_l + N \rightarrow \bar{\nu}_l + X(\text{NC}) \end{aligned} \tag{1.14}$$

The next two neutrino-nucleus interactions explained here are of particular relevance to the analysis in this thesis: inverse beta decay (IBD) and quasi-elastic scattering.

Inverse beta decay is the reaction by which Cowan and Reines first detected electron antineutrinos: it is important at low energies: from the minimum energy for the reaction

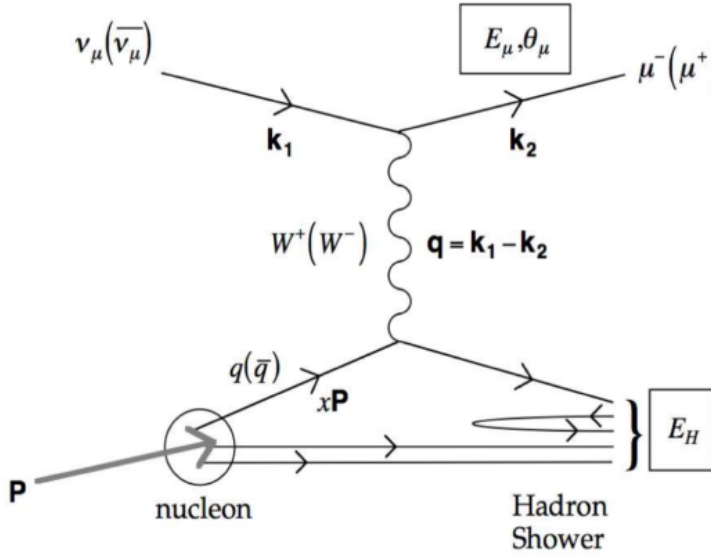


Figure 1.6: Feynman diagram for a charged current deep inelastic scattering interaction with an incoming muon neutrino

to take place ( $E_\nu = 1.806$  MeV) to tens of MeV. Diffuse Supernova Neutrino Background and low energy antineutrinos produced from nuclear reactors can be detected via this process. Figure 1.7 shows the Feynman diagram for this reaction. The neutron produced by this reaction is integral to the motivation behind the Gadolinium-doping upgrade to Super-Kamiokande, which will be explained in the next section.

Finally, we get to the type of interaction investigated in this thesis: quasi-elastic scattering. This makes up the majority of the neutrino-nucleus interaction cross-sections at the energy range from 100 MeV to 2 GeV, and therefore vital for the study of neutrinos from long baseline neutrino experiments and also low energy atmospheric neutrinos. Equation 1.15 shows the equations for both the charge current (CCQE) and neutral current (NCQE) version of this interaction where the incoming neutrino scatters off a nucleon.

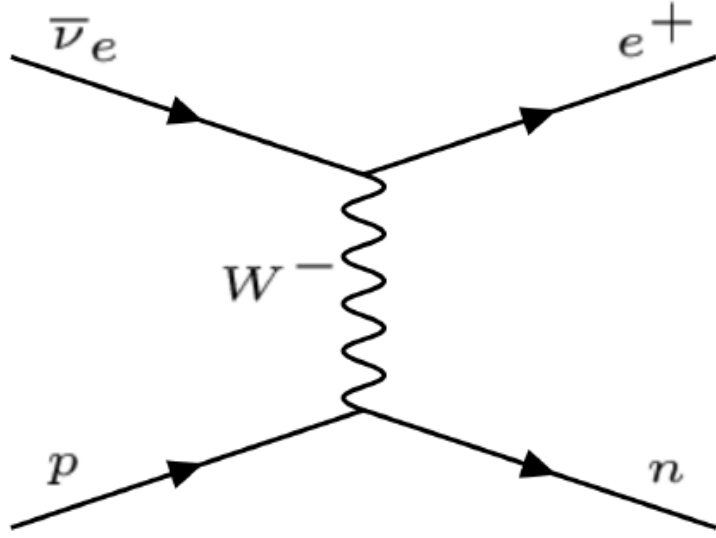


Figure 1.7: Feynman diagram for the inverse beta decay reaction

$$\text{CC} : \nu(k) + n(p) \rightarrow l^-(k') + p(p') \quad (1.15)$$

$$\bar{\nu}(k) + p(p) \rightarrow l^+(k') + n(p')$$

$$\text{NC} : \nu(k) + N(p) \rightarrow \nu(k') + N(p')$$

$$\bar{\nu}(k) + N(p) \rightarrow \bar{\nu}(k') + N(p')$$

As this analysis relates to the various properties of neutrons produced from NCQE interactions in Super-Kamiokande Gd, it is worth looking at the interactions where neutrons are produced inside the detector medium. In Water Cherenkov detectors, the incoming neutrino or anti-neutrino interacts with an  $^{16}\text{O}$  nucleus, and at neutrino energies greater than 200 MeV, a nucleon is knocked out, as shown in Equation 1.16.





Figure 1.8: Feynman diagram for a quasi elastic scattering interaction off a nucleon

This interaction happens in stages, where there is the initial reaction between the incoming neutrino and the specific nucleon inside the  $^{16}\text{O}$  nucleus, hadronic final state interactions (FSI) inside the nucleus itself, and subsequent hadronic secondary interactions (SI) inside the detector medium. These are outlined in the schematic shown in Figure 1.9, with the primary interaction, taken as the CCQE reaction ( $\bar{\nu}(k) + p(p) \rightarrow l^+(k') + n(p')$ ). There are stages to neutrino-nucleus reactions, and for the CCQE reaction shown in Figure 1.9, there are three processes: the initial neutrino-nucleon reaction ( $\bar{\nu}(k) + p(p) \rightarrow l^+(k') + n(p')$ ), the final state interaction (FSI) inside the  $^{16}\text{O}$  nucleus ( $p + p \rightarrow p + n + \pi^+$ ), and the secondary (SI) interaction in the detector medium ( $n + ^{16}\text{O} \rightarrow n + n + ^{15}\text{O}^*$ ). All interactions inside the nucleus are referred to as hadronic final state interactions, and when they move through the detector medium and leave the target nucleus they are known as hadronic secondary interactions.

### 1.1.6 Supernova Relic Neutrinos

A key feature of the analysis presented in this thesis is that it is an investigation into the significant background of the signal for SRN. It is therefore important to state and understand the process behind the production of supernova relic neutrinos in order to get a firm handle on the motivation behind this analysis.



Figure 1.9: Schematic of neutron production following the interaction of neutrino with a nucleon inside an  $^{16}\text{O}$  and the resulting FSI and SI interactions in the detector medium.

## Supernovae Classification

Supernovae occur when a star with a mass around eight times the mass of our sun explodes, and in a galaxy these occur only a few times in a century. Supernovae are classified into different types: Type 1a, Type 1b, Type 1c and Type II. The classification of supernovae are determined by looking at the spectral lines in the light emitted from these supernovae. Table 1.1.6 shows how these supernovae are classed and which spectral line elements are associated with each class.

Supernova Classification	Element lines present in spectra
Type 1a	No hydrogen, silicon
Type 1b	No hydrogen, no silicon, helium
Type 1c	No hydrogen, no silicon, no helium
Type II	Hydrogen

The kinetic energy of a supernova is  $10^{44}$  J, and 99 % of the energy from core-collapse supernovae (CCSN) are released in the form of neutrinos. Unlike Type 1a supernovae which are usually thermonuclear supernovae, Type 1b, Type 1c and Type II are core-collapse supernovae, from which more neutrinos are emitted which is why these types of supernovae are of more interest.

## Core-Collapse Supernovae Mechanism

Using the pressure produced by the process of nuclear fusion, a star is able to support itself against gravitational collapse. During the proton-proton chain reaction, hydrogen will fuse to produce helium and once temperatures and pressures are high enough, helium fusion will occur. After all the helium in the core is used up in the fusion process, the star will contract until the pressure and temperatures get even higher, allowing more massive nuclei to fuse. This reaction will carry on until iron nuclei are produced, this being the element with the highest binding energy, causing the fusion to stop.

As more and more iron accumulates in the core of the star, the density and temperature of the core will increase, and these higher energy electrons will increase the rate of electron capture on protons that will occur in the iron nuclei. This will cause a reduction in the electron degeneracy pressure, which is further enhanced by the breakdown of the iron nuclei which occurs at higher temperatures when gamma rays interact with them. The degeneracy pressure is no longer greater than the gravitational forces acting inwards, and gravitational



Figure 1.10: Schematic showing core collapse of a star, and the resultant shockwave and neutrino production

core collapse occurs.

The point at which in the core the neutrino mean free paths become approximately the same size as the proto-neutron star is called the “neutrinosphere”. Figure 1.10 shows the formation of a proto-neutron star (PNS) and the neutrino flux and neutrinosphere produced by the core-collapse mechanism.

The radius of the neutrinosphere becomes as large as that of the inner core of the star, when the inner core of the star reaches a density of  $10^{11} \text{ g cm}^{-3}$ , and the electron neutrinos produced from electron capture become unable to escape. Gravitational collapse of the star continues until the inner core reaches nuclear density, at which point a shock wave is produced due to the repulsive force between nuclei.

When this shock wave reaches the neutrinosphere, neutrino emission begins, which lasts less than 10 milliseconds. After this shockwave passes, nucleons and electrons fall back onto the proto-neutron star which heats it up. This causes neutrinos of all flavours to be

produced via pair production and electron capture. This is called the “accretion phase”. Due to this expulsion of neutrinos the shock wave loses energy, but it is revived through matter behind the shock wave being heated by neutrino absorption from the proto-neutron star region. The mechanism for this shown in Figure 1.11, where the shockwave produced depends on antineutrinos being absorbed by the dense post-shock gas.

After the shock wave is revived, if it has enough energy to blow off the outer layer of matter a supernova occurs. Then, depending on the mass of the PNS, it cools to either become a neutron star or a black hole. If the shock wave energy is not high enough to blow off the outer layer of matter, the accretion phase continues until a black hole is formed.

The energy of the emitted neutrinos depend on their flavour - neutrinos emitted from a deeper layer inside the supernova will be higher in temperature and therefore have a higher energy. For electron neutrinos and electron anti-neutrinos, the dominant interactions are charged current interactions with nucleons. Due to the number of neutrons in a proto-neutron star greatly outnumbering the number of protons, the interaction involving  $\nu_e$  will be far more efficient than those involving  $\bar{\nu}_e$ , meaning the neutrinosphere for  $\bar{\nu}_e$  is smaller than for  $\nu_e$ , so they are emitted from the PNS with greater energies.

Due to there being no charged current interactions involving muon neutrinos in the medium, they are involved instead in neutral current reactions, including Bremsstrahlung, neutrino-pair annihilation, and electron-positron pair annihilation. Due to only undergoing these reactions their neutrinosphere is even smaller than that of their electron neutrino and electron anti-neutrino counterparts, therefore being emitted with even higher energies [11]. Figure 1.12 shows the luminosity (top panels) and average energy (bottom panels) for three different neutrino flavours as a function of time for the neutronisation phase (left), accretion phase (centre) and cooling phase (right). Taken from [12].

Kamiokande-II observed neutrinos produced from a supernova, later named 1987A, in the Large Magellenic Cloud. These neutrinos were also observed by the Baskan Neutrino Observatory and the Irvine-Michigan-Brookhaven detector (IMB) [13]. The neutrinos detected from 1987A were detected via the inverse beta decay (IBD) interaction (shown in Figure 1.7), as opposed to the electron elastic scattering, CC interaction with  $^{16}\text{O}$  or NC interaction with  $^{16}\text{O}$  channels. The positron from this reaction is what is searched for, and these positrons are produced isotropically within the detector. A neutrino burst search from SN1987A was carried out on the data run which ran continuously between 16:09 21

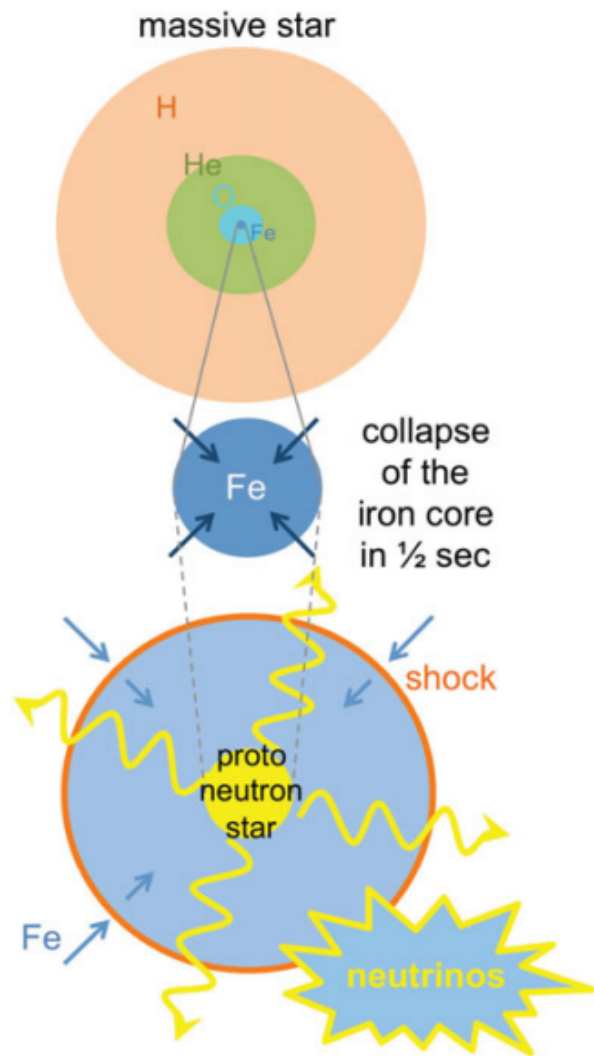


Figure 1.11: Schematic showing core collapse of a star, and the resultant shockwave and neutrino production

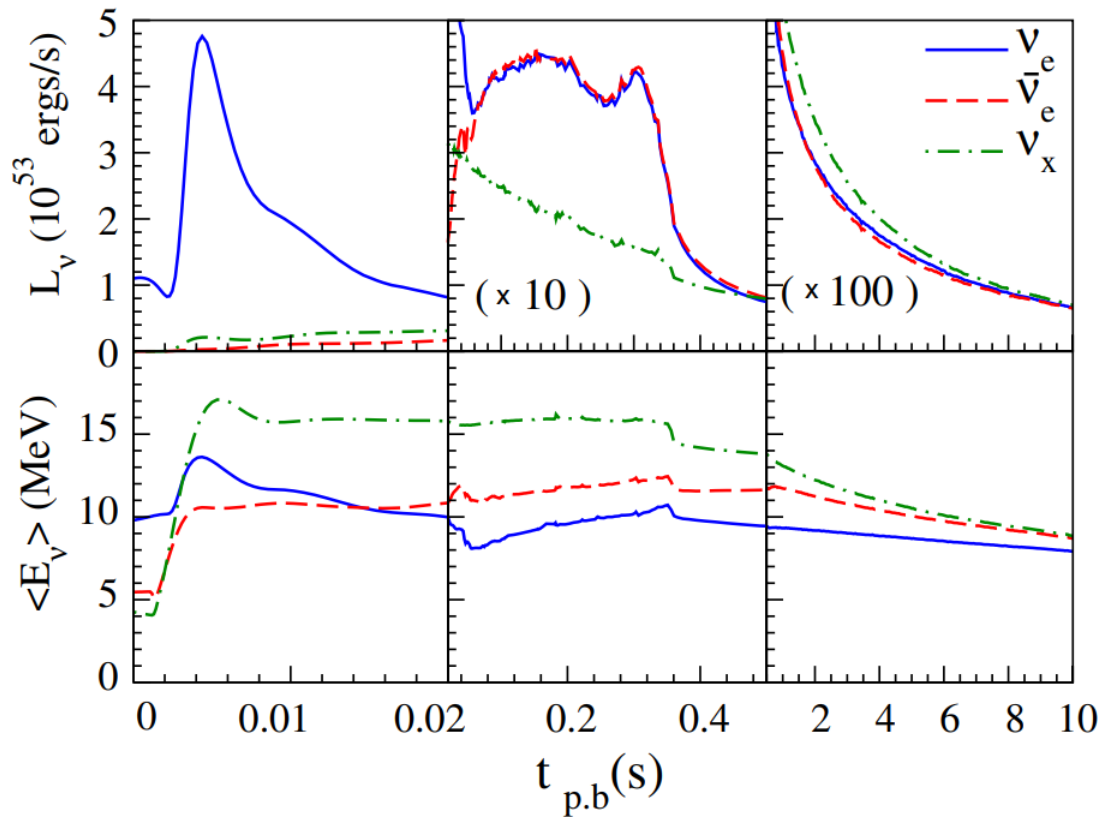


Figure 1.12: Luminosity (top panels) and average energy (bottom panels) for three different neutrino flavours as a function of time for the neutronisation phase (left), accretion phase (centre) and cooling phase (right). Taken from [12].

February 1987 to 07:31 24th February 1987 JST [14].

The event selection criteria for a supernova neutrino event were as follows: firstly, the total number of photoelectrons per event should be less than 170, as this corresponds to an electron with an energy of 50 MeV, and the neutrinos released from a supernovae have a typical energy of the order of 10 MeV. Secondly, the total number of electrons in the outer detector per event needed to be less than 30, in order for the event to be considered fully contained, and finally, the time between previous events has to be greater than 20  $\mu$ sec, in order to avoid electrons produced from Michel electrons. Figure 1.13 shows the time-sequence of all low-energy events. If the neutrinos were to show up in Kamiokande-II, they would arrive in a cluster lasting of order 10s, so intervals of 10 seconds were used to search for clusters of events. In order to classify the event as a supernova neutrino candidate, the event had to be registered by atleast 30 PMTs, and 6 events were found in the first 10s interval which satisfied this, and 2 events in the next 10s interval. A second search was performed on a larger data sample of 42.9 days, from 9th of January to 25th of February 1987, and no other supernova neutrino burst candidates were found. The first two events shown in Figure 1.13 also correlate in angle to the direction of 1987A. As a result, this was considered detection of a genuine supernova neutrino burst, and was the first direct observation of this in neutrino astronomy.

Due to neutrinos carrying away 99% of the energy produced by supernovae, they are the most important signal a supernova can produce, and can be used for finding out when the supernova explosion actually happened - due to neutrinos leaving the supernovae immediately while gamma rays from the the explosion can only leave the supernova when the shock wave reaches the surface of the star [15].

The supernova relic neutrinos emitted from all past CCSN are accumulated and form an everpresent background due to the fact that neutrinos only weakly interact with matter. The total flux of this neutrino background has been theoretically predicted and is called the “diffuse supernova neutrino background” (DSNB). When calculating the total DSNB flux, the redshift caused by the expansion of the universe needs to be taken into account.

Equation 1.17 gives the differential of the DSNB flux with respect to the DSNB energy at Earth.

$$dn_\nu(E_\nu) = R_{\text{SN}}(z) \frac{dt}{dz} dz \frac{dN_\nu(E'_\nu)}{dE'_\nu} (1+z)dE_\nu \quad (1.17)$$

Here  $E'_\nu = (1+z)E_\nu$  is the energy of neutrinos at a certain redshift  $z$ ,  $R_{\text{SN}}(z)$  is the



Figure 1.13: Events detected centered on 16:35:35 JST, where the solid lines are the number of hit PMTs and dashed lines are muon events. The zoomed in plot in the top-right shows an expanded version of the 0.0 - 2.0 second time scale.

supernova rate at a comoving volume at  $z$ ,  $dN_\nu/dE_\nu$  is the number spectrum of neutrinos emitted by one supernova explosion, and  $(1+z)^{-3}$  is the expansion of the universe factor. The relationship between redshift and time ( $dt/dz$ ), is given by the Friedmann equation (Equation 1.18), where  $H_0$  is the Hubble constant,  $\Omega_m$  is the matter density and  $\Omega_\Lambda$  is the cosmological constant [16].

$$\frac{dz}{dt} = -H_0(1+z)\sqrt{\Omega_m(1+z)^3 + \Omega_\Lambda} \quad (1.18)$$

It is worth reviewing the lastest searches from Super-Kamiokande for DSNB neutrinos, and the limit on the flux prediction from different Super-Kamiokande phases. While Figure 1.14 shows that the majority of DSNB neutrinos have an energy below 10 MeV, due to massive backgrounds these DSNB are hard to detect, so Super-Kamiokande therefore searches for the DSNB signal in the order of 10 MeV. As mentioned previously the main detection channel is inverse-beta decay, with the prompt signal being the emitted positron and the delayed signal constituting of the photon emission from neutron capture. Up to and including now, there has been no DSNB signal evidence but upper-limits on the flux have been set from both KamLAND and from Super-Kamiokande phases I-IV, shown in Figure 1.15.

Regarding important backgrounds to the DSNB signal, below neutrino energies of 15 MeV NCQE interactions from atmospheric neutrinos form the main background to DSNB searches. The importance of this background motivates the analysis in this thesis: by measuring the NCQE interaction using T2K beam neutrinos, the large uncertainty of this interaction in the low energy region can be reduced due to the reason that the atmospheric neutrino energy region is similar to that of the T2K beam energy region. The differential cross section of the neutral-current elastic interaction of a neutrino on a free proton or neutron can be written as shown in Equation 1.19.

$$\frac{d\sigma^{\nu(\bar{\nu})}}{dq^2} = \frac{M^2 G_F^2}{8\pi E_\nu^2} \left\{ A(q^2) \pm B(q^2) \frac{s-u}{M^2} + C(q^2) \frac{(s-u)^2}{M^4} \right\} \quad (1.19)$$

where  $E_\nu$  is the initial neutrino or antineutrino energy,  $M$  is the mass of the nucleon,  $G_F$  is the Fermi coupling constant,  $s$  and  $u$  are the Mandelstam variables, and  $q$  is the transfer of four momentum between between incoming (anti)neutrinos and outgoing (anti)neutrinos. Depending on whether it is an incoming neutrino or antineutrino, there is either a plus or a minus between the A and B terms. A,B and C are terms which are

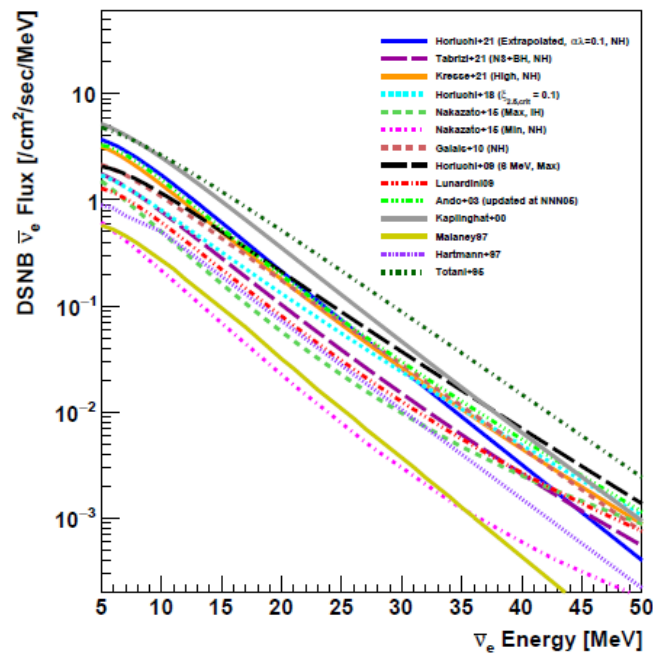


Figure 1.14: DSNB flux against neutrino energy for various theoretical models, "NH" and "IH" are the normal and inverted mass hierarchies respectively



Figure 1.15: The 90% C.L. for observed and expected upper limits on the electron antineutrino flux from SK-I - SK-IV and KamLAND, with the theoretical predictions in Figure 1.14 shown in grey.



Figure 1.16: Schematic showing the IBD and NCQE interaction mechanisms

made up of form factors specific to neutral current interactions.

### 1.1.7 Physics motivation behind Super-Kamiokande Gadolinium Upgrade

Due to the large cross section of the IBD interaction, IBD events constitute about 88% of the total number of events in the detector [17]. With efficient neutron tagging in Super-Kamiokande, the backgrounds (charged current interactions and muon spallation) in the search for SRN flux neutrinos would be largely reduced. The neutral current quasielastic (NCQE) background would still remain due to the way the gamma rays arising from neutron capture mimic the signal of the inverse beta decay (IBD) reactions: a schematic of both NCQE and IBD reactions are shown in Figure 1.16. The measurement of the NCQE interactions using T2K beam flux can aid in understanding this background more due to the T2K flux peak being near the atmospheric neutrino flux peak ( 600 MeV).

Efficient neutron tagging aids information about neutrino energy and neutrino interaction type, and when it comes to studying atmospheric neutrino oscillations, accurate neutrino energy reconstruction is particularly important. Figure 1.17 shows the fraction of non-visible energy as a function of the number of tagged neutrons from simulations of atmospheric neutrino interactions at Super-Kamiokande. Here  $E_\nu$  is the energy of the atmospheric neutrino and  $E_{vis}$  is the energy that is reconstructed from charged particles. Due to these neutrinos interacting with nuclei in the detector, more neutrons are



Figure 1.17: MC study of (a) neutron multiplicity production for  $\nu$  and  $\bar{\nu}$ , (b) neutral current, charged current and deep and non-deep inelastic scattering, (c) the correction to the visible energy as a function of neutrino multiplicity. Taken from [17].

produced, and with efficient neutron tagging on gadolinium the neutrino energy can be properly reconstructed.

The ideal goal of this analysis is to complement prior analyses which investigate the NCQE cross-section and analyses which produce neutron multiplicity distributions for NCQE interactions, with the added benefit of comparisons to Run 11 T2K data, which brings with it the first beam events with gadolinium in the far detector. The emphasis on the distributions of neutrons in this thesis and the methods of neutron tagging used are of increasing interest due to the fact that the main purpose behind adding Gadolinium to the detector is to make these neutron captures more visible.

# Chapter 2

## The Tokai-to-Kamioka experiment

### 2.1 The Tokai-to-Kamioka experiment

The Tokai-to-Kamioka (T2K) experiment is a long baseline neutrino oscillation experiment based in Japan and its purpose is to study neutrino oscillations: specifically a precision measurement of the neutrino oscillation parameters  $\Delta m_{23}^2$  and  $\sin^2 \theta_{23}$  and to improve the measurement of the leptonic CP violating phase  $\delta_{CP}$ , which is mentioned in Chapter 1. The experiment produces a beam of intense anti-muon neutrinos at J-PARC (Japan Proton Accelerator Research Complex) in Tokai, which is located on the east coast of Japan in Ibaraki Prefecture. The muon neutrino beam travels 295 km west towards the far detector Super-Kamiokande (see Chapter 3.) The neutrino beam is measured by other detectors such as ND280 and INGRID, prior to reaching Super-Kamiokande which is important with regards to measuring the neutrino oscillation parameters. Both ND280 and Super-Kamiokande are off-axis detectors, meaning that they are located  $2.5^\circ$  off axis from the centre of the neutrino beam. This results in the peak of the energy of the muon neutrinos to be 0.6 GeV, maximising the neutrino oscillation on the 295 km baseline. This chapter explains production of the muon neutrino beam from the JPARC proton beam line and the near detector complex.

### 2.1.1 Neutrino beam production

#### JPARC proton beam production

A sequence of three accelerators results in the production of a proton beam from the JPARC accelerator complex, these are the LINAC (linear accelerator), the RCS (rapid cyclic synchrotron) and the main ring synchrotron (MR). A negative hydrogen ion is accelerated to a kinetic energy of 400 MeV by a linear accelerator (LINAC), from which a beam of protons is created by converting the negative hydrogen ion beam using charge-stripping foils. This proton beam is then accelerated to a kinetic energy of 3 GeV by the RCS, and about 5% of the bunches produced from this process are passed to the MR where the proton beam will be accelerated up to 30 GeV. The rest of the proton bunches are passed to the neutron and muon beamline in the Material and Life Science Facility.

#### Neutrino beam production

The neutrino beam is produced using the primary and secondary beamline as shown in Figure 2.2. The primary beamline takes the proton beam from the MR and directs it towards Kamioka. The beam is then transferred through a succession of beam monitors which measure facets of the proton beam including the beam profile, intensity and position. The beam monitor which is closest to the graphite target measures the "Protons-On-Target" (POT), a value used to determine the neutrino beam flux. The secondary beamline takes the proton bunches and passes them through a target station, the decay volume and the beam dump. After interacting with the target station, the proton bunches are collimated through a 1.7 m graphite rod where the collimated hole the proton bunches pass through are 30 mm in diameter. Beam profile reconstruction occurs in the OTR (Optical Transition Radiation) monitor, made up of titanium alloy foil placed at a 45 degree angle in order to intercept the beam. As the proton beam enters the foil, the visible light that is produced escapes through a collection of mirrors and is then captured by a charge injection device camera, which creates the beam profile.

After beam profiling, the proton beam then impacts upon a graphite rod target which is 91.4 cm long and 2.6 cm in diameter - this collision produces secondary hadrons, including pions which are focused by three magnetic horns (shown in Figures 2.1a, 2.1b and 2.1c). These magnetic horns can be used to produce either a muon neutrino or muon antineutrino beam depending on the polarity of the 250kA current they are pulsed with. If a +250 kA



(a) T2K Horn 1

(b) T2K Horn 2



(c) T2K Horn 3

current is used, the positive pions and kaons produced can go on to make muon neutrino beams whereas if a -250 kA current is used negative pions and kaons can decay to create muon antineutrino beams (both are shown in Equation 2.1). The +250 kA mode is called Forward Horn Current (FHC) mode and the -250 kA mode is called Reversed Horn Current (RHC) mode. The analysis in this thesis will occur in FHC mode only.



A 75 ton volume beam dump made of graphite and iron stops the particles, specifically



Figure 2.2: Schematic of the neutrino beam line

the protons, secondary hadrons and mesons which have a momentum below  $5 \text{ GeV}/c$ , and therefore end up being absorbed by the beam dump. A muon monitor is placed after the beam dump in order to directly measure the the beam intensity and beam direction. Muons can be used to monitor the beam properties because along with the neutrinos these are the main particles produced from pion decay. After the muon monitor, a nucleon emulsion plate detector measures the flux and momentum of the muons.

### 2.1.2 Near detectors

#### INGRID detector

The INGRID (Ineractive Neutrino GRID) detector is a neutrino detector which unlike ND280 is placed on-axis instead of off-axis. This allows it to directly monitor the direction and the intensity of the neutrino beam by measuring the interactions of the neutrinos with the alternating iron plates that make it up. INGRID is also placed 280 m from the graphite target and consists of 14 modules placed in a cross formation, with the centre of the cross placed at the centre of the neutrino beam. The INGRID modules are comprised of nine iron plates alternating with 11 tracking scintillator planes, which are themselves surrounded by scintillator plates the purpose of which is to reject interactions that occur



Figure 2.3: Schematic of the INGRID cross taken from [18].

outside the module. A schematic of the INGRID cross is shown in 2.3 and a schematic of the modules is shown in 2.4.

An additional module, called the proton module, was added to more precisely measure the neutrino interaction cross-section with the T2K on-axis neutrino beam. This module is used to distinguish the quasi-elastic interaction channel in order to compare it with Monte Carlo simulations of the beamline and neutrino interactions. The Proton Module is made of scintillator planes (no alternating iron plates) and is contained by veto planes. The Proton Module was placed in the centre of the INGRID cross at the intersection of the vertical and horizontal modules. Figure 2.5 shows what a standard neutrino event looks like on the INGRID module. A neutrino enters from the left and after interacting with the scintillator cells (shown in green) produces hits (shown in red), with the relative size of each circle corresponding to the observed signal in that cell. The blue cells show the



Figure 2.4: Individual INGRID module schematic taken from [18].

position of the veto scintillators, while the gray planes show the iron plates.

By reconstructing the profile of the beam in x and y directions using the number of neutrino events in seven horizontal and vertical INGRID modules, and fitting the profiles with a Gaussian, the centre of the beam can be defined as the peak of the Gaussian fit. The beam direction can then be reconstructed as the direction from the proton beam target to the reconstructed beam centre. Figure 2.6 shows these neutrino beam centres from the centre of INGRID, for both the x and y directions, measured in April 2010 [20].

## ND280

ND280 is a near detector which sits 280 m from the target. It is an off-axis detector, meaning that just like Super-Kamiokande, it is placed 2.5 ° off-axis from the center of the beam. This stems from the relationship between the energy of the neutrinos produced from the decay of the pions, a relationship shown in Equation 2.2.

$$E_\nu = \frac{m_\pi^2 - m_\mu^2}{2(E_\pi - \sqrt{E_\pi^2 - m_\pi^2} \cos \theta)} \quad (2.2)$$

where  $E_\pi$  is the energy of the parent pion and  $\theta$  is the scattering angle between the direction of the outgoing neutrino and the direction of the parent pion's momentum,  $m_{pi}$  is the parent pion mass and  $m_\mu$  is the mass of the outgoing muon. Figure 2.7 shows the neutrino energy from pion decay plotted against the energy of the parent pion for a range of off-axis angles.



Figure 2.5: INGRID event display showing a typical INGRID event, taken from [19].



Figure 2.6: Neutrino beam profiles for x (left) and y (right) directions.



Figure 2.7: Energy of the neutrino plotted against the energy of the parent pion for multiple different off-axis angles

As off-axis angle increases, the intensity of the neutrino beam decreases, and therefore picking an off-axis angle of  $2.5^\circ$  at which to place the ND280 detector complex strikes a good balance between keeping a high beam intensity while ensuring a peak energy of 0.6 GeV in order to have the neutrino oscillation be maximised at 295km. The relationship between muon neutrino oscillation probability and muon neutrino energy is shown at the top in Figure 2.8, and at the bottom the muon neutrino flux 295 km away from the graphite target can be seen for three different off-axis angles.

Figure 2.9 shows a schematic of the ND280 detector complex. It has five main goals: firstly, to measure the cross sections of muon neutrino interactions, so neutrino-nucleus interaction models can reduce their systematic uncertainties. Secondly, measuring the component of the neutrino beam which is made of electron neutrinos, hence being able to better constrain the background to electron neutrino appearance at the far detector. Thirdly, to predict the event rate at Super-Kamiokande by measuring the energy spectrum of the muon neutrinos produced. It also aims to study non quasi-elastic processes which produce pions below the Super Kamiokande Cherenkov threshold, and to measure the neutral current (NC) pion-nought production rates.

N2D280 is made of a neutral pion detector (*P0D*), three Time Projection Chambers



Figure 2.8: The probability of survival of muon neutrinos (top plot) and neutrino beam flux at the 295km far detector (bottom) Taken from [18].



Figure 2.9: Near detector ND280 schematic taken from [19].

(TPCs) and two Fine Grained Detectors (FGDs). These are enclosed within Electromagnetic Calorimeters (ECals) and a Side Muon Range Detector (SMRD). These detectors are magnetised using a magnet originally used in the UA1 detector at CERN.

The neutral pion detector is important due to its ability to detect a process that can imitate the signal event of electron neutrino appearance at Super-Kamiokande. Neutral pions are produced during the neutral current interactions on water ( $\nu_\mu + N \rightarrow \nu_\mu + N' + \pi^0 + X$ ) and the purpose of *P0D* is to measure the cross-section of this interaction.

There are also two electromagnetic calorimeters which remove events entering the detector from the outside. The SMRD (Side Muon Range Detector) is used as a way to measure the momenta of muons which escape the detector complex at a large angle relative to the direction of the beam.

There are three time projection chambers placed downstream of the neutral pion detector. These are used for reconstruction of charged particle tracks, particle identification and determination of the momentum of the particle. There are two fine grained detectors (FGDs) in ND280, which have two purposes. Firstly to yield a mass for the neutrino interaction, and secondly, to track the charged particles issuing from the neutrino interaction vertex. The ECal is an electromagnetic calorimeter which surrounds the P0D, the TPCs and the FGDs. It consists of plastic scintillator layers sandwiched between lead absorber sheets. Its purpose is to aid in the full event reconstruction through detecting photons and measuring their energy and direction, along with detecting charged particles and getting information which helps in their identification (separating out electrons, muons and pions.)

# Chapter 3

## The Super Kamiokande Detector

### 3.1 The Super-Kamiokande detector

#### 3.1.1 Background and detector design

Super-Kamiokande is a neutrino observatory consisting of a cylindrical tank which is 41.4 m in height and 39.3 m in diameter, and filled with 50kton of ultrapure water and currently with 0.026% gadolinium sulphate. It is used as a neutrino detector for atmospheric, solar and astrophysical neutrinos, as well as being a far detector of the T2K neutrino beam. It is based in the Mozumi mine, located in Gifu Prefecture, Japan. Due to its location being underneath Mount Ikenoyama, 1000m underground, it is shielded from the cosmic ray muon detector background. Super-Kamiokande is divided into two concentric cylinder volumes, consisting of the inner detector (ID) and outer detector (OD) using a stainless steel structure which supports the photomultiplier tubes. Tyvek and black polyethylene terephthalate sheets are mounted on this structure in order to optically separate the inner and outer detector [21].

The inner detector is a cylinder which has a diameter of 33.8 m and a height of 36.2m, and has a fiducial volume of 22.5 ktons of water. The fiducial volume is defined as the region inside a surface drawn 2.00 m from the inner detector wall. Using this fiducial volume gives protection against events produced from natural radioactivity in the surrounding rock. The detector contains 11,129 photomultiplier tubes which give 40% photocoverage of its inner surface, with the specific photomultiplier model chosen being the hemispherical, 50.8 cm diameter Hamamatsu R3600 model. The 2 m wide outer detector has only 1885

photomultiplier tubes which are mounted on the outside of stainless steel structure, each with a smaller diameter of 20cm, and are either the R1408 or R5912 Hamamatsu model. Each outer detector photomultiplier tube is attached to a 50cm x 50cm wavelength shifting plate, improving the light collection ability in the OD [22].

A detailed schematic of the photomultiplier tubes used in Super-Kamiokande can be seen in Figure 3.1. The photocathodes used in these PMTs are comprised of bialkali antimony-potassium-caesium material (Sb-K-Cs), which give a greater sensitivity to longer wavelengths, giving the greatest spectral response at 360 nm, near the ultraviolet range. This makes these types of photocathodes suitable to use for matching with light sources in the blue region of the visible spectrum, which is the region in which the wavelength of Cherenkov photons lie. The 11 dynodes which are inside the photomultiplier tube are arranged in a “venetian blind” fashion, meaning that the dynodes consist of an assembly of parallel strips. This results in a good collection efficiency of the multiplied electrons and gives decent protection from external magnetic fields. More protection from external magnetic fields is provided by a set of Helmholtz coils which are aligned outside the inner detector, which reduce the ambient background geomagnetic field from 450mG to 50mG. This is needed due to the systematic bias that could occur due to the strength and uniform direction of this magnetic field affecting the photo-electron trajectories and consequently the photomultiplier tube hit timing.

Radioactivity from radon, uranium and thorium radioisotopes in the Super-Kamiokande tank water and radon in the surrounding air could provide a low energy background to measurements which should be negated. In low-energy analyses, such as the analysis in this thesis, this becomes an even more significant issue. Microbes present in the mine water also present a problem as they cause a reduction in the the light attenuation length. Therefore the water used in Super-Kamiokande has to undergo a purification process - the water used is continuously reprocessed at a rate of 30 tons  $h^{-1}$  in a closed loop system, which is the same method used to purify the water when refilling the tank. The first step of this water purification process is to use a 1  $\mu m$  mesh filter to remove large particulates of impurities from the water [23]. A heat exchanger is then used to cool down the water to a constant 13.0 °C to reduce the dark noise hits of the photomultiplier tubes and the growth of the microbes. A treatment with ultraviolet light is then used to kill any remaining microbes in the water. Radon-free air is then dissolved into the water to aid in the later process of radon removal from the water and a high performance membrane ultra filter (UF) is used to remove organic compounds about 10 nm in diamater from the



Figure 3.1: Schematic of an ID 50 cm Super-Kamiokande PMT [22].

water. After this step a membrane degasifier removes the dissolved radon, where 30 L of radon reduced air is supplied to the membrane degasifier. The dissolved radon will transfer across the membrane but the water will not, allowing for efficient radon reduction.

The inner detector tank water is circulated by injecting the water at the bottom of the tank and extracting it from the top, where the convection currents are able to maintain the temperature in the region within 11 m to the bottom of tank, however, outside this region the present temperature gradient causes an asymmetry in the attenuation of light, which is discussed more in Chapter 3.

An air purification system is also installed in Super-Kamiokande in order to reduce the amount of Radon present which could dissolve into the tank and affect measurements. The level of radon activity achieved after this air purification has taken place is  $1 \text{ mBq}/\text{m}^3$ .

The Super-Kamiokande experiment began taking data on 1st April 1996, and due to maintenance was shut down in July 2001, which was phase I of the experiment. A table of the Super-Kamiokande phases is shown in Table 3.1. During the refilling of the tank after maintenance, there was cascade of PMT implosions that occurred on the 12th of November 2001, which were triggered by the implosion of a single photomultiplier tube,

due to a microfracture in the neck of the tube. This implosion destroyed about 7,000 of the PMTs and in order to avoid such chain reactions in the future, from 2002 onwards all of the inner detector PMTs are fitted with acrylic covers and fiber-glass reinforced plastic (FRP) cases. Detector shutdown and rebuild took nine months and Super-Kamiokande resumed data taking with the full number of photomultiplier tubes in July 2006 which marked the beginning of Super-Kamiokande phase III. Super-Kamiokande phase IV began in September 2008 where a new data acquisition system and charge to time (QTC) based electronics with Ethernet (QBEE) was deployed in order to measure arrival times and integrated charge for inner detector and outer detector photomultiplier tube signals. This replaced the ATM (Analogue and Timing Module). The improvements in electronics and calibration methods meant that when Super-Kamiokande phase IV started running in September of 2008, electrons with energies as low as 3.5 MeV were able to be detected.

Phase	Phase Period	Total PMT number		FRP case?	Readout	Gd%
		ID (Coverage)	OD			
SK-I	Apr. 1996 - Jul. 2001	11146(40%)	1884	no	ATM	0
SK-II	Oct. 2002 - Oct. 2005	5182(19%)	1884	yes	ATM	0
SK-III	Jul. 2006 - Sep. 2008	11129(40%)	1884	yes	ATM	0
SK-IV	Sep. 2008 - May 2018	11129(40%)	1884	yes	QBEE	0
SK-V	Jan. 2019 - Jul. 2020	11129(40%)	1884	yes	QBEE	0
SK-VI	Aug. 2020 - May 2022	11129(40%)	1884	yes	QBEE	0.01%
SK-VII	Jun. 2022 - Today	11129(40%)	1884	yes	QBEE	0.03%

Table 3.1: Phases of Super-Kamiokande and main properties of each phase

### 3.1.2 Data aquisition system

As shown in Table 3.1, Phase IV of the experiment marked the beginning of Super-Kamiokande using QTC-based Electronics with Ethernet (QBEEs). Each QBEE board used in Super-Kamiokande contains 24 photomultiplier tube input channel, where each channel uses a charge-to-time (QTC) converter and a time-to-digital converter placed in



Figure 3.2: Schematic of the charge-to-time converter circuit [24].

series as shown in Figure 3.2. After a single photoelectron is produced by the photomultiplier tubes after incident photons have been received upon it, the dynodes inside the photomultiplier tube amplify this photoelectron so that each photoelectron that strikes the surface of the dynode produces several more photoelectrons, which are produced from the dynodes as an analogue signal. This signal then enters a charge-to-time converter (QTC), an application specific integrated circuit (ASIC) which was specifically designed for Super-Kamiokande in order to detect photomultiplier tube signals using built-in discriminators and to produce output timing signals whose widths represent the integrated charge of the PMT signal. The QTC used has three input channels per chip, which has three gain ranges (Small, Medium, Large as shown in Figure 3.2). There is a built in discriminator inside the QTC which determines whether the signal from a PMT is a “hit”. If the PMT signal exceeds the threshold value of this discriminator, the QTC integrates the charge of the signal over the next 400 ns, and a square wave pulse is generated whose pulse width is proportional to the integrated charge of the input signal from the PMT. The next 400 ns is used to discharge the integrated charge from the QTC, leading to a total channel dead time of 900 ns due to summing the charge integration and discharge of the QTC.

A time-to-digital converter (TDC) then digitises the output time signal, so the PMT charge information is retained. These digitised outputs are collated by 20 front-end com-

puters which collects all the information from the inner and outer detectors, with each computer taking the PMT hit information from 30 inner detector and 20 outer detector QBEE boards and sorting the PMT hit time information in order of the raw hit time. This information is then sent to “merger” computers, who then produce a full time-ordered list of all PMT hits. These merger computers then apply software triggers to select event candidates, using  $N_{200}$ , a quantity which determines the number of PMT hits in a 200 ns timing window. When the value of  $N_{200}$  surpasses the threshold value of a certain trigger type (whether it is a SLE (Super Low Energy), LE (Low Energy), HE (High Energy), SHE (Super High Energy), OD (Outer Detector) or AFT (After Window) trigger), the trigger is used to select an event candidate. The SLE, LE, HE and SHE triggers roughly define the energy of a certain event, based on the number of hits detected. The OD trigger is used to veto events, and the AFT trigger is of special importance to the analysis in this thesis: it is used to discern when a neutron is produced after a neutrino interaction. The AFT Trigger is issued to take 500  $\mu$ sec of data after SHE trigger in order to identify the positron from the prompt event and the delayed 2.2 MeV gamma released from the neutron capture on the proton during the IBD reaction. Another set of computers acts as an “organiser”: it takes all the information regarding the event candidates from the “merger” computers and writes them onto disks [22].

## 3.2 Event Reconstruction

### 3.2.1 Vertex Reconstruction

For low energy events (events up to 100 MeV), Super-Kamiokande currently uses BONSAI (Branch Optimisation Navigating Successive Annealing Interactions) for event reconstruction. Vertex reconstruction for Super-Kamiokande has undergone changes and improvements depending on the phase of the experiment.

For Phase I of Super-Kamiokande, vertex reconstruction depended on a lattice of test vertices with 4 m spacing throughout the detector, with a specific measure of goodness for each test vertex: the test vertex with the highest measure of goodness would have around it a more finely spaced grid, and the process would be repeated. For Phase II of Super-Kamiokande due to the reduced number of PMTs, this approach was no longer as successful as it was in Phase I and as a result the reconstruction performance declined, and BONSAI was created as a replacement. Instead of using a fixed grid which was the case

with SK-I and SK-II, BONSAI creates test vertices by selecting groups of four PMT hits and seeing where the timing residuals of the PMT hits would be most reduced. After these test vertices have been identified, a maximum likelihood fit over all the PMT hits in the event is performed, shown in Equation 3.1.

$$\mathcal{L}(\vec{x}, t_0) = \sum_{i=1}^{N_{\text{hlt}}} \log(P(t - t_{\text{tof}} - t_0)) \quad (3.1)$$

where  $(\vec{x}, t_0)$  is the test vertex, and  $(P(t - t_{\text{tof}} - t_0))$  (shown in Figure 3.3) is the probability density function of the timing residual, which for each PMT hit is defined as  $(t - t_{\text{tof}} - t_0)$ , where  $t_0$  is the time of the interaction,  $t_{\text{tof}}$  is the time of flight from the interaction vertex position to the position of the hit PMT,  $t$  is the PMT hit time. The  $1\sigma$  difference between the true vertex position and the reconstructed vertex position plotted as a function of true electron energy is shown in Figure 3.4.

### 3.2.2 Direction Reconstruction

Cherenkov light is emitted in a conical formation as electrons and positrons travel through water, with a Cherenkov angle of  $\approx 42^\circ$ . BONSAI can reconstruct the direction of these particles by using this information along with the reconstructed vertex. This reconstruction occurs using a maximum likelihood function defined in Equation 3.2.

$$\mathcal{L}(\vec{d}) = \sum_i^{N_{20}} \log(f(\cos \theta_i, E)) \times \frac{\cos \theta_i}{a(\theta_i)} \quad (3.2)$$

The term  $f(\cos \theta_i, E)$  in Equation 3.2 is the expected distribution of the angle between the vector of the direction  $\vec{d}$  of the particle, and the observed Cherenkov photon from the position of the reconstructed vertex. The reason there is a spread in this energy distribution is because while the highest value of this distribution occurs at the cosine of the opening Cherenkov angle of  $42^\circ$ , due to the particle travelling through the water being Coulomb scattered multiple times, there is a variation in the angle because of the varying particle energy. The term  $N_{20}$  is the number of hits whose residual hit time is within 20 ns of the time of the reconstructed event, which is used in order to reduce the amount dark noise and scattered photons contribute to the direction reconstruction calculation. The variable  $a(\theta_i)$  is a correction factor stemming from the acceptance of PMTs and therefore linked to the shape of the PMT and its acrylic case, is linked to the angle of incidence of the photon



Figure 3.3: Probability density of the timing residual  $P(t - t_{\text{tof}} - t_0)$ , where  $t_0$  is used for the vertex reconstruction maximum likelihood fit. The peaks at 30ns and 100ns are caused by PMT after-pulsing.



Figure 3.4: The vertex resolution (the point at which 68% of the events in the distance distribution between the actual and reconstructed vertex are contained) for the different SK phases. SK-I (Blue), SK-III (Red), SK-IV (Black).

on the PMT, and is related to the angle of incidence of the photon on the PMT.

### 3.2.3 Energy reconstruction

The kinetic energy of a particle is proportional to the amount of Cherenkov photons emitted from it, and if we assume that the Cherenkov photons in a single event come from a single electron, we can reconstruct the total energy of the electron. Instead of using the number of photoelectrons of all hit photomultiplier tubes to reconstruct the energy of low energy events, the number of hit photomultiplier tubes is used instead. The reasons for this are threefold - firstly, low energy events emit a small number of Cherenkov photons, and therefore average about one photon per hit PMT. Secondly, at single photoelectron level, the resolution of the PMTs is poor, and third, the number of photoelectrons produced is related to the gain of the PMT.

Due to the variation in gain value not affecting the number of hit photomultiplier tubes as much as it does for the number of photoelectrons, number of hit PMTs is used instead. To reduce dark noise, energy reconstruction uses  $N_{50}$ , which is the number of time of flight corrected photomultiplier tube hits in a 50 ns window. The number of effective photomultiplier tubes which are hit in this timing window of 50 ns are summed up, while being weighted with correction factors, to give  $N_{eff}$  shown in Equation 3.3 [25].

$$N_{eff} = \sum_{i=1}^{N_{50}} \left[ (X_i - \epsilon_{dark} + \epsilon_{tail}) \times \frac{N_{all}}{N_{alive}} \times \frac{1}{S(\theta_i, \phi_i)} \times \exp\left(\frac{r_i}{\lambda}\right) \times G(i) \right] \quad (3.3)$$

where  $X_i$  is the correction factor hits with many photoelectrons. This correction factor is important because if some photomultiplier tubes are hit by multiple photons (for example, if the edge of the fiducial volume is where the event vertex took place). The number of photoelectrons produced by each hit photomultiplier tube is estimated using the occupancy of the eight photomultiplier tubes which surround it. Using the number of hit photomultiplier tubes ( $n_i$ ) and the number of functional photomultiplier tubes that surround the i-th photomultiplier tube ( $N_i$ ), the formula for  $X_i$  is shown in Equation 3.4.

$$X_i = \begin{cases} \log(1 - n_i/N_i)^{-N_i/n_i} & (n_i < N_i) \\ 3 & (n_i = N_i) \end{cases} \quad (3.4)$$

The term  $\epsilon_{dark}$  in Equation 3.4 is a correction factor for dark noise hits, shown in

Equation 3.5, where  $R_{dark}$  is the average value for the dark rate during the run period that the event is in and  $N_{PMT\text{alive}}$  is the number of active photomultiplier tubes in the inner detector.

$$\epsilon_{dark} = \frac{N_{PMT\text{alive}} \times R_{dark} \times 50 \text{ ns}}{N_{50}} \quad (3.5)$$

The term  $\epsilon_{tail}$  is the correction factor for photomultiplier tube hits which are in the tail end of the 50ns timing window, and is defined in Equation 3.6.

$$\epsilon_{tail} = \frac{N_{100} - N_{50} - N_{alive} \times R_{dark} \times (100 - 50)\text{ns}}{N_{50}} \quad (3.6)$$

The term  $\frac{1}{S(\theta_i, \phi_i)}$  is the inverse of the effective area of the ith hit photomultiplier tube photocathode, from the direction of the incident photon given by it's solid angle  $(\theta_i, \phi_i)$ .

$G(i)$  is the gain correction for the quantum efficiency of the photomultiplier tubes and  $exp(\frac{r_s}{\lambda})$  is the correction for water transparency which accounts for the amount of attenuation undergone by the photons in water, where  $\lambda$  is the water transparency measured during the run period which includes the event, and  $r_i$  is the distance between the reconstructed event vertex and the i-th hit PMT.

The average of each  $N_{eff}$  distribution is taken, after producing multiple  $N_{eff}$  distributions with fixed energies using Monte Carlo. These energies are fitted with a polynomial which is a function of the averaged  $N_{eff}$  distribution, so the reconstructed energy is converted from  $N_{eff}$ .

### 3.3 Super-Kamiokande Gadolinium Upgrade

In order to be able to observe the diffuse supernova neutrino background (DSNB) flux it was proposed that Gadolinium (Gd) should be added to the the water in Super-Kamiokande. There are two natural isotopes of gadolinium, Gd-155 and Gd-157, which have large thermal neutron capture cross sections of 60740 barns and 253700 barns respectively: when neutrons are captured on them there is a cascade of gamma rays that occurs, with an energy totalling 8 MeV. However when a neutron is captured on hydrogen, a single 2.2 MeV gamma ray is produced. [26]. The ultimate aim is to load a total amount of gadolinium in the form of gadolinium sulphate octahydrate ( $\text{Gd}_2(\text{SO}_4)_3 \cdot 8\text{H}_2\text{O}$ ) in Super-Kamiokande which equates to 0.2% of Gd by mass, resulting in 90% neutron capture efficiency. The ability to tag

neutrons efficiently in Super-Kamiokande will benefit multiple physics topics, not only for the aforementioned observation of DSNB flux, but also for analyses involving atmospheric neutrinos and proton decay.

### 3.3.1 Americium/Beryllium Calibration

The use of an Americium/Beryllium (Am/Be) calibration source deployed in Super-Kamiokande and also in the EGADS project (see next section) is very useful for validating the neutron tagging algorithm and for measuring the neutron capture time constant from neutrons captured on gadolinium. An Am/Be source is placed inside a 5 x 5 x 5 BGO (Bismuth Germanate Oxide) crystal cube. A 4.4 MeV gamma ray is produced from the Am/Be source decay (shown in Equation 3.7) and this is detected by the detector from the large number of scintillation photons generated by this gamma ray passing through the BGO crystal. This 4.4 MeV gamma ray serves as the prompt event, and the delayed neutrons produced can be searched for after the 4.4 MeV gamma ray signal.



The Am/Be source was used both in both EGADS (see next section) and Super-Kamiokande in order to measure the gadolinium concentration and the neutron capture time constant, and due to its similarity to the neutral current quasielastic events studied in the analysis in this thesis, it can serve as a helpful control sample and is used in the calculation of the detector response uncertainty in Chapter 7.

### 3.3.2 The EGADS project

In 2009, prior to the addition of gadolinium in Super-Kamiokande, the EGADS (Evaluating Gadolinium's Action on Detector Systems) project was used to evaluate how the inclusion of  $\text{Gd}_2(\text{SO}_4)_3 \cdot 8\text{H}_2\text{O}$  would affect water quality and detector components inside Super-Kamiokande and their analyses, and also to test the water system circulation. Measurements regarding neutron tagging were also taken using an Americium/Beryllium (Am/Be) source placed inside EGADS. The delayed neutron capture time from an Am/Be source used in EGADS with the gadolinium sulphate concentration of 0.2% is shown in Figure 3.5. Here, we can see that the neutron capture time from the data is  $29 \pm 0.3 \mu\text{s}$  and for the Monte Carlo it is  $30 \pm 0.8 \mu\text{s}$ .



Figure 3.5: (a) Delayed neutron capture time from prompt event with Am/Be source. (b) Reconstructed energy from gamma rays after neutron capture. Taken from [17]

EGADS represented the most realistic possible soak test, and after two and a half years of running, EGADS was emptied in November 2017 to check the condition of the inner structure and the photomultiplier tubes. There was no deterioration of any of the components, which was an excellent sign for a detector designed to so closely resemble the conditions for the Super-Kamiokande Gadolinium upgrade.

### 3.3.3 Gadolinium loading into Super-Kamiokande

After the success of EGADS, the Super-Kamiokande Gadolinium project was formed in 2015 with the final goal of adding 0.2%  $\text{Gd}_2(\text{SO}_4)_3 \cdot 8\text{H}_2\text{O}$  by mass to the detector. The first step of gadolinium loading began with the loading of 13 tons of  $\text{Gd}_2(\text{SO}_4)_3 \cdot 8\text{H}_2\text{O}$  into Super-Kamiokande from July 14th to August 17th 2020, which is about 10% of the target concentration. The work in this thesis focuses on this first Gd loading period with a Gd concentration of 0.01%, not the second loading period which began in late May of 2022, with the target concentration of 0.03%.

#### The SK-Gd water system

The SK-Gd water system was designed to dissolve  $\text{Gd}_2(\text{SO}_4)_3 \cdot 8\text{H}_2\text{O}$  powder into the detector water, pass it through a “pretreatment” system to remove contaminants from the water, and then to continuously circulate it. The design for this treatment system was successfully tested in EGADS and involves treating this solution with ultraviolet light.

Chain	Isotope	Criterion [mBq/kg]	Physics target
$^{238}\text{U}$	$^{238}\text{U}$	< 5	SRN
	$^{226}\text{Ra}$	< 0.5	Solar
$^{232}\text{Th}$	$^{232}\text{Th}$	< 0.05	Solar
	$^{228}\text{Ra}$	< 0.05	Solar
$^{235}\text{U}$	$^{235}\text{U}$	< 30	Solar
	$^{227}\text{Ac}/^{227}\text{Th}$	< 30	Solar

Table 3.2: Table of impurities in the gadolinium sulphate octahydrate powder

Positively charged impurities dissolved in the solution (such as radium ions) and negatively charged impurities (such as uranium) are removed using a cation and anion exchange resins respectively, after which a UV steriliser removes bacteria which were introduced in the dissolving process.

The acceptable background rate after the final value for Gd loading was set to be less than double that of the background rate for when Super-Kamiokande ran with pure water. As a result, rigorous standards of cleanliness were set for the  $\text{Gd}_2(\text{SO}_4)_3 \cdot 8\text{H}_2\text{O}$  powder, which meant setting maximum allowed levels of radioactive impurities which are shown in Table 3.2.

### SK-Gd attenuation, transparency and concentration monitoring

After the loading of gadolinium into Super-Kamiokande, water transparency and attenuation length were continuously monitored. This had also been conducted in EGADS (see previous section), but due to the flow rate of the water and method by which gadolinium is loaded into the detector being different in Super-Kamiokande, it is important to monitor these attributes in the SK-Gd upgrade as well. Figure 3.6 shows how the attenuation length of the Cherenkov light in SK-Gd varies with time: this attenuation length is measured using cosmic ray through going muons (as explained in Chapter 3). There is a clear decrease in the attenuation length after the loading of  $\text{Gd}_2(\text{SO}_4)_3 \cdot 8\text{H}_2\text{O}$ , reaching a minimum of 75 m in August of 2020, and increasing again to its original pre-Gadolinium loading value of 90 m by the beginning of December 2020.

It is important to monitor the concentration of the  $\text{Gd}_2(\text{SO}_4)_3 \cdot 8\text{H}_2\text{O}$  in the detector - this can be done using either direct sampling via calibration ports or using



Figure 3.6: The attenuation length of Cherenkov light measured using cosmic ray muons between March of 2020 and March of 2021, taken from [17]. The dashed lines on the figure indicate the first Gadolinium loading period from July 14th 2020 to August 17th 2020.



**Fig. 8.** Conductivity vs. Z position in the ID during Gd loading.  $Z=+19$  m is inside the calibration guide pipe.

Figure 3.7: Conductivity vs. z position during Gd loading inside the inner detector, taken from [27].

the Am/Be neutron source. By measuring the conductivity of the ions, the concentration of  $\text{Gd}_2(\text{SO}_4)_3 \cdot 8\text{H}_2\text{O}$  can be determined. Figure 3.7 shows the variation of the  $\text{Gd}_2(\text{SO}_4)_3 \cdot 8\text{H}_2\text{O}$  concentration in the detector at different depths in the detector during various points in time during the gadolinium loading period.

Deployment of this Am/Be source into the inner detector of Super-Kamiokande using the central calibration port and then monitoring the source at three positions along the Z-axis, the concentration of  $\text{Gd}_2(\text{SO}_4)_3 \cdot 8\text{H}_2\text{O}$  could be measured. One measurement position is in the middle of the detector ( $Z=0$  m) and the other two were at  $Z = +12$  and  $Z = -12$  m respectively. By searching for neutron capture events on gadolinium from the Am/Be data, a time distribution of neutron capture candidates could be plotted and fit with a function shown in Figure 3.8. The Am/Be source position here was  $Z=0$  m and the  $0 \mu\text{s}$  time value on the x-axis is the time at which the scintillation photons produced by the 4.4 MeV gamma ray from its passing through the BGO cube are detected.

Using GEANT4 Monte Carlo simulations, the neutron capture time can be converted to a value for Gd concentration, where the measured mean capture lifetime of  $115 \pm 1$



Figure 3.8: Neutron capture time distribution for the Am/Be source placed at Z=0 m, taken from [27].

$\mu$ s corresponds to a Gd concentration value of  $111 \pm 2$  ppm, consistent with the target concentration value of 0.011%.

To summarise, Super-Kamiokande has undergone a lot of transformations over its lifetime, with modifications made to its data acquisition system and methods of event reconstruction with each successive new phase. The biggest change made to the detector is the upgrade to Super-Kamiokande Gd, where in the summer of 2020 0.026% of  $\text{Gd}_2(\text{SO}_4)_3 \cdot 8\text{H}_2\text{O}$  was added to the detector: a long-awaited next step to enhance sensitivity to the detection of neutrons emitted in inverse beta decay compared to that in water.

## Chapter 4

# Super-Kamiokande Detector Calibration

In order to achieve optimal event reconstruction for physics analyses, calibration of the Super-Kamiokande detector is crucial. For example, when conducting Monte Carlo simulations of certain processes in the detector, facets of the experiment such as properties of the water, photomultiplier tube response and the inner detector and outer detector electronics are all calibrated so that input parameters for the Monte Carlo simulations can be obtained. This chapter will concern itself with the inner and outer detector calibration, including photomultiplier tube and electronics calibration, PMT gain calibration, quantum efficiency determination and hit timing and charge information calibration.

### 4.1 Inner detector calibration

#### 4.1.1 PMT High-voltage setting calibration

The high-voltage (HV) setting for all photomultiplier tubes need to be adjusted individually so all the PMTs produce the same amount of charge for a certain light intensity received by them. Placing a light source which distributes light isotropically in the centre of the inner detector to achieve this calibration means that there is no position in the detector from which the inner detector PMTs are equidistant, so each PMT will not receive the same amount of light from the light source. To avoid this problem, a set of 420 pre-calibrated PMTs inside the detector were used, separated into groups relating to their geometrical



Figure 4.1: Location of 420 reference PMTs used for HV setting calibration. The red lines in show the placement of these PMTs with respect to the others (left). The grouping of these PMTs due to their geometry in relation to the light source is also shown (right)

distance from the HV calibration light source, which is shown in Figure 4.1 for their location with respect to the other photomultiplier tubes.

#### 4.1.2 Relative gain calibration

Understanding the timing information from the hit photomultiplier tubes depends on how well the charge from the hit PMT is calculated. To conceive charge calibration, a quantity called photomultiplier tube “gain” must be calculated. “Gain” is the conversion factor from the number of photoelectrons produced by the hit PMT and charge, specifically how much charge one can expect from a single phtotoelectron from the PMT anode. Along with the PMT gain, there are three other quantities which relate to charge calibration: quantum efficiency, collection efficiency and light collection efficiency.

The quantum efficiency (QE) is the ratio of the number of photoelectrons produced by the photocathode, to the number of incident photons on the photocathode. The collection efficiency is the fraction of the total number pf photoelectrons produced which are collected by the first dynode in the PMT. The product of the quantum efficiency and the collection

efficiency, gives the light collection efficiency.

Knowing the gain and light collection efficiency of each PMT in the detector is important in order to accurately measure the output charge from each individual PMT, which is done by first calculating the relative gain difference among all PMTs and then working out the average gain difference over all PMTs in the detector. After this, the variation away from this average gain value can be calculated for each separate inner detector photomultiplier tube, and the gain value for each can be extracted.

The relative gain difference is calculated by two measurements using a light source to produce constant-intensity flashes. The first measurement involves using the light source to produce high-intensity flashes so that all photomultiplier tubes in the detector get a certain number of photons, and the second measurement has the light source produce low-intensity flashes so that only a few PMTs are hit. The first measurement provides an average charge value ( $Q_{obs}(i)$ ) for each inner detector PMT, while the second measurement gives single photoelectron hits, providing a number of times ( $N_{obs}(i)$ ) that a single PMT gives a charge which is greater than the PMT threshold value. Equations 4.1 and 4.2 shows how these two values are calculated from the high and low intensity flash values ( $I$ ), the acceptance of the PMT(i) ( $a(i)$ ), the QE value of the PMT ( $\varepsilon_{qe}$ ) and the PMT gain  $G$ .

$$Q_{obs}(i) \propto I_{high} \times a(i) \times \varepsilon_{qe}(i) \times G(i) \quad (4.1)$$

$$N_{obs}(i) \propto I_{low} \times a(i) \times \varepsilon_{qe}(i) \quad (4.2)$$

Therefore, by simply dividing these two values of  $Q_{obs}(i)$  and ( $N_{obs}(i)$ ) the average gain over all PMTs can be calculated. Figure 4.2 shows the spread of the relative gain over all the PMTs.

#### 4.1.3 Absolute gain calibration

In order to calculate absolute gain, the single photoelectron distribution needs to be measured, this is because absolute gain relates to the observed charge in the photomultiplier tube with the number of photoelectrons produced. A nickel-californium source (shown in Figure 4.3) is used for this measurement due to it releasing gamma rays isotropically, with a total gamma ray cascade energy of 9 MeV. Thermal neutron capture on nickel is used as the gamma ray source, with the neutrons provided by the spontaneous fission of



Figure 4.2: Relative gain of PMTs in Super-Kamiokande



Figure 4.3: Nickel-californium source used for absolute gain calibration [28]

$^{252}\text{Cf}$ . This nickel source is placed in the centre of the inner detector and the gamma rays produced are detected by all the inner detector PMTs. On average the observed number of photoelectrons is 0.004 per event per PMT, meaning that single p.e. hits are observed for more than 99% of the hits. The observed charge distribution of all the hits from this nickel source is used to give the average charge, which is used as a conversion factor from a charge measurement in picoColoumbs and single photo-electrons. The factor is 2.658 pC per photoelectron (calculated at the beginning of SK-IV) which is then used to extract the single-p.e. distribution, shown in Figure 4.4.

#### 4.1.4 Relative quantum efficiency measurement

To measure the relative quantum efficiency, the gamma rays from neutron capture on the nickel source are simulated. Inside this simulation, a common value of QE is used for all the ID PMTs to predict the number of hits for each PMT. Comparing this number of hits to the actual data obtained for each individual PMT by calculating the ratio between them provides us with a value for relative QE for each inner detector PMT which is then used



Figure 4.4: Single p.e distribution of charge in pC [28]

inside the simulation.

#### 4.1.5 Timing information calibration

Calibrating the hit timing information of the photomultiplier tubes is essential due to its importance in accurately being able to reconstruct events. Event reconstruction makes use of determining exactly where interaction vertices are and the direction in which particles travel, and to do this the time response needs to be very carefully calibrated. The response time of the PMT also relates to the amount of charge observed: in order for a hit to be registered, the PMT signal must pass the discriminator value of the hit threshold, and the time in which this happens is dependent on the height of the pulse, which is correlated with the observed charge. All these factors need to be considered when calibrating hit timing information.

To aid the timing calibration, a diffuser ball is placed near the centre of the inner detector, into which a nitrogen laser injects pulsed laser light. By varying the intensity of this light, the laser light can be outputted in flashes, and the timing of the laser pulses is monitored using a 2-inch monitor PMT. The schematic of this timing calibration system is shown in Figure 4.5.

The value of these laser pulse timings, and the time-of-flight value from the diffuser ball are subtracted from the PMT hit time. Using the observed charge values and these adjusted hit times, “TQ” (time and charge) distributions can be plotted for each inner detector PMT. An example TQ distribution is shown for an inner detector PMT (cable number 00010) in Figure 4.6, where the vertical axis shows the corrected TOF and laser pulse time corrected PMT hit time, and the horizontal axis shows the observed charge of each hit. Figure taken from [28].

The timing resolution of the PMTs (also known as the transit time spread) is also something that must be calibrated. This is calculated by using the same timing and charge data used to produce the TQ distributions. By correcting all the ID PMT hits by their TQ distributions, these residual timing distributions have an asymmetric Gaussian function fitted to them, from which two values of sigma are extracted:  $\sigma_t$  and  $\sigma_{t'}$ . These are the values for the timing resolution for before and after the peak time of this distribution. Equation 4.4 shows how the asymmetric Gaussian is defined.

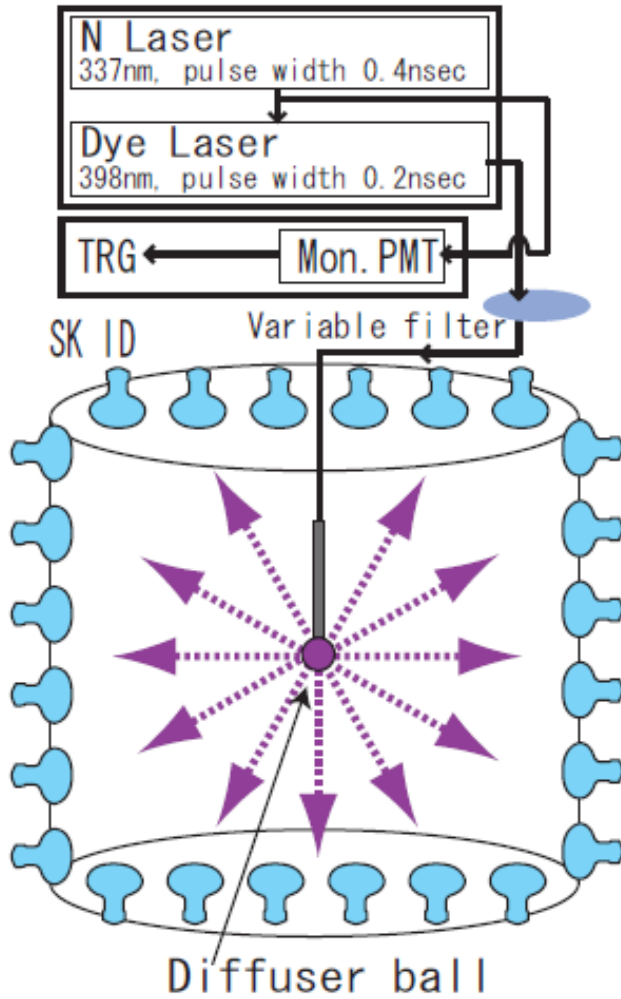


Figure 4.5: Schematic of the timing calibration system, with SK ID PMTs in blue and the diffuser ball in purple. The dye laser shifts the wavelength of the laser light to 398 nm to maximise the quantum efficiency of the PMTs and light absorption.



Figure 4.6: Example TQ distribution for an inner detector PMT

$$f(t; t > T_{\text{peak}}) \equiv A_1 \cdot \exp\left(-(t - T_{\text{peak}})^2 / \sigma_t^2\right) + B_1 \quad (4.3)$$

$$f(t; t \leq T_{\text{peak}}) \equiv A_2 \cdot \exp\left(-(t - T_{\text{peak}})^2 / \sigma_t'^2\right) + B_2 \quad (4.4)$$

Figure 4.7 shows an example of the residual timing distribution fitted with an asymmetric gaussian for a certain value of binned charge.

Figure 4.8 shows timing resolution plotted as a function of charge for both before and after the peak time of the residual time distribution (red and blue points respectively) for SK-IV TQ calibration data.

#### 4.1.6 Measurement of light reflection on the black sheet and the PMTs

For SK-IV, four types of material, corresponding to four different refractive indices are taken into account: water, glass, bialkali, and vacuum. Table 4.1 shows the values for each of these materials,  $\lambda$  is the wavelength of the light in nm and  $n_{\text{real}}$  and  $n_{\text{img}}$  are the real and imaginary parts of the complex refractive index.

Regarding the black sheet used to line the inside of Super-Kamiokande, it can either reflect or absorb Cherenkov photons. The amount of Cherenkov photons detected is measured by a light injector setup, shown in Figure 4.9. For three different incident angles of



Figure 4.7: Residual timing distribution summed over all the readout channels in charge bin 14 (QBin in 4.6.)



Figure 4.8: Timing resolution as a function of charge for SK-IV

Material	Refractive index
Water	1.33
Glass	$1.472 + 3670/\lambda^2$
Bi – alkali	$n_{real} + i n_{img}$
Vacuum	1.00
$x_{abs}^N$	Nucleon absorption probability
$x_\pi^N$	Nucleon $\pi$ -production probability

Table 4.1: Refractive indices of materials inside the Super-K detector.

laser light ( $30^\circ$ ,  $45^\circ$  and  $60^\circ$ ) and three different laser light wavelengths (337 nm, 400 nm and 420 nm) the charge from the light scattered off the black sheet was measured. The direct charge (i.e. the same setup without the black sheet present) was also measured, with the total black sheet reflectivity being the ratio between the scattered charge and the direct charge.

### Measurement of absorption and scattering coefficients

In Super-Kamiokande, the detector medium scatters and absorbs the Cherenkov light, attenuating its wavelength. The amount of light attenuation after the light has travelled distance  $l$  is given by  $\exp(-l/L(\lambda))$ . Here  $L(\lambda)$  is the attenuation length of the detector medium and is shown by Equation 4.5,

$$L(\lambda) = \frac{1}{\alpha_{sym}(\lambda) + \alpha_{asym}(\lambda) + \alpha_{abs}(\lambda)} \quad (4.5)$$

In Equation 4.5, the  $\alpha_{sym}$  parameter consists of two types of scattering: the symmetric component of Mie scattering and Rayleigh scattering, whereas  $\alpha_{asym}$  only consists of asymmetric Mie scattering. Figure 4.10 shows the difference between these two types of scattering:

Rayleigh scattering occurs when light is scattered from very small particles, the size of these particles being less than 1/10 of the wavelength of the light. For particles larger than the wavelength of the light being scattered, Mie scattering becomes more dominant, with more asymmetric scattering occurring the larger the particle is (i.e. with a greater forward lobe for larger particles.) As a result of this  $\alpha_{sym}$  has an angular dependence of  $1 + \cos(\theta)^2$



Figure 4.9: Schematic of the laser light reflectivity. Bird's-eye view (left) and setup inside of Super-Kamiokande (right).

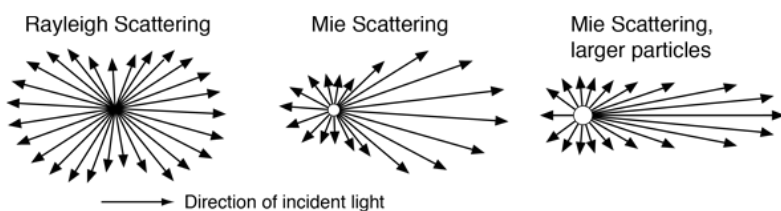


Figure 4.10: Schematic of the differences between Rayleigh and Mie scattering

where  $\theta$  is the angle between the incoming and outgoing scattered photon vectors, but  $\alpha_{\text{asym}}$  has a  $\cos\theta$  dependence, only for forward scattering, and an amplitude of zero for backward scattering. The  $\alpha_{\text{abs}}(\lambda)$  is the amplitude of the light absorption. The method by which these measurements were made is by using a laser system (shown in Figure 4.11), where laser light is injected at several points in the tank, denoted in Figure 4.11 by the barrel injectors (B1-B5), the previously used old top injector (OT), the new top injector (NT), and an injector on the tank bottom (BT).

The absorption and scattering coefficients are measured using data from light injected from the new top (NT) injector. A large set of calibration Monte Carlo are generated using laser generation software and the Super-Kamiokande detector simulation (SKDETSIM). These set of Monte Carlo are generated with different values of absorbtion, symmetric and asymmetric scattering, and their timing distributions are compared to the data from the laser system in order to tune the amount of absorption, symmetric and asymmetric scattering in the calibration Monte Carlo. The way in which the  $\alpha_{\text{abs}}(\lambda)$ ,  $\alpha_{\text{sym}}$  and  $\alpha_{\text{asym}}$  are defined is shown in Equation 4.6.

$$\begin{aligned}\alpha_{\text{abs}} &= P_0 \times \frac{P_1}{\lambda^4} + C \\ \alpha_{\text{sym}} &= \frac{P_1}{\lambda^4} \times \left(1 + \frac{P_5}{\lambda^2}\right) \\ \alpha_{\text{asy}} &= P_6 \times \left(1 + \frac{P_7}{\lambda^4} \times (\lambda - P_8)^2\right)\end{aligned}\quad (4.6)$$

The term  $C$  in the equation for  $\alpha_{\text{abs}}(\lambda)$  is based on data from [29] for laser light with wavelengths greater than 464 nm while Equation 4.7 is used for wavelengths less than 464 nm.

$$C = P_0 \times P_2 \times (\lambda/500)^{P_3} \quad (4.7)$$

The values of  $P_0$  to  $P_8$  in Equations 4.6 and 4.7 were taken from fits to laser data taken in April 2009, the water coefficient functions of which are shown in Figure 4.12.

As well as the amount of absorption and scattering in the detector, there is also a dependence with respect to z-position in the detector, defined by Equation 4.8.

$$\alpha_{\text{tba}} = (\langle N_{\text{top}} \rangle - \langle N_{\text{bottom}} \rangle) / \langle N_{\text{barrel}} \rangle \quad (4.8)$$



Figure 4.11: Schematic of the laser system

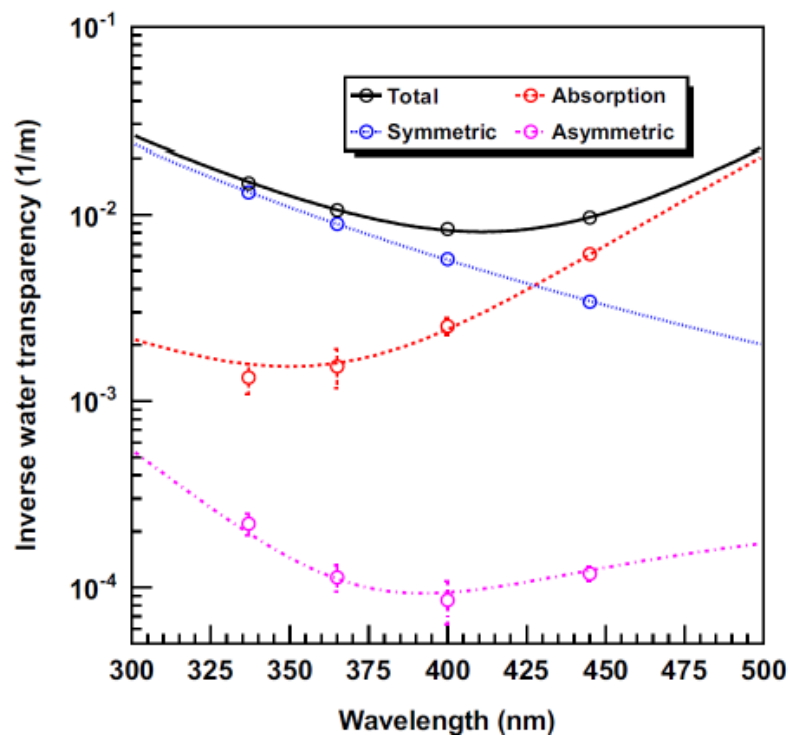


Figure 4.12: Plot of water coefficient functions used in Monte Carlo production, showing points for symmetric and asymmetric scattering and absorption.



Figure 4.13: Dependence of temperature on vertical position in the Super-Kamiokande ID.

Here  $\langle N_{\text{top}} \rangle$ ,  $\langle N_{\text{bottom}} \rangle$ ,  $\langle N_{\text{barrel}} \rangle$  are the averaged hit probabilities of the top, bottom and barrel PMTs, where  $\langle N_{\text{top}} \rangle$  is about 5% less than  $\langle N_{\text{bottom}} \rangle$  due to the temperature gradient in the tank. Figure 4.13 shows this dependence, and Equation 4.1.6 shows how this is taken into account for the absorption coefficient  $\alpha_{\text{abs}}$  by the factor  $A(z, t)$ :

$$\begin{aligned} A(z, t) &= 1 + z \cdot \beta(t) \quad \text{for } z \geq -11 \text{ m} \\ &= 1 - 11 \cdot \beta(t) \quad \text{for } z \leq -11 \text{ m} \end{aligned}$$

where from Figure 4.13, the value of  $A(z, t)$  is constant below  $z = -11 \text{ m}$ , and above  $z = -11 \text{ m}$  this value is determined by the z-position in the tank. The relationship between the value of  $\beta$  is related to the top-bottom asymmetry parameter  $\alpha_{tba}$ , and for the April 2009 data  $\alpha_{tba}$  and  $\beta$  are -4.91% and 0.01.

Chapter 5 expands upon these measurements by going into detail about the newly developed UK Light Injection system which improves upon the Korean laser system mentioned here used to make water coefficient measurements - it offers much narrower beam profiles which are shone onto the barrel regions, allowing for better analysis of the depth

dependence of the water coefficients.

# Chapter 5

## The UK Light Injection System

The UK calibration group's efforts have been focussed on improving the data analysis method and improving the accuracy of the water coefficient measurements. To aid this effort a new UK developed Light Injection (UKLI) system was installed into Super-Kamiokande during the refurbishment that occurred in the summer of 2018. This system has its own set of optics with multiple beam spot diameters and will be described in detail in this Chapter.

### 5.1 The UK Light Injection System Electronics and Optics

The electronics setup architecture for the UK Light Injection system is made of sixteen light emitting diode boards, where the light being pulsed by the LEDs has a wavelength of 435 nm and there is 1 LED per injector. Each LED is coupled to three optical fibres: one channel connected to a monitor PMT, one connected to an optical fibre that sends light into the Super-Kamiokande detector, and one is a spare.

Unlike the Korean laser system mentioned in Chapter 4 which injects light into the detector using an optical fibre which has an opening angle of 12 degrees, the UK Light Injection system contains three different types of light injection optics, with each having a different opening angle: a bare fibre, a collimator and a diffuser. This range of optics can accommodate a larger variety of calibration measurements, and better suit the multiple applications of the light injection system.



Figure 5.1: Collimator schematic including the end-cap, lens mount and mounting sleeve structures.



Figure 5.2: Photograph of the diffuser by itself (left), empty diffuser enclosure (centre) and diffuser inside enclosure (right).

### The Collimator Optic

A 2-degree opening half angle is achieved by the collimator optic by using a GRIN (gradient-index) lens [30] to reduce the opening angle of the light coming from the fibre optic. A schematic of the collimator design can be seen in Figure 5.1.

### The Diffuser Optic

The diffuser optic is a wide angled beam with a opening half-angle of 40 degrees, allowing for more PMT coverage in the detector, therefore enabling measurements of PMT properties, and measurements of light attenuation length in water. Figure 5.2 shows a photograph of one of the diffusers used, and one of the diffuser ball enclosures. The enclosure is made of high grade stainless steel and using a chemical and water resistant epoxy resin, so all the components were ensured to be watertight.

### Bare Fibre and Optical Plate

The bare fibre injector are 1 mm step index fibres, and are approximately 20 cm in length and are used for validation purposes with the bare fibres in the Korean optical calibration



Figure 5.3: Photograph of the optical plate which houses the different optics.

system. These short fibres are screwed into the back end of the optical plate that the collimator and diffuser optics are mounted on, shown in Figure 5.3.

## 5.2 Optics test stand measurements

In order to test the collimator and diffuser optics, measurements of the angular distributions were made using diffuser and collimator test-stands and would measure angular distributions of the light intensity. The setup for the collimator test stand at the University of Warwick is shown in Figure 5.4 and captures the beam cross section by moving a CMOS camera along the beam width. For the diffuser test-stand the angular distribution of the light output was measured using the setup shown in Figure 5.6. This test stand setup for the diffuser optics consists of a test diffuser ball placed inside a diffuser enclosure, a rotation stage which allows for the movement of the diffuser between -40 and 40 degrees,



Figure 5.4: Setup of the collimator test stand provided by Warwick University

and a PMT used for pulse intensity measurement set up 250 mm away from the diffuser. An optical fibre couples the diffuser under test to a laser set to a wavelength of 450 nm.

Figure 5.5 shows fits made by ROOT to the light profiles for the collimator. The angular distributions shown give the distribution of the polar angle in degrees of light intensity which are relative to the virtual position from which the light cone originates, averaged over all the orientations of the azimuthal angle.

Figure 5.7 shows distributions provided by this test stand data which are preliminary fits made by ROOT to the light profiles for the diffuser. These distributions are not phi-averaged, and instead are scans across the front of the diffuser.

### 5.3 First commissioning data from UKLI

In September of 2019 and November of 2019 two sets of test data were taken of the collimator, the diffuser and the bare fibre optic (the B2 bare fibre) and using an event display developed by the University of Warwick, occupancy plots of the test data sets were produced. Figure 5.8 shows the occupancy plots for the collimator optic from the November 2019 dataset showing the beam spot inside the unrolled volume of the Super-Kamiokande detector. Similarly, Figure 5.9 shows the occupancy plots for the diffuser optic from the November 2019 dataset. The graph in the bottom right hand corner of the occupancy plots show the corrected time-of-flight plots for the PMT hits from the injector.

Figure 5.5: Light profiles for the collimator optics provided by The University of Warwick





Figure 5.6: Setup of the diffuser test stand provided by Warwick University

The UKLI was also added to the “autocalib” system used for long term monitoring of the water parameters in Super-Kamiokande by the Korean laser system. In early 2020 the autocalib scheduler was modified to incorporate data taking by the UKLI system which was very useful for gadolinium loading calibration purposes but also in the longer term, it will be useful in the monitoring of daily/weekly water coefficient property measurements, investigation of depth dependence with respect to the water properties and PMT property calibration. Figure 5.10 shows the schedule for autocalib, and the black dashed lines show the position of the UK barrel collimator and diffusers with respect to the other autocalib data taking streams. The horizontal blue line shows the length of the one autocalib cycle, which is about 4.6 seconds, with each UKLI optic taking about 3310 events per day. The intensely dark purple hits in Figures 5.8 and 5.9 are ”hot channels” and have not been accounted for - these should not be mistaken for scattered hits.

Figures 5.12 shows the occupancy plots for autocalib data taken in July 2020, for the B1 collimator (left) and the B1 diffuser (right). From this point onwards all plots relating to the B2 - B5 injectors for both the collimators and diffusers will be shown in Appendix A. As can be seen in the text in the upper left hand corner, the number of events in the run is a lot less than the 100,000 events or so taken in the test runs, however they are more than sufficient for monitoring purposes.

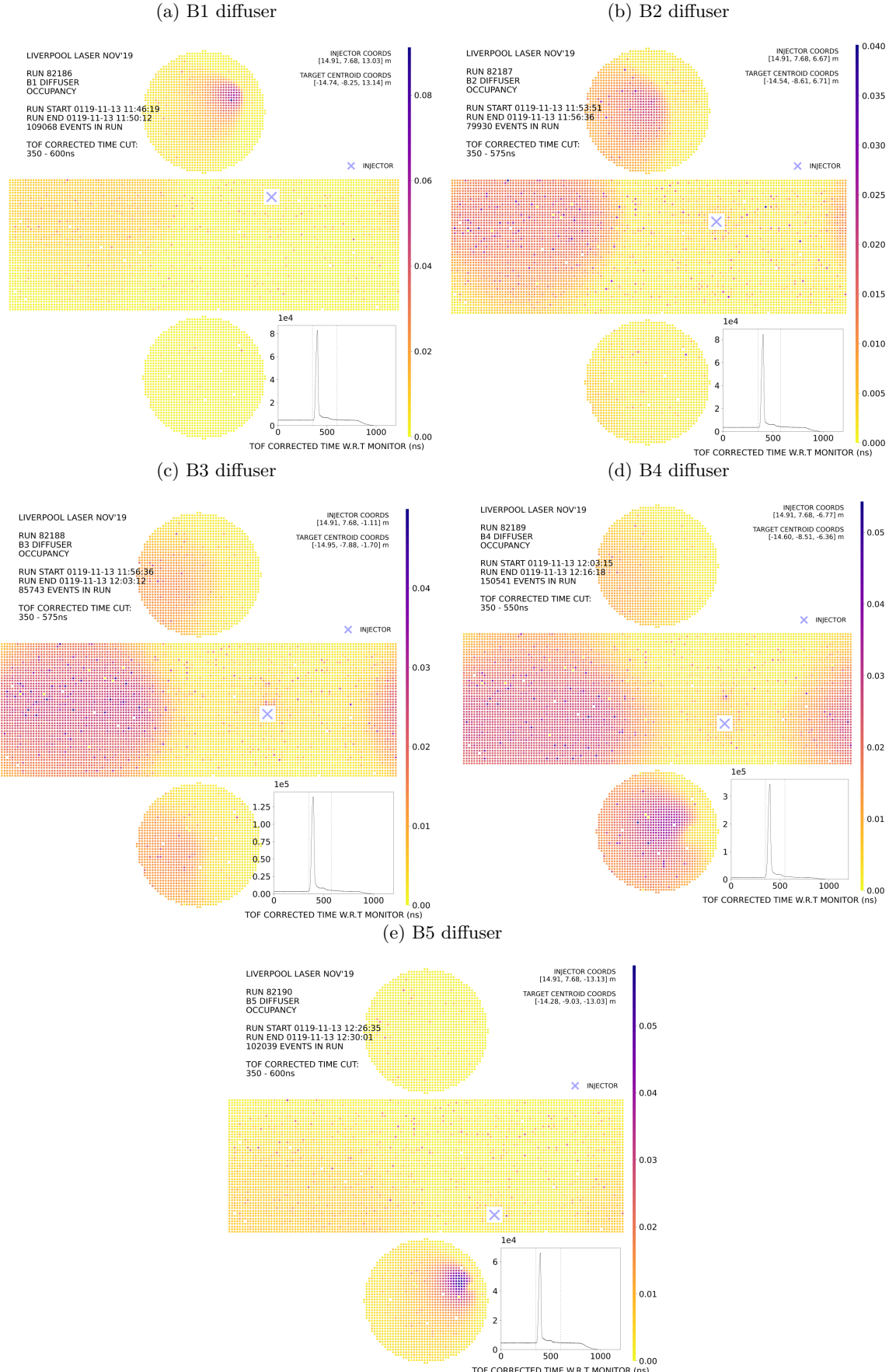
Figure 5.7: Light profiles for the diffuser optics provided by The University of Warwick



Figure 5.8: Occupancy plots for the collimator optics from the UKLI November 2019 test run



Figure 5.9: Occupancy plots for the diffuser optics from the UKLI November 2019 test run



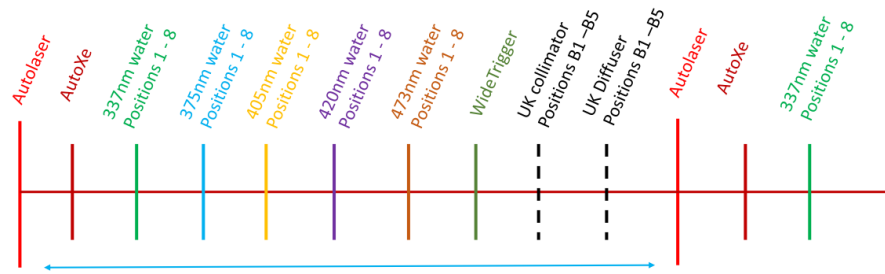


Figure 5.10: Schematic showing position of the UKLI in autocalib scheduler: the black dashed lines show the UKLI B1-B5 collimator and diffuser optics and the horizontal blue line shows the length of one autocalib cycle.



Figure 5.11: Occupancy plot for the B1 collimator optic from the UKLI Autocalib July 2020 run



Figure 5.12: Occupancy plot for the B1 diffuser optic from the UKLI Autocalib July 2020 run

## 5.4 Implementation of UKLI in SK Simulation

In order to simulate the data taken with the UKLI, SKDETSIM, the Super Kamiokande Detector Simulator was used. SKDETSIM uses GEANT3 (GEometry ANd Tracking 3 [31]) to simulate what the particles in each event would do inside the detector, and tracks the particle's trajectories and energy loss. Simulating the light injection from the UKLI system in SKDETSIM was done in a similar way to the Korean method of producing Monte Carlo: the same versions of the calibration scripts were used, however, small modifications were made to them and to the version of SKDETSIM used to simulate the input photons from the system in the detector. The calibration software allows for the number of events and the number of injected photons to be set, in order to generate many Monte Carlo files with varying absorption, Rayleigh and Mie scattering parameters.

Along with making sure the position of the injectors was set to that of the UKLI injectors (shown in Table 5.1), the opening angle of the injectors determined by the simulation had to be set to accomodate the fact that the injectors for the UKLI system now consisted of three different opening angles for the collimator, diffuser and bare fibre optics. Previously, to set the angle of the photons in the beam, a parameter relating to the width of the input injector beam was produced using a Gaussian random number generator to output the photon angle. However, an entirely new method of determining the opening angle of the beam was needed to include the information from the light profiles taken from the test stands at Warwick.

UKLI Barrel Injector	x (cm)	y (cm)	z (cm)	Misalignment angle (°)
B1	1490.73	768.14	1224.0	4.1
B2	1490.73	768.14	742.0	3.5
B3	1490.73	768.14	-200.0	3.4
B4	1490.73	768.14	-747.0	6.3
B5	1490.73	768.14	-1413.0	-

Table 5.1: Beam spot positions (x,y,z) of the UKLI injectors in cm and misalignment of the injectors in degrees

In order to validate the positions of the targets for the UKLI system, and the relationship between the width of the beam and the output angle, producing charge weighted histograms from UKLI test runs is very helpful. It allows us to explore the shape of the



Figure 5.13: Charge weighted z profile plots for the B1 collimator UKLI injector optic

beam profile and intensity. Figures 5.13 and 5.14 shows the charge weighted z-profiles for the September and November 2019 datasets for the B1 and B4 collimator injectors, where the blue dashed line shows the expected target position. These are produced by selecting hit PMTs which are greater than 2 m away from the injector (to avoid including PMT hits from backscattered light), and filling the histogram with the z-position of the hit PMT and the number of hits the hit PMT receives multiplied by the corrected charge from the PMT. The corrected PMT charge is calculated using Equation 5.1, where the gain correction value is taken from official Super-Kamiokande gain tables. By fitting these charge weighted histograms with a gaussian and calculating its mean value (i.e. the actual target location), it was possible to calculate the deviation from the expected target location (the dashed blue lines in Figures 5.13 and 5.14), and then using simple trigonometry the misalignment angle of the injector was calculated, as shown in Table 5.1.

$$q/(1 + \text{gain}) \quad (5.1)$$

The profiles from the Warwick optic test stands (shown in Figures 5.5 and 5.7) are then used in the production of the opening angle of the injectors in the detector simulation. This was done by treating the profiles in Figures 5.5 and 5.7 as Probability Distribution Functions (PDFs) and using inverse transform sampling to make the detector simulation sample at



Figure 5.14: Charge weighted  $z$  profile plots for the B4 collimator UKLI injector optic

random from it. Inverse transform sampling is a method for generating random numbers from any probability distribution by using the inverse of its cumulative distribution  $F^{-1}(x)$ . For continuous distributions, such as the results from the collimator and diffuser optics test stands, the algorithm for inverse transform sampling is simple. Firstly, a random variable  $U$  is uniformly distributed between  $[0,1]$ , and secondly the relation  $X = F_x^{-1}(U)$  would then produce a distribution  $X$  following the original probability distribution function, i.e. that of the original PDFs from the optics test stands.

The first step is to produce the CDFs from the PDFs from the optic test stand profile tests. Figure 5.5 shows that the original fits to the collimator data did not reach 4 degrees, and as a result the PDFs produced needed to be linearly extrapolated from 3.5 degrees where the measurements cut off to reach 4 degrees. Figure 5.15 shows the PDFs and CDFs produced from the B1 collimator data and Figure 5.16 shows them for the B1 diffuser data. The CDFs are normalised with a max of one using min-max scaling.

After producing the normalised CDFs, the inverse of these CDFs are calculated - Figure 5.17 shows the comparison of the normalised CDF data for the B1 collimator and diffuser (top sublots, shown in blue) and the polynomial fit to the CDF for the B1 collimator (top subplots, shown in red), and the inverse CDF function (bottom subplots shown in green) and the polynomial fit to this inverse CDF function (bottom subplots shown in purple).



Figure 5.15: PDF (left) and CDF (right) for the B1 collimator

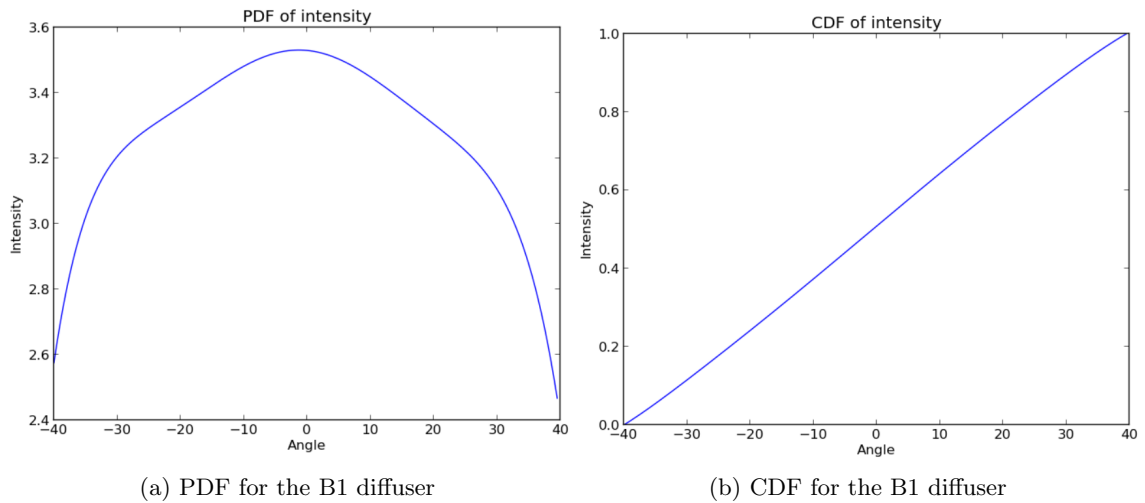


Figure 5.16: PDF (left) and CDF (right) for the B1 diffuser



Figure 5.17: Inverse CDF for the B1 collimator (left) and for the B1 diffuser (right)

After producing the fits to the inverse cumulative distribution functions, these functions were inputted into the detector simulation, SKDETSIM. Using the same event display used to produce the occupancy plots for the autocalib data and the test run data, occupancy plots of the Monte Carlo were produced. These are shown for the B1 collimator and B1 diffuser in Figure 5.18. These MC were produced with the standard optical settings used for SKDETSIM. Because the original profiles from the test stands were taken in air, adjustments were made so that the refractive index of the water in the detector is taken into account when implementing the inverse CDFs into the detector simulation.

In order to validate the diffuser MC inverse cumulative distribution function output, a uniform distribution was run through the equation for the diffuser inverse CDF fits and the original PDF fit for each diffuser was used to fit the output points from the distribution, showing that inverse transform sampling was done correctly for the PDFs. This is shown for the B1 diffuser in Figure A.11.

After producing the UKLI MC, adjusting the timing distributions in order to match up with the UKLI test run data was the next step. Producing time-of-flight corrected plots for the B1 collimator UKLI MC and overlaying it with the Run 82181 November test run data with the standard optical parameters, it was clear that there are disagreements between the Monte Carlo and data in both the scattered hits region and the reflected hits peak. In order to change this, the time dispersion of the injected photons in the MC was varied, in order to match the time dispersion of the injected photons in the data.

The time dispersion for the injected photons in the laser generation in SKDETSIM is

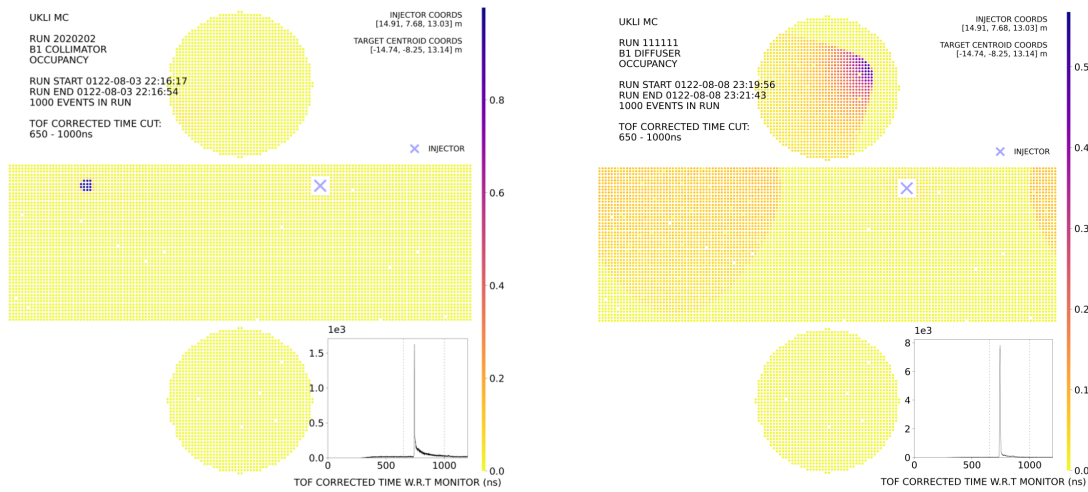


Figure 5.18: Monte Carlo simulations of the B1 collimator (left) and diffuser (right) injectors

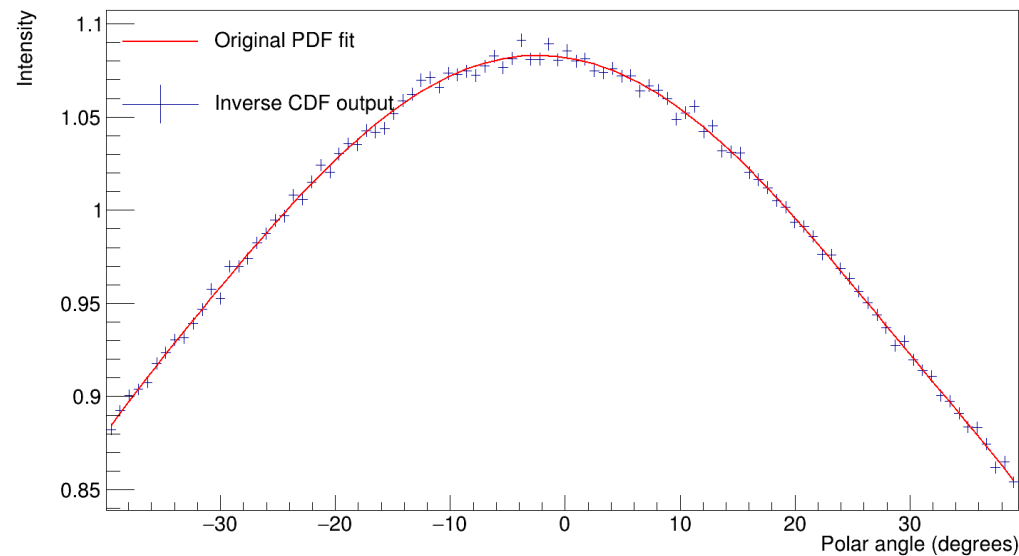


Figure 5.19: B1 diffuser inverse CDF check

governed by a Gaussian distributed random number generated using a Box-Muller transform, where additional time dispersion added would be the sigma of this Gaussian, and after a random number is passed through it, the output number would be added to the time for each track step of the photon giving the time dispersion.

The Box-Muller transform is a random number sampling method for making pairs of independent, normally distributed random sources from a source of uniformly distributed numbers (from between usually from between 0 and 1) [32]. The form of the Box-Muller method implemented to calculate the added time dispersion is the Marsaglia polar method [33], which works by choosing two independent and uniformly distributed numbers ( $u, v$ ) between  $[-1, +1]$ , so that  $s = u^2 + v^2$ , and if  $s = 0$ , or  $s >= 1$ , another pair of numbers are chosen. Then the standard normal deviate which is given by

$$z_0 = u \cdot \sqrt{\frac{-2 \ln s}{s}}$$

is multiplied by the chosen value of time dispersion in seconds and added to the mean (set to zero) to give the normally dispersed extra track step time for a photon in the distribution.

Figure 5.20 shows the effect of implementing this varying time dispersion on the raw hit timing output from the UKLI MC B1 collimator simulation, with the time dispersion shown for 0 ns, 5 ns, 10 ns, 15 ns and 20 ns.

In order to properly compare the timing distributions between data and Monte Carlo, the time-of-flight corrected timing plots are produced. To only select reflected and scattered hits, an exclusion region of hits is set: this is set to be  $\pm 2$  m around the injector (in order to avoid using backscattered hits in the analysis), and also  $\pm 3.2$  m around the injector target region in order to avoid including direct hits to the beam target. Figure 5.21 shows the regions for the hits which are included and excluded in order to produce the TOF corrected timing distributions.

Figures 5.22, 5.23, 5.24, 5.25, 5.26 show time-of-flight corrected hit timing distributions for the B1 injector. The region between the blue dashed lines are the region for the scattered hits and the peak on the right shows the reflected hits. The hits from the injector data are shown in black and the MC hits are shown in red. In order to find the closest match for the time dispersion in the data, a gaussian distribution was fit to the B1 collimator data and Monte Carlo reflected peaks and the width of the gaussian was compared - this was only done for the 10 ns, 15 ns and 20 ns dispersion plots because the value for the time



Figure 5.20: Gaussian distributed time dispersion plots, with varying amounts of time dispersion

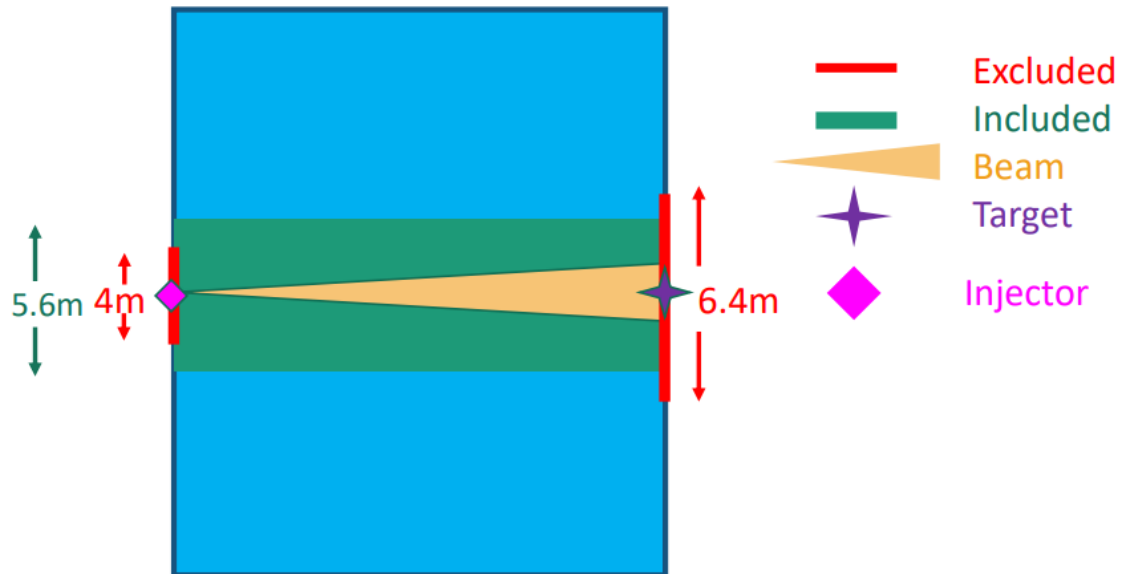


Figure 5.21: The included (green) and excluded (red) regions for the TOF timing distributions



Figure 5.22: TOF comparison between UKLI MC with no time dispersion and Run 82181 test data for B1 collimator

dispersion for the LED pulse is known to be in this range and the peak is too narrow and uneven for the 0 ns and 5 ns dispersion plots to fit a gaussian properly. The reason for the variation in the height of the reflected peaks between the MC and data is due to the detector response, which is why the width is being focussed on here instead.

The sigma of the gaussian fit to the data is  $14.07 \pm 0.01$  ns, while the gaussian fit to the reflected peak for the 10 ns, 15 ns, and 20 ns time dispersed MC distributions is shown in Table 5.2.

Time dispersion value (ns)	Sigma of gaussian (ns)	$\chi^2/ndf$ values of scattered hits region
0	—	8.15
5	—	4.72
10	$19.94 \pm 0.39$	3.45
15	$30.30 \pm 0.55$	13.17
20	$38.46 \pm 0.75$	22.12

Table 5.2: Sigma of gaussian (ns) for each value of time dispersion along with the  $\chi^2/ndf$  value for B1 data and MC comparison between the scattered hits region (blue dashed lines)



Figure 5.23: TOF comparison between UKLI MC with 5 ns gaussian time dispersion and Run 82181 test data for B1 collimator



Figure 5.24: TOF comparison between UKLI MC with 10 ns gaussian time dispersion and Run 82181 test data for B1 collimator, with a gaussian fit to both

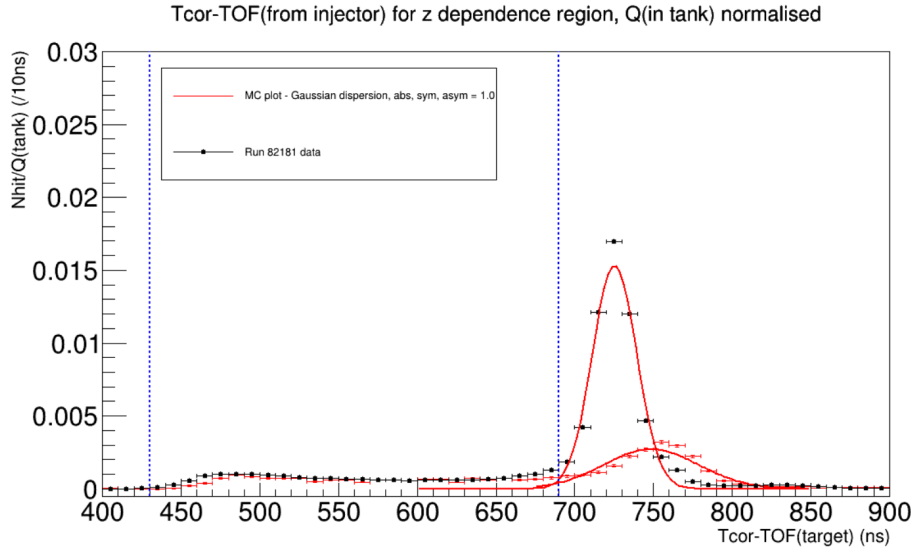


Figure 5.25: TOF comparison between UKLI MC with 15 ns gaussian time dispersion and Run 82181 test data for B1 collimator, with a gaussian fit to both

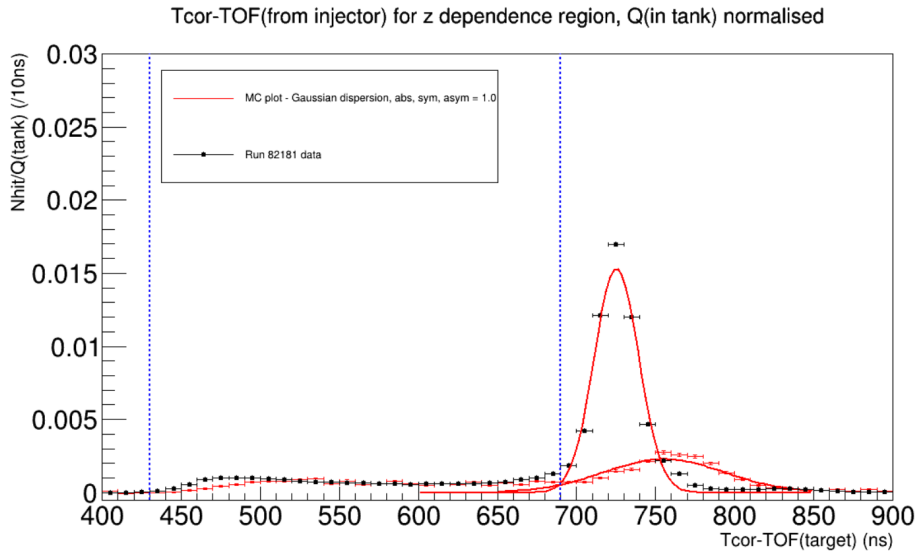


Figure 5.26: TOF comparison between UKLI MC with 20 ns gaussian time dispersion and Run 82181 test data for B1 collimator, with a gaussian fit to both

From Table 5.2 it can be seen that the 10 ns dispersion had the closest value to the B1 data for the sigma of the gaussian fit to the reflected peak, and also the lowest  $\chi^2/ndf$  value for the comparison between the data and MC for the scattered hits region, showing that this 10 ns dispersion was the best to use in the MC. In order to improve this part of the analysis, the scale of the time dispersion values could be more granular, for example, zooming into the 5 - 10 ns range when producing MC in order to more accurately determine the value of the time dispersion for the collimator data.

To summarise the work in this Chapter, data from test stands using the same optics used in the UKLI in Super-Kamiokande were used to produce probability and cumulative distribution functions of the optic light profiles. These were implemented into the Super-Kamiokande detector simulation, and inverse transform sampled in order to produce UKLI MC beam spot outputs which were fitted with the original PDFs to verify the output. Alongside this, in order to better align the hit timing distributions for the MC and data, modifying the track step of the photon in the simulation was used to vary the time dispersion of the hits from the injector. The width of the reflected hits peak in TOF corrected timing distributions was determined with a gaussian fit, and compared with the B1 collimator data, along with a comparison of the difference in hit times in the scattered hits region, which allowed us to determine the optimal value for time dispersion of injected hits was 10 ns.

## Chapter 6

# Neutron Tagging and NCQE Interactions with the SK-Gd Upgrade

At energies close to the atmospheric peak, the NCQE interaction cross sections can be evaluated using T2K beam neutrinos. This chapter will present the status of the improved neutron tag from SK-Gd, its impact on the measurement of NCQE in T2K and the improvements to the SRN background measurement. The prompt and delayed signal of the NCQE interaction mimics that of the DSNB, due to the positron being the prompt signal for DSNB, while the prompt signal for NCQE is given by a gamma ray. Neutron capture constitutes the delayed signal for both SRN and NCQE interactions. With the recent addition of 0.026%  $\text{Gd}_2(\text{SO}_4)_3 \cdot 8\text{H}_2\text{O}$  to Super-Kamiokande, neutron detection has improved due to the gamma cascade signal produced when neutrons are captured on gadolinium.

There are multiple stages to this analysis, shown in Figure 6.1, where the “neutron tagging” stage occurs via two methods. Previously the NCQE neutron-tagging analyses used a method for neutron tagging which will be referred to as “legacy NTag code”, but in 2020 the Super-K collaboration decided to proceed to use a new, more compact and streamlined version, which combines most of these stages into one piece of software. This will be referred to as “current NTag code”, and this is shown in Figure 6.1 as well. The red arrows in Figure 6.1 show the steps in the analysis procedure using the legacy NTag code which have been assimilated into the new NTag code.

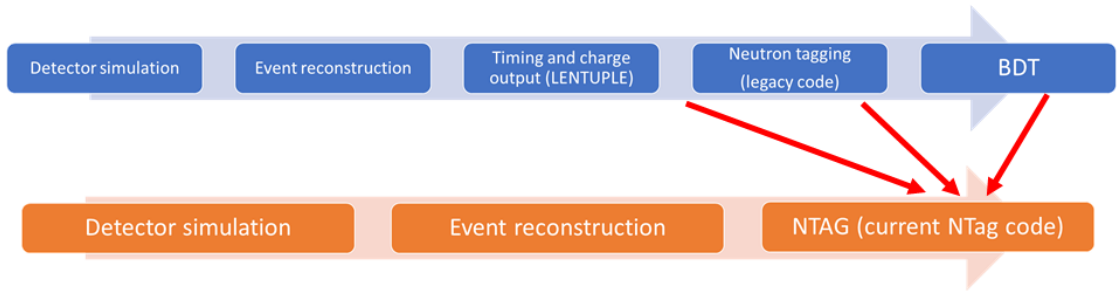


Figure 6.1: Flowchart showing the stages in this analysis for both the analysis which used the legacy Ntag code (blue) and the current NTAG code (orange).

Name	Version
Flux	13 a tuning v4.0
NEUT	5.3.3
SKDETSIM-SKGd	ANNRI-Gd model
Geant	4.10.05.p01
T2KReWeight	v1r23
GENIE	R2-12-10

Table 6.1: Software versions used in analysis from [34].

A large portion of this analysis was to validate the results regarding the prompt event reconstruction and the neutron truth information between the legacy NTAG and the new NTAG - while the general neutron tagging algorithm was the same, the complete rearrangement of the structure of the NTAG code required there to be checks regarding event reconstruction variable output and true neutron information variables such as the number of neutrons captured and the position in the detector the neutron captures occur at which will be shown later on in this Chapter.

## 6.1 Event Simulation

This section discusses details about the event simulation, specifically the way neutrino interactions are simulated in order to produce the Monte Carlo. Table 6.1 summarises all the software packages used in this analysis.

### 6.1.1 Neutrino flux

As mentioned in Chapter 2, the T2K neutrino beam is generated by having a 30 GeV proton beam impinge on a graphite target, where the pions and kaons that result from this decay, producing in anti(neutrinos). Neutrino event rates measured at Super-Kamiokande are compared to Monte-Carlo predictions stemming from flux calculations. Prior to data from the NA61/SHINE experiment, the flux was predicted from hadron production models which were tuned to data which produced large systematic uncertainties. However, the NA61/SHINE experiment provides direct hadron production measurements for T2K and other long baseline experiments, and measures the yield of charged hadrons from a proton beam fired at a thin graphite target (2 cm long) and a T2K replica graphite target (90 cm long). From this experimental data, Monte Carlo simulations of the neutrino flux are predicted. In the beam MC, protons which have 30 GeV of kinetic energy are focused onto a graphite target and after the secondary particles are focused using the horn magnets, the neutrino tracks they decay into are ascertained at the near detectors and at Super-Kamiokande to produce the flux and energy spectra at both of these locations. The T2K neutrino beam flux version used in this analysis is 13a tuning v4.0 which uses the NA61/SHINE 2009 Replica-Target Data [35]. Figure 6.2 shows the energy spectra of each of the neutrino flavour components for the FHC (forward horn current) mode for the T2K Run 1-9 period.

The oscillation effect on the neutrino flux also needs to be considered after choosing which flux to use: the neutrino-oxygen NCQE cross section does not depend on flavour, and therefore neutrino oscillation affects would have no impact on a fully pure NCQE sample. However, there is a small fraction of charged current events which seep into the NCQE sample, and oscillation weights need to be applied to the charged current events in the sample. The entire Monte Carlo is reweighted as if it was fully comprised of muon and muon anti-neutrinos, due to the very small presence of electron neutrinos. Equation 6.1 shows the event weight applied to charge current events for the 2-flavour (electron neutrino and muon neutrino) scenario.

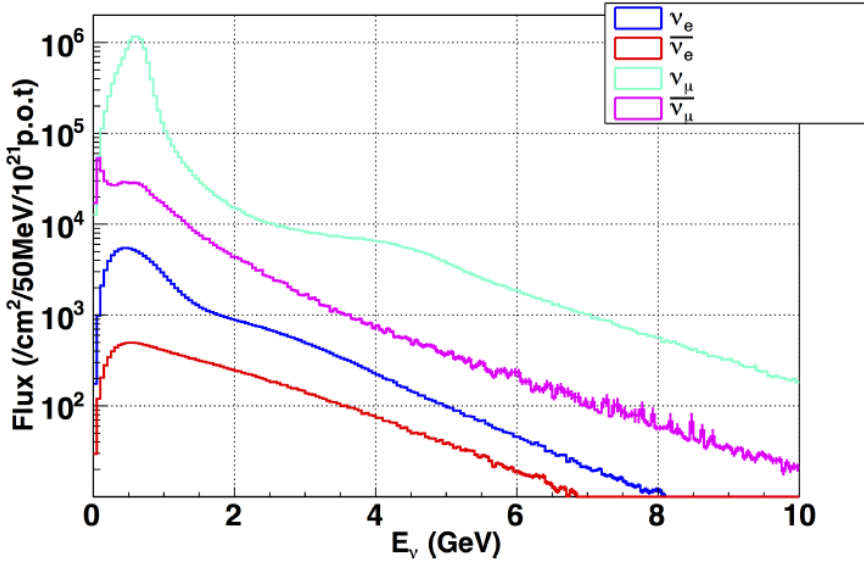


Figure 6.2: Energy spectra of the  $(\nu_e, \bar{\nu}_e, \nu_\mu, \bar{\nu}_\mu)$  flavour components for the FHC mode, T2K Run 1-9.

Osc Parameter	Value
$\sin^2 \theta_{13}$	$0.0211 \pm 0.0008$
$\sin^2 \theta_{23}$	$0.541^{+0.027}_{-0.037}$
$ \Delta m_{32}^2 $	$2.469^{+0.073}_{-0.071} \times 10^{-3} \text{ eV}^2$

Table 6.2: Oscillation parameters estimated with the reactor constraint.

$$\begin{aligned}
 \text{weight } (E_\nu) &= P_{\nu_\mu \rightarrow \nu_\mu}(E_\nu) + P_{\nu_\mu \rightarrow \nu_e}(E_\nu) \times \underbrace{\frac{\sigma_{\nu_e CC}(E_\nu)}{\sigma_{\nu_\mu CC}(E_\nu)}}_{\approx 1} \\
 &\approx P_{\nu_\mu \rightarrow \nu_\mu}(E_\nu) + P_{\nu_\mu \rightarrow \nu_e}(E_\nu) \\
 &= 1 - \cos^4 \theta_{13} \times \sin^2 2\theta_{23} \times \sin^2 \left( 1.267 \frac{\Delta m_{32}^2 [\text{eV}^2] \cdot L [\text{km}]}{E_\nu [\text{GeV}]} \right)
 \end{aligned} \tag{6.1}$$

where the cross-section ratio term is simplified to 1 due to the kinematic difference between  $e^\pm$  and  $mu^\pm$  not being considered. Table 6.2 shows the oscillation parameters used in Equation 6.2 which are estimated with the reactor constraint taken from [36].

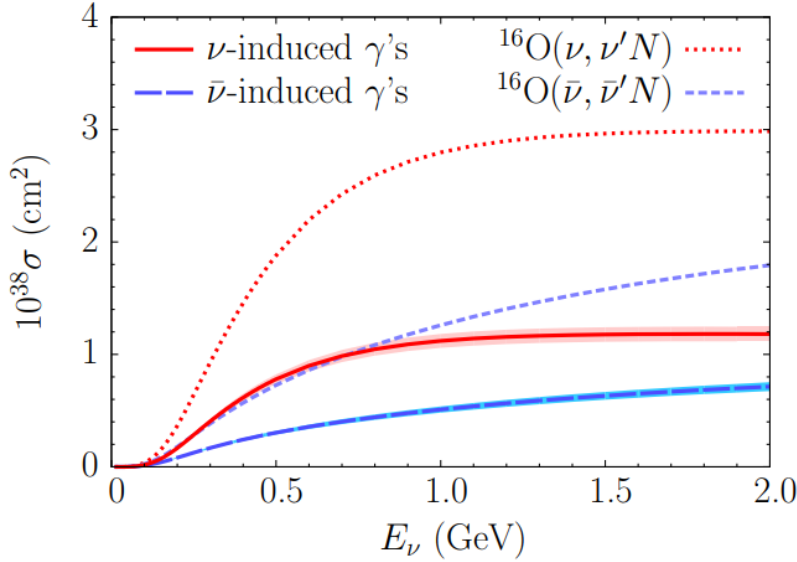


Figure 6.3: Plot showing the NCQE cross section for  $^{16}\text{O}$  as a function of incoming neutrino energy and the cross section of gamma ray production, taken from [37].

### 6.1.2 Primary interaction

The interaction between the incoming neutrino event and an Oxygen nucleus, and the de-excitation of the nucleus is modelled by NEUT, which produces a vector of primary particles used for event simulation in SKDETSIM. Because these are primary particles, they do not take into consideration all the particles produced from the detector response, i.e. the secondary particles produced from the interactions within the medium of the detector, in our case, water doped with  $\text{Gd}_2(\text{SO}_4)_3 \cdot 8\text{H}_2\text{O}$ . The way NEUT treats the interaction between a nucleus and a neutrino for the case of a neutrino interaction with a  $^{16}\text{O}$  isotope is shown in Figure 6.3.

NCQE interactions are modelled in NEUT using the Benhar Spectral Function (SF), while CCQE interactions (including 2p2h interactions) are modelled using the Relativistic Fermi-Gas (RFG) model [38], [39]. 2p2h interactions (2-particle-2-hole) involve a neutrino knocking nucleons out of a nucleus and creating two holes.

The lowest rung of nucleons in Figure 6.4 is the  $s_{1/2}$ , with  $p_{3/2}$  above this level and  $p_{1/2}$  above that. The protons in these rungs have removal energies of 42 MeV, 18.4 MeV and 12.1 MeV respectively, and due to neutron levels being more tightly bound, these have

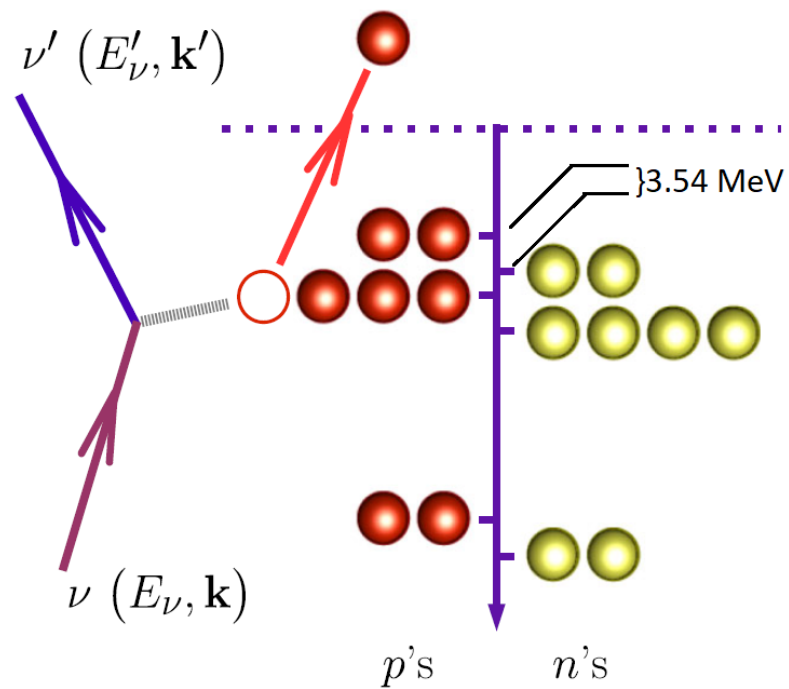


Figure 6.4: Representation of NC neutrino scattering off  $^{16}\text{O}$  with protons on the left hand side and neutrons on the right arranged according to the shell model.

	$(s_{1/2})^{-1}$	$(p_{3/2})^{-1}$	$(p_{1/2})^{-1}$	others
Shell model	0.25	0.5	0.25	0
Spectral Function	0.1055	0.3515	0.158	0.385
This analysis	0.4905	0.3515	0.158	0

Table 6.3: Transition probabilities for different models and states

an extra removal of 3.24 MeV compared to their proton counterparts. The shell model is imperfect due to how it allocates the probability of  $^{16}\text{O}$  transitioning to the possible nucleon states. In the shell model, probabilities are allocated by counting the number of nucleons in each energy level and assigning probabilities according to how many there are. In Figure 6.4 it can be seen that the  $p_{3/2}$  state has double the number of nucleons compared to the  $s_{1/2}$  model and therefore double the probability of transition is assigned for the  $p_{3/2}$  state, and the probability of transitioning to any other state is assigned to be 0, because in the shell model they don't even exist. The Benhar Spectral Function model however is complex and is tuned using electron-nucleus scattering data. The model used in this analysis is a modified version of the Benhar Spectral Function model, where the case of other transition states is dealt with by merging the “others” state into the  $s_{1/2}$  state. Table 6.3 gives the probabilities of transition to different states for different models.

### 6.1.3 Detector response and interactions in the detector medium

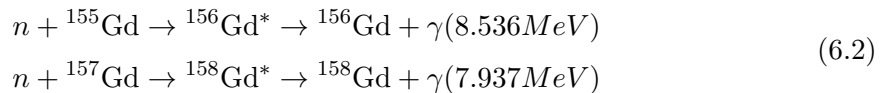
Prior analyses to this used SKDETSIM (Super-Kamiokande Detector Simulator) to simulate the trajectories of particles through the water in Super-Kamiokande and output detector response MC. This analysis uses SKDETSIM-SKGd to propagate the particles, due to the requirement of needing gadolinium sulphate present in the simulation. Unlike SKDETSIM, SKDETSIM-SKGd has a GEANT4 function implemented for neutron capture on gadolinium isotopes and its subsequent interactions. The particular isotopes of gadolinium used in the simulation are  $^{155}\text{Gd}$  and  $^{157}\text{Gd}$  due to their excellent thermal neutron capture cross sections. Table 6.4 shows the relative abundance of various gadolinium isotopes inside natural gadolinium and their associated thermal neutron capture cross sections.

As can be seen in Table 6.4, not only are  $^{155}\text{Gd}$  and  $^{157}\text{Gd}$  have extremely high neutron capture cross sections compared to the other isotopes. Equation 6.2 shows the neutron

Isotope	Abundance [%]	Cross-section [b]
$^{152}\text{Gd}$	0.200	735
$^{154}\text{Gd}$	2.18	85
$^{155}\text{Gd}$	<b>14.80</b>	<b>60900</b>
$^{156}\text{Gd}$	20.47	1.8
$^{157}\text{Gd}$	<b>15.65</b>	<b>254000</b>
$^{158}\text{Gd}$	24.84	2.2
$^{160}\text{Gd}$	21.86	1.4

Table 6.4: Abundance and thermal neutron capture cross section of various isotopes of Gadolinium

capture on both of these isotopes, and the energy of the subsequent gamma rays.



It is important to therefore model the gamma ray emission spectra from both of these isotopes. The model used by SKDETSIM-SKGd is the ANNRI-Gd model, [40], [41]. This uses gamma energy spectrum data from the germanium spectrometer at the ANNRI (Accurate Neutron Nucleus Reaction Measurement Instrument) experiment. This experiment uses the incoming pulsed neutron beam from the Japan Spallation Neutron Source (JSNS) at the Material and Life Science Experimental Facility (MLF) of J-PARC. After a 300 kW beam of protons from the JSNS facility hits a target of mercury and produces neutrons, this neutron beam hits an enriched  $^{155}\text{Gd}$  target or a  $^{nat}\text{Gd}$  film. The ANNRI spectrometer is placed 21.5 m away from the neutron beam source, with two cluster detectors on either side of the neutron capture target material, which is 13.4 cm away from each cluster detector. Surrounding the target, there are also 8 co-axial germanium detectors. The schematic for the ANNRI-Gd experiment is shown in Figure 6.5.

Figure 6.6 shows the energy spectra for different multiplicity values (left) and hit values (right) from one of the germanium crystals in the ANNRI spectrometer.

One of the key differences between the default Geant4 model for thermal neutron capture on Gadolinium and the ANNRI-Gd model is how it conserves energy: the photon evaporation model conserves only the final sum of energy for the captured event, but per-

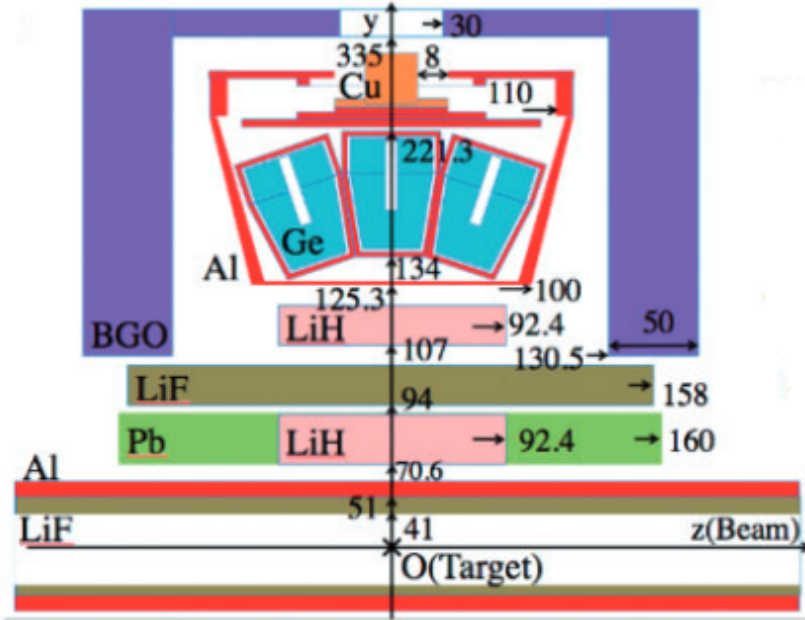


Figure 6.5: Schematic of the ANNRI Ge spectrometer (dimensions in mm). The beam pipe along with one of the Ge cluster detectors (light blue) is shown. The shaded purple area are the anti-coincidence shields made of bismuth-germanium-oxide (BGO) crystals [40].

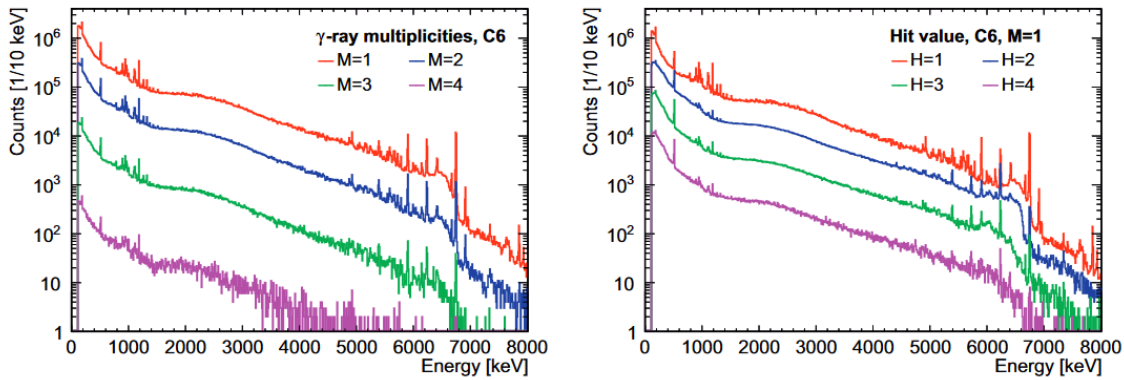


Figure 6.6: Energy spectra for thermal neutron capture on  $^{157}\text{Gd}$  energy spectra for different multiplicity values (left) and hit values (right) from one of the germanium crystals in the ANNRI spectrometer. Taken from [40].

forms poorly when modelling the gamma-ray energy on an individual event by event basis. One way the ANNRI-Gd model combats this is by separately describing the continuous and discrete peaks in Figure 6.6, where the discrete peaks are shown as spikes below 1500 keV and above 4500 keV. These come from the different ways in which gadolinium de-excites after thermal neutron capture. The continuous spectrum in the plots in Figure 6.6 show the de-excitation of  $^{158}\text{Gd}^*$  in multiple steps, producing multiple low energy gamma rays, which accounts for about 93% of the spectrum. The discrete spikes in the spectra come from a two-step cascade, which produces a high energy gamma ray instead, accounting for the remaining 7% of the spectrum. Figure 6.7 shows the continuous and discrete components of the ANNRI-Gd MC, along with data from the experiment. Figure 6.8 shows ratio plot of data and MC for the GLG4sim model, the default Geant4 photon evaporation model and the ANNRI-Gd model: here it is clear the ANNRI-Gd model fits the data better than the other two models, especially at energies above 3500 keV. The energy from the neutron capture on Gadolinium de-excitation is released in the form of multiple gamma rays, and liquid scintillator detectors would only have to look for the deposition of the energy from these gamma rays, whereas a water Cherenkov detector such as Super-Kamiokande can only detect part of this deposition due to the Cherenkov threshold energy. As a result, understanding the gamma ray multiplicities and their energies in the range 0.8 MeV to 8 MeV is important in order to predict the efficiency of neutron tagging within Monte Carlo simulation.

## 6.2 Event Reconstruction

### 6.2.1 Bonsai output reconstruction quantities

Due to this analysis looking specifically at the low energy region, a fitter (LOWFIT) specific to low energies (below 100 MeV) is used to reconstruct events. Both MC and data neutrino events undergo a reconstruction phase, where the low-energy fitter BONSAI is applied to the event, as discussed in Chapter 2. The reconstruction is carried out using timing and PMT position information, however charge information is omitted - this is because of only a couple photoelectrons being produced by each PMT, so it makes sense to count the number of hit PMTs instead. The output of BONSAI gives information which will be used in the reduction phase of the data and allow for the selection of the NCQE sample. The following quantities comprise the BONSAI output, the first two being help-

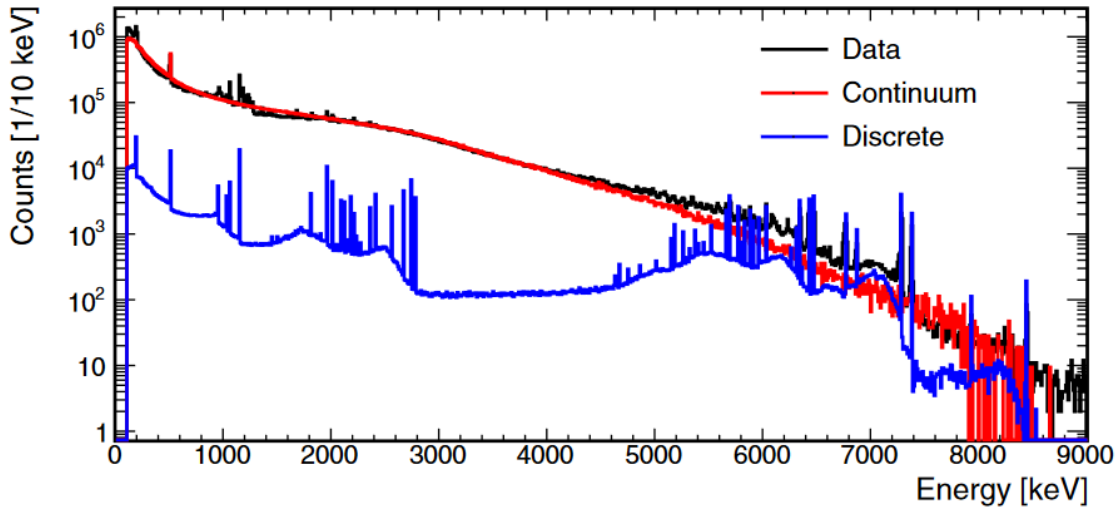


Figure 6.7: Energy spectra for the ANNRI-Gd model broken down into its continuous and discrete components along with data from the ANNRI-Gd experiment [40].

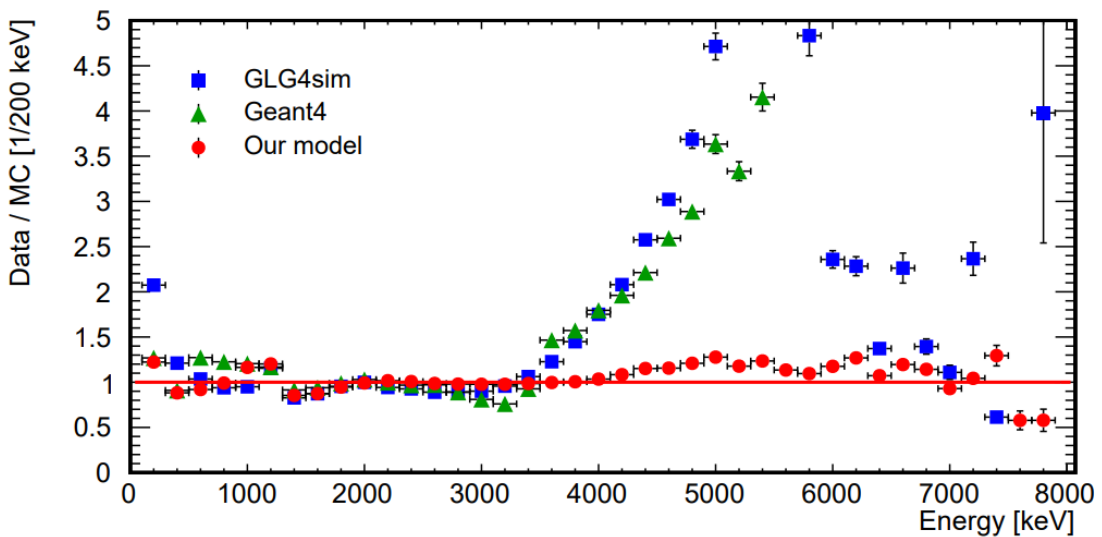


Figure 6.8: Comparison between neutron capture MC models and ANNRI-Gd data, with the ratio of data and MC on the y-axis, the GLG4sim model in blue, Geant4 default model in green and the ANNRI-Gd model in red [40].

ful spectator variables and the latter five constituting parameters which are used in the reduction phase of the analysis, from which the neutrino NCQE sample is determined.

#### 1. Neutrino vertex position

The reconstructed location of the neutrino interaction event.

#### 2. Neutrino vertex direction

This vector points towards the direction which is an average over all the Cherenkov cone axes which are produced, due to there being multiple leptons induced in the interaction.

#### 3. Reconstructed energy

In line with the standard SK low energy analysis definition, this energy is simply the reconstructed kinetic energy of the electrons.

#### 4. Dwall

This variable gives the minimum distance of the neutrino vertex position from the closest wall of the Super-Kamiokande detector.

#### 5. Effwall

This variable gives the distance between the neutrino vertex position and the closest wall, but moving back from the vertex position along the neutrino vertex direction vector.

#### 6. Vertex direction and goodness coefficient

The coefficient  $ovaQ$  (defined in Equation 6.3) describes the quality of the vertex reconstruction. It consists of two parameters  $g_{vtx}^2$  and  $g_{dir}^2$  where the former describes the goodness of the vertex which is based on PMT hit timings, and increases the sharper an event is in time. The latter is the directional goodness and measures the azimuthal uniformity in the ring pattern produced by the Cherenkov cone, which decreases the more uniform an event is in space. As a result of this,  $ovaQ$  increases the more uniform and sharp in time an event is.

$$ova\ Q = g_{vtx}^2 - g_{dir}^2 \quad (6.3)$$

$g_{vtx}$  is calculated using a fit of the PMT timing distribution and using the hit times of the PMT it is defined as in Equation 6.4.

$$g_{vtx} = \frac{\sum_i w_i e^{-\frac{1}{2}(\frac{\Delta t_i}{\sigma})^2}}{\sum_i w_i} \text{ with } w_i = -\frac{1}{2}(\frac{\Delta t_i}{\omega})^2 \quad (6.4)$$

Here  $\sum_i w_i$  is the weight given to the i-th hit PMT for the reduction of dark noise,

where  $\omega$  has a value of 60ns.  $\sigma$  has a value of 5ns which is used to test the goodness, and as a result, a sharp timing distribution produces a large vertex goodness.  $g_{dir}$  is calculated by looking at how spatially uniform the PMT hits are in the azimuthal angle around the reconstructed neutrino vertex direction. The hits are ordered from 0 to  $2\pi$  and compared to a uniform distribution of angles. Equation 6.5 shows how the minimum difference between the uniform distribution and the data is subtracted from the maximum difference and normalized to produce  $g_{dir}$ .

$$g_{dir} = \frac{\max_i\{\angle_{uni}(i) - \angle_{data}(i)\} - \min_i\{\angle_{uni}(i) - \angle_{data}(i)\}}{2\pi} \quad (6.5)$$

where  $\angle_{data}(i)$  is the azimuthal angle of i-th hit real PMT included in the number of hits in 50ns.  $\angle_{uni}(i) = 2\pi i/N_{50}$  is the azimuthal angle of the i-th virtual PMT hit, but only when uniform distribution of the hits is assumed. As the uniformity of the hit pattern increases, the goodness decreases.

## 7. Cherenkov angle $\theta_C$

In order to estimate the Cherenkov opening angle, all the possible combinations of PMT hits of three hit PMTs in a 15 nanosecond timing window are binned. A histogram is produced of these binned angles and divided into 100 bins, and by looking at the seven neighbouring bins with the largest number of entries, peaks in the histogram are located. The middle of the seven bins is chosen to be the Cherenkov angle of the event. Figure 6.9 shows the vertex of the prompt event and three PMT hit vectors which produce the Cherenkov opening angle.

For relativistic electrons in water, the value of the Cherenkov opening angle is  $\approx 42^\circ$ , due to the relation:

$$\cos \theta_{\text{Cherenkov}} = \frac{1}{n\beta} \quad (6.6)$$

where  $\beta = v/c \approx 1$  and  $n$  is the refractive index of water, 1.33. However due to other particles in the simulation, such as protons or muons, the Cherenkov cone is expected to be narrower, or if multiple leptons are present, the Cherenkov cones will be less distinct and more spread out, leading to deviations from the  $42^\circ$  value.

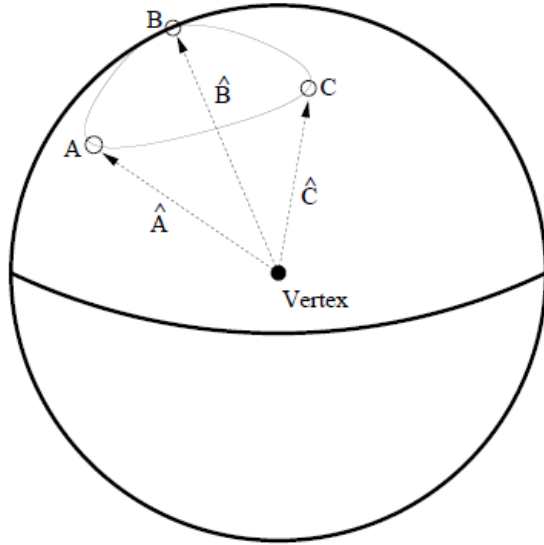


Figure 6.9: Schematic of the prompt event vertex and a triplet of independent PMT hits which make up the Cherenkov angle, taken from [42].

### 6.2.2 Comparison of BONSAI reconstruction output variables between SKDETSIM versions

The BONSAI reconstruction output variables were compared between three versions of SKDETSIM, the version used in the previous NCQE neutron capture on hydrogen only analysis, with no neutron capture on Gd implemented (black), the SKDETSIM-SKGd photon-evaporation model mentioned in the previous section (red), and the SKDETSIM SK-Gd ANNRI-Gd model (green). Figure 6.10 to Figure 6.14 shows the comparison of these models for the output BONSAI variables  $E_{rec}$ , dwall, effwall, ovaQ, and  $\theta_C$ , where the y-axis shows the number of events.

To ensure correct implementation of the ANNRI-Gd model, ensuring the BONSAI output variables were similar between these SKDETSIM versions was important as the Gadolinium model should only effect the neutron capture in the simulation, not the output from event reconstruction of the neutrino interaction vertex. As can be seen in the SKDETSIM/SKDETSIM-SKGd BONSAI reconstruction variable comparison plots, this holds true for  $E_{rec}$ , dwall, effwall and  $\theta_C$ , but not for the vertex and goodness coefficient ovaQ, where the ANNRI-Gd model differs for ovaQ between -0.05 and 0.15 compared to the SKDETSIM and SKDETSIM photon-evaporation model. To investigate this difference

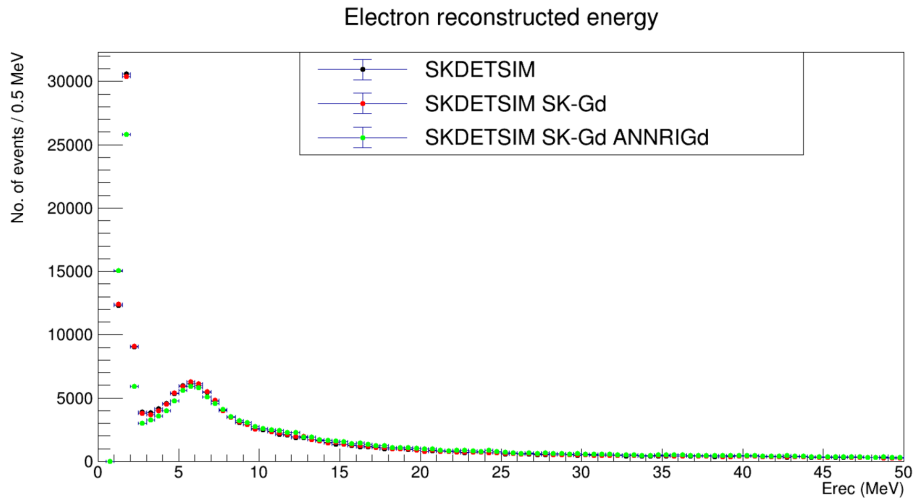


Figure 6.10: Comparisons of prompt event electron reconstructed energy between versions of SKDETSIM

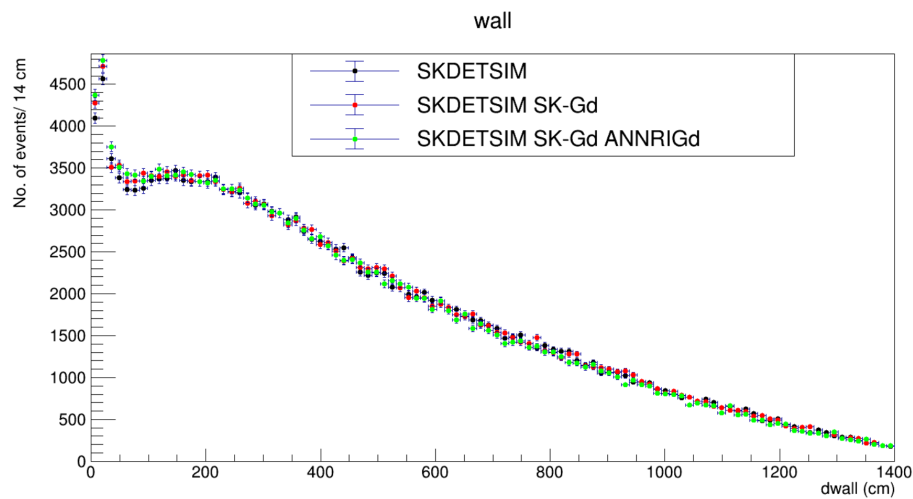


Figure 6.11: Comparisons of dwall for the prompt event between versions of SKDETSIM

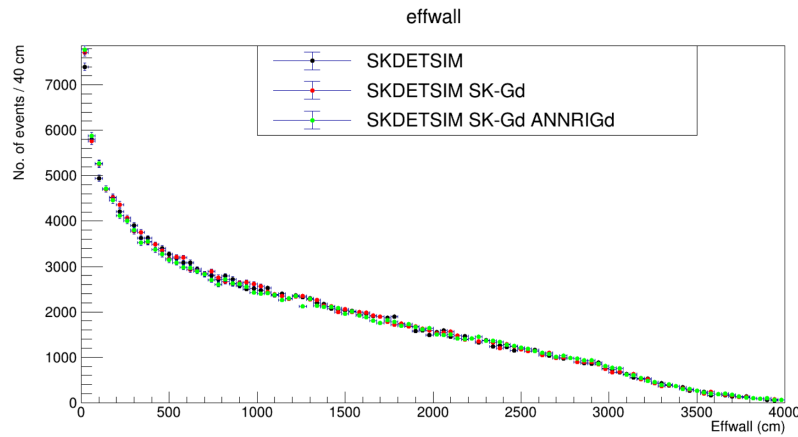


Figure 6.12: Comparisons of effwall for the prompt event between versions of SKDETSIM

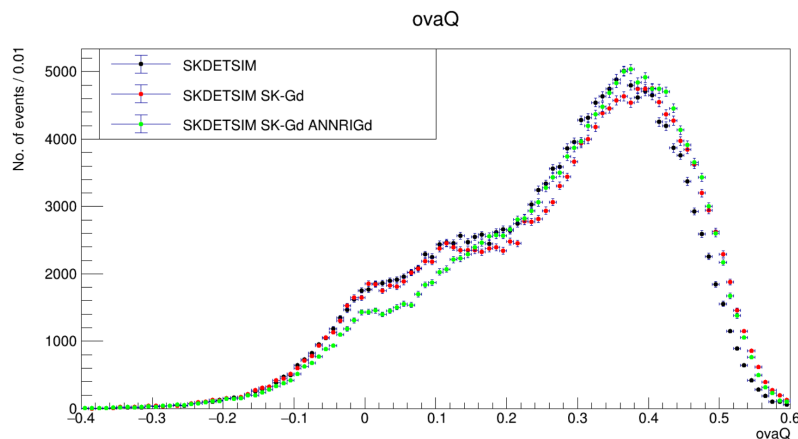


Figure 6.13: Comparisons of ovaQ for the prompt event between versions of SKDETSIM

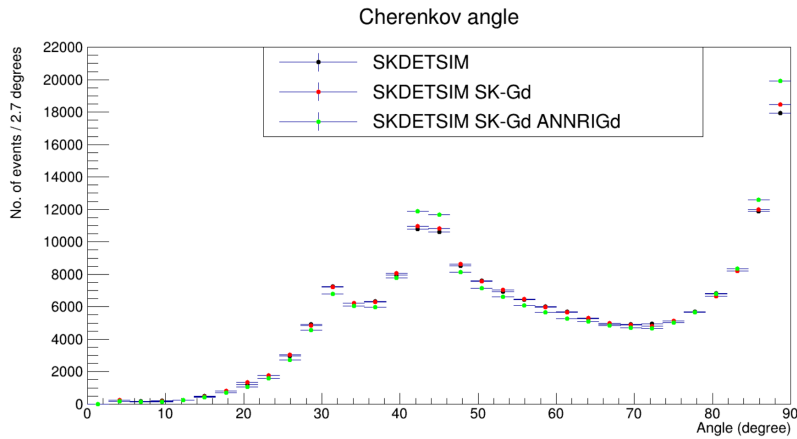


Figure 6.14: Comparisons of Cherenkov angle for the prompt event between versions of SKDETSIM

SKDETSIM version	Value (cm)
SKDETSIM-V	113.2
SKDETSIM-SKGd (Photon evaporation model)	109.4
SKDETSIM-SKGd (ANNRI-Gd model)	111.9

Table 6.5: Value of the true neutrino vertex - reconstructed neutrino vertex distribution which encompasses 1-sigma (68%) of the number of events.

further, distributions of the vertex goodness and the directional goodness which make up ovaQ (according to Equation 6.3) were also checked, shown in Figure 6.13.

The vertex goodness (gvtx) and directional goodness (gdir) squared comparisons are shown in Figures 6.15 and 6.16 respectively. Figure 6.15 shows a slight discrepancy between the SKDETSIM versions, but not enough to warrant further investigation. In addition to checking the previous BONSAI reduction phase quantities, the distance between the true neutrino vertex from the simulation and the neutrino vertex from the BONSAI reconstruction was also checked for the different SKDETSIM versions, shown in Figure 6.17. Table 6.5 shows the value of this distribution which encompasses 1-sigma (68%) of the number of events: this value was very similar for all SKDETSIM versions.

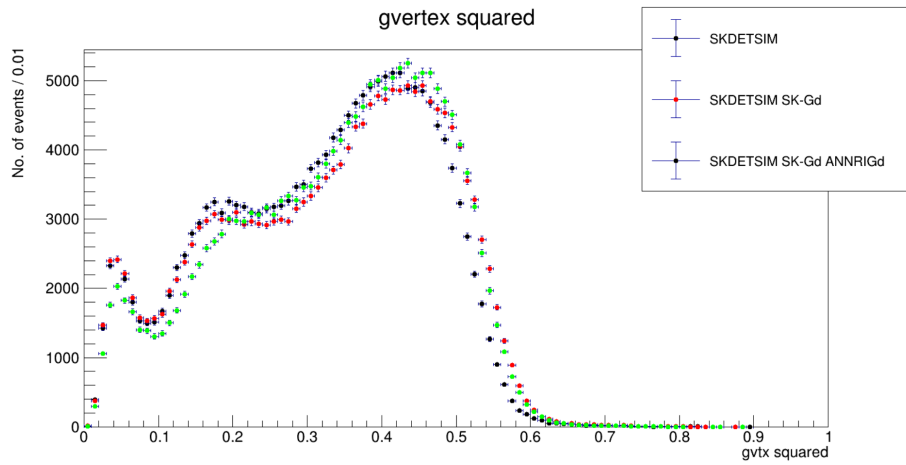


Figure 6.15: Comparisons of vertex goodness for the prompt event between versions of SKDETSIM

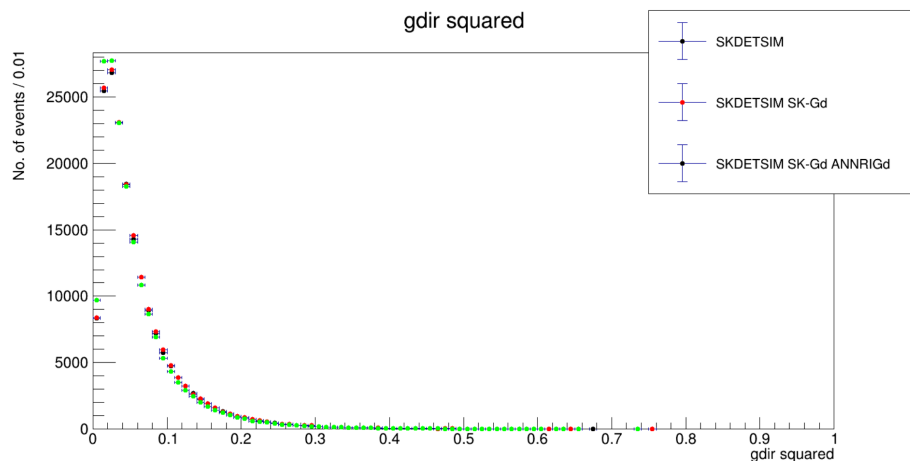


Figure 6.16: Comparisons of directional goodness for the prompt event between versions of SKDETSIM

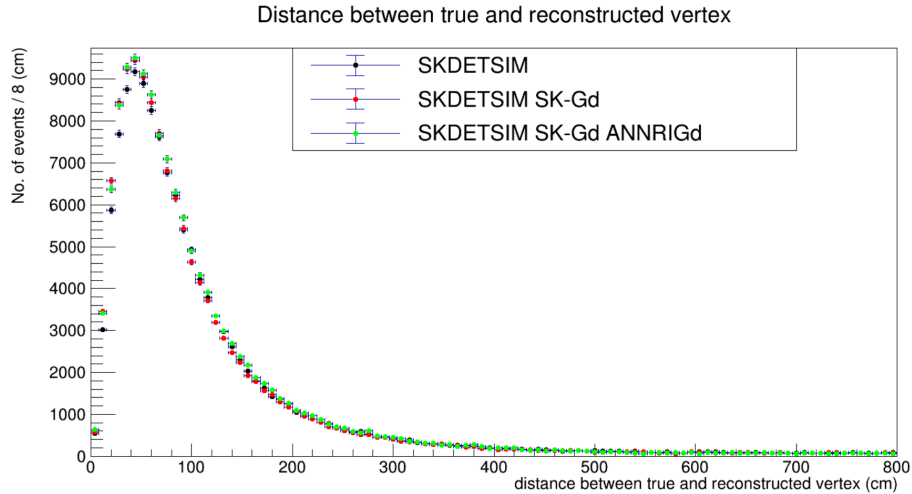


Figure 6.17: Distance between true and reconstructed neutrino vertex for different SKDETSIM versions

### Comparisons of event reconstruction output between NTag versions

To ensure that the NCQE event selection and neutron tagging could be carried out using the new NTag code, comparisons of the output BONSAI reconstruction variables between the two versions were made to ensure the validity of the reconstruction output. Figures 6.18, 6.19, 6.20, 6.21 and 6.22 shows the reconstructed energy, dwall, effwall, Cherenkov angle and ovaQ parameters, with the legacy NTag output in black and the new NTag output in red.

From the comparisons of the event reconstruction variables we can conclude that there is no significant variation between the way the different gadolinium implementation models in the detector simulation doesn't affect the way the prompt event is reconstructed. This makes sense as the only difference the neutron capture model should make should relate to the secondary interactions - checking the prompt event distributions remain unchanged is a confirmation of this. Similarly, the comparisons between the two NTag versions, legacy and new show that the change in the neutron tagging algorithm didn't affect the prompt event reconstruction either.

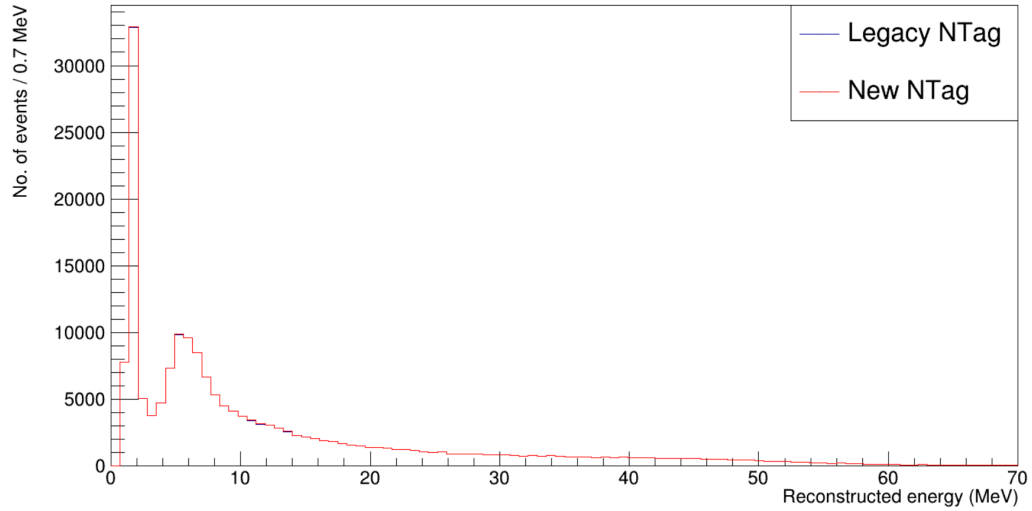


Figure 6.18: Reconstructed energy (MeV) comparison

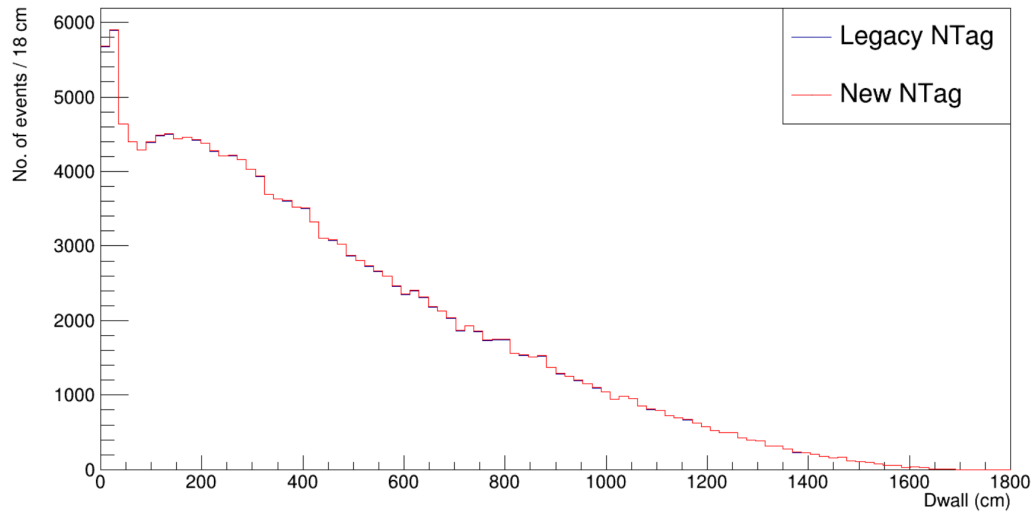


Figure 6.19: DWall (cm) comparison

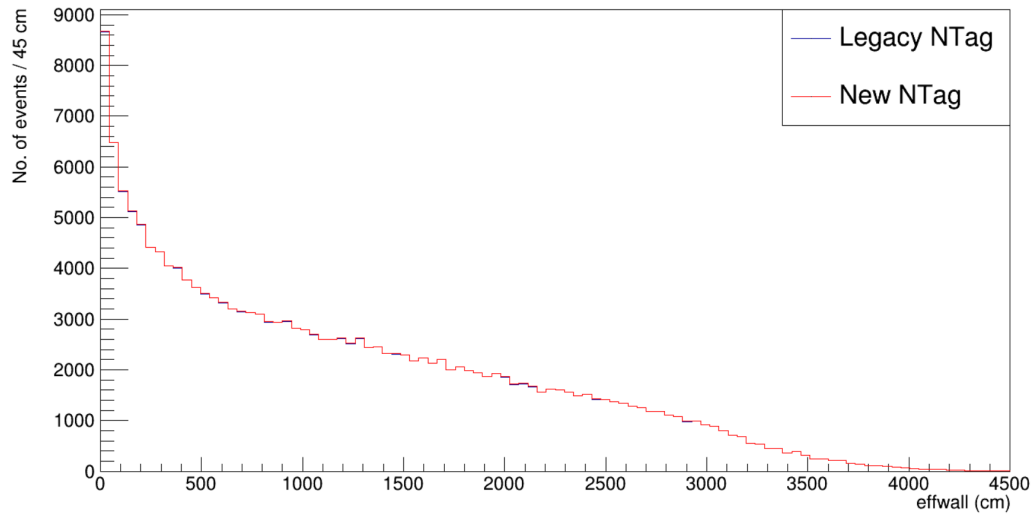


Figure 6.20: Effwall (cm) comparison

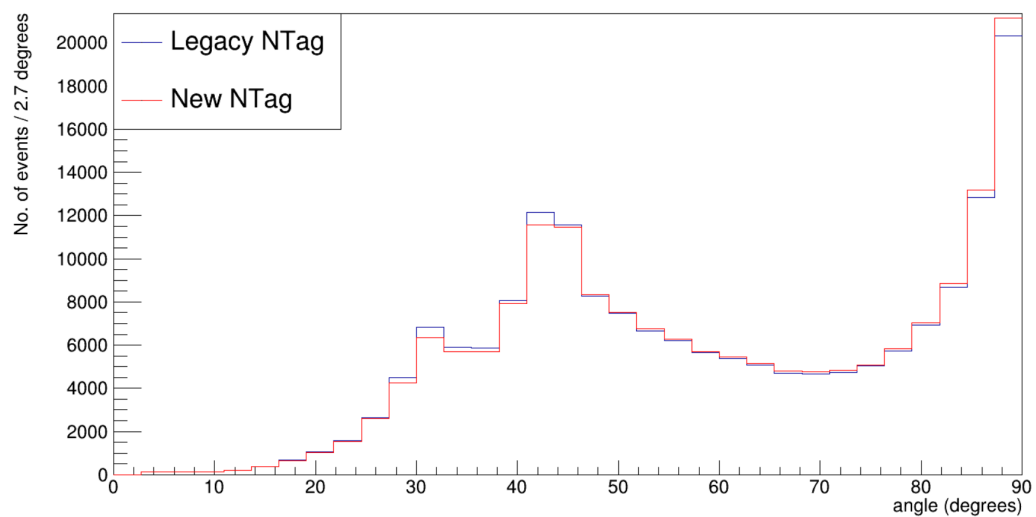


Figure 6.21: Reconstructed Cherenkov angle (degrees)

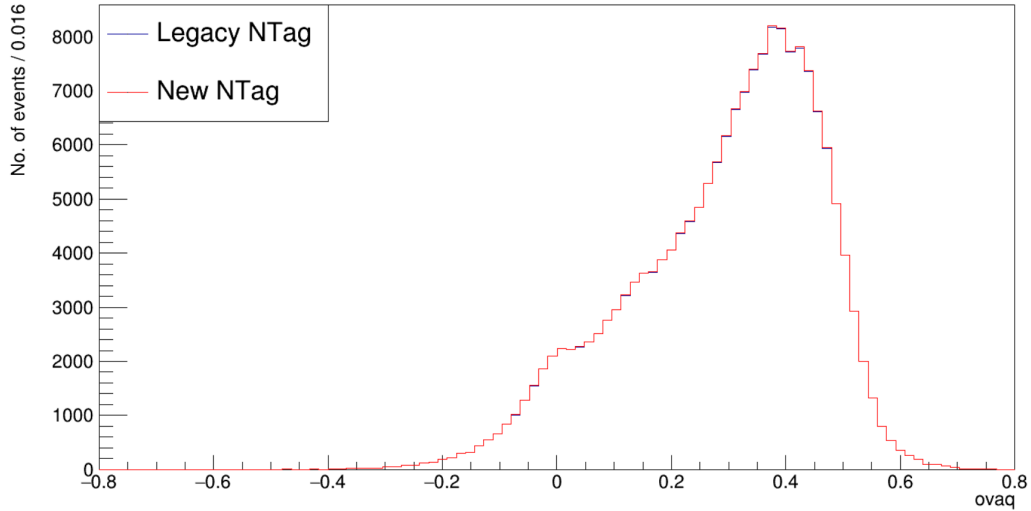


Figure 6.22: Comparisons of vertex goodness for the prompt event between versions of SKDETSIM

### 6.2.3 NCQE event selection

Prior to applying the neutron tagging algorithm which searches for neutron candidates, events which satisfy the neutral current quasi-elastic criteria need to be selected. This selection only involves the neutrino vertex information, no information about the neutron candidates is used in the NCQE selection process.

The following cuts are applied to the Monte Carlo, in order to select the NCQE events. These include a visible energy cut, a fiducial volume cut, a low energy background cut, and a cut to exclude charged current interaction events (CCQE).

#### Visible energy cut

The range for  $E_{rec}$  in this variable is 3.49 MeV to 29.49 MeV - the estimated kinetic energy under the hypothesis that the event is a singular electron. The upper value for this range is chosen because the background of Michel electrons from muon neutrino and muon anti-neutrino charged current interactions increase but the NCQE signal decreases above 30 MeV. This is shown in Figure 6.23, where the NC elastic (and therefore NCQE) signal decreases significantly above 30 MeV but the decay-e events and electron neutrino charged current events increase.

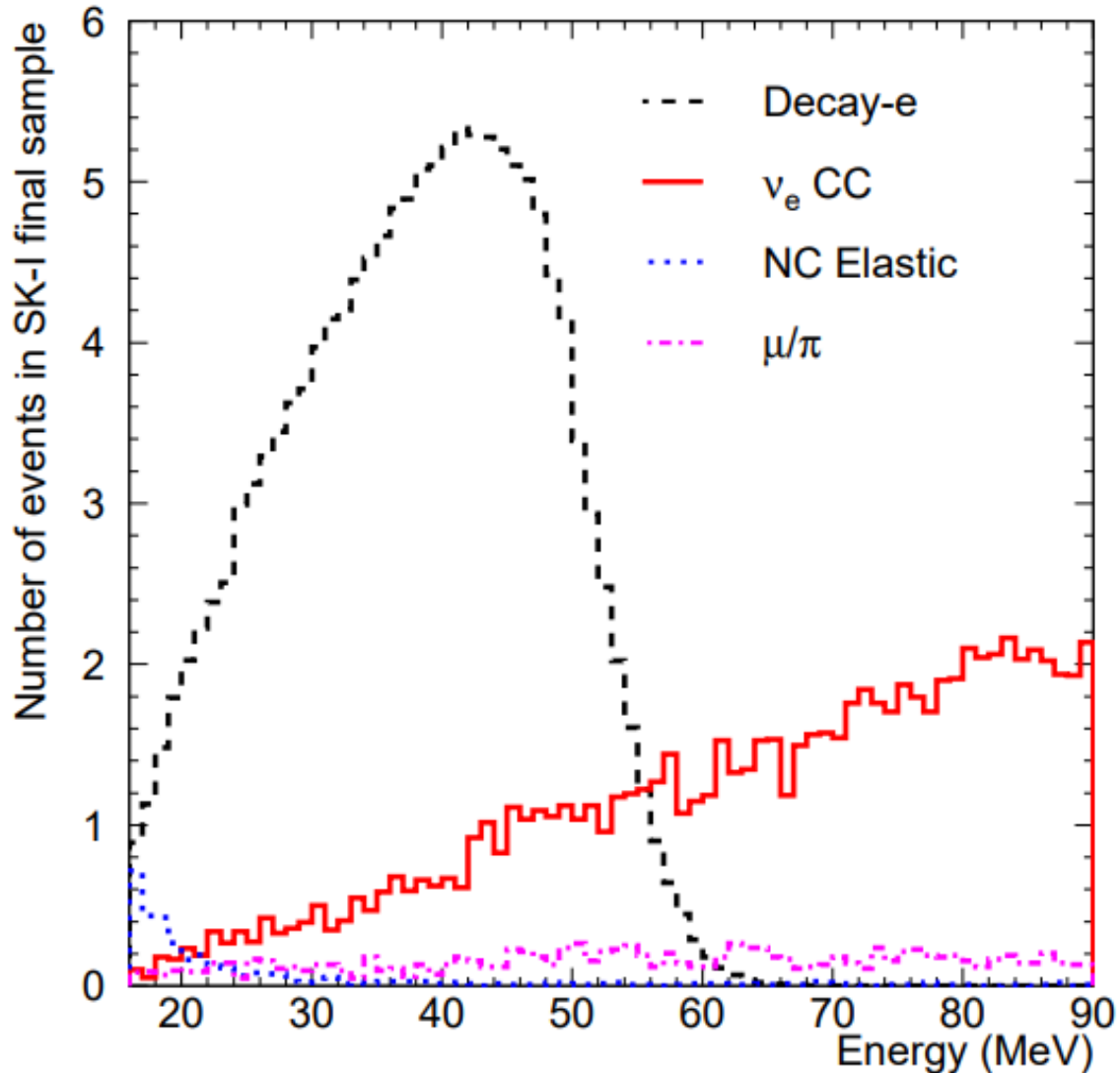


Figure 6.23: Spectra of NCQE backgrounds where the  $\nu_\mu$  charged current channel is from decay electron data, whereas the other three are from Monte Carlo. A clear decrease of NC elastic events are shown after 30 MeV. Taken from [43].

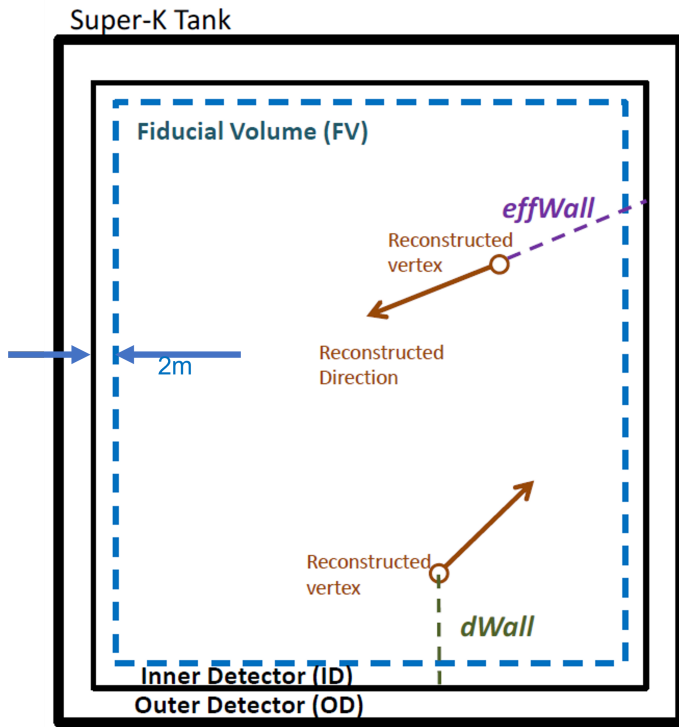


Figure 6.24: Schematic defining the fiducial volume (FV) and the dWall and effWall variables.

### Radioactivity background cut

Due to radioactive impurities inside the detector material, specifically the wall of the inner detector, there is a cut involving the distance from the detector wall to the prompt interaction vertex - this is the fiducial volume (FV) cut. Events where the distance between the prompt interaction vertex and the detector wall is less than 200 cm are removed.

There are two more cuts used and these involve the distance to the inner detector wall. The variable **dWall** is defined as the distance from the reconstructed event vertex to the nearest inner detector wall inside the FV, and is set to **dWall** needing to be less than 200 cm. A similar cut is also used where events where the distance between the prompt interaction vertex and the distance to the inner detector wall in the neutrino vertex vector direction (**effWall**) is less than 200 cm is removed. Figure 6.24 shows an illustration of how the variables FV, **dWall** and **effWall** are defined.

These are standard cuts applied in all Super-Kamiokande analyses in order to avoid backgrounds, and when you have events where the energy region is below 6 MeV even

more stringent cuts are required to further reduce background from the inner detector wall, described in the next Subsection.

### Low energy background cut

The variables dwall, effwall and ovaQ are used to tune cuts in the energy region below 6 MeV. There are five energy regions with a width of 0.5 MeV used between the lower end of the visible energy cut region (3.49 MeV) and 5.99 MeV where the cuts on the dwall, effwall and ovaQ variables are optimised. Cuts are applied on the dwall, effwall and ovaQ variables and an event is only accepted if the values of dwall, effwall and ovaQ are greater than the threshold cut values. In each 0.5 MeV energy interval, these threshold values are optimised based on the T2K run period due to the beam power and detector conditions being different from run to run, especially since the Gadolinium loading occurred in the detector. Equation 6.7 shows how the figure-of-merit (FOM) value is to be maximised for the optimisation of each cut.

$$\text{FOM} = \frac{N_{\text{sig}}}{\sqrt{N_{\text{sig}} + N_{\text{bkg}}}} \quad \left( N_{\text{bkg}} = N_{\text{bkg}}^{\text{MC}} + N_{\text{bkg}}^{\text{beam-unrelated}} \right) \quad (6.7)$$

Here  $N_{\text{sig}}$  is the number of NCQE neutrino events in the FHC Monte Carlo sample and  $N_{\text{bkg}}$  is the summation of the background events, and the FOM is calculated separately in the five energy intervals, and the optimised cut value is taken as the one which maximises the FOM. Then the optimised cut values in each energy interval are fitted with a linear function dependent on the visible energy variables ( $E_{\text{rec}}$ ). Equation 6.10 gives the relation of  $E_{\text{rec}}$  to the optimised cut values for dwall, effwall and ovaQ.

$$\text{dwall}^{\text{CUT}} = p_0^{\text{dwall}} + p_1^{\text{dwall}} \times E_{\text{rec}} \quad (6.8)$$

$$\text{effwall}^{\text{CUT}} = p_0^{\text{effwall}} + p_1^{\text{effwall}} \times E_{\text{rec}} \quad (6.9)$$

$$\text{ova } Q^{\text{CUT}} = p_0^{\text{ovaQ}} + p_1^{\text{ovaQ}} \times E_{\text{rec}} \quad (6.10)$$

The scan regions and intervals for the dwall, effwall and ovaQ parameters for Equation 6.10 are given in [44].

FHC sample	MC $\#\nu_{\text{det}}$	MC $\#\nu_{\text{det}}$	fraction (%)
$\nu - NCQE$	204.1	76.6	
$\bar{\nu} - NCQE$	5.6	2.1	
$NC - \text{other}$	47.8	17.9	
$CC$	8.8	3.3	
Total	266.3	100	

Table 6.6: FHC MC expectation values for each interaction type

#### 6.2.4 Charged current event (CC) interaction cut

In order to reduce the number of charged-current events which may be mistakenly included in the NCQE selection, a cut regarding the reconstructed Cherenkov angle of the prompt event is also utilised alongside the low energy background cut, where the accepted Cherenkov angle of a prompt event ( $\theta_C$ ) should be greater than the threshold cut value  $\theta_C^{CUT}$  where the cut value is determined by the linear equation dependent on  $E_{\text{rec}}$  as shown in Equation 6.11.

$$\theta_C^{CUT} = p_0^{\theta_C} + p_1^{\theta_C} \times E_{\text{rec}} \quad (6.11)$$

Just like for the low energy background cut values, the values of the optimised parameters in Equation 6.11 are given in [44] and are shown in Figure 6.25.

#### 6.2.5 Prompt event NCQE reduction cut plots

Before applying the NTag algorithm, either legacy or new, plots were produced of the number of neutrino events and their dependence the reduction cut variables mentioned previously. These are shown in Figures 6.26 to 6.30. Each figure shows the corresponding plot for the previous NCQE analysis carried out with neutron tagging on Hydrogen on the left, with the plot from this analysis on the right. Due to the FHC sample not purely consisting of neutrino and antineutrino NCQE interactions, Table 6.6 gives the expected number of neutrino events for each type of interaction including neutral current and charged current interactions.

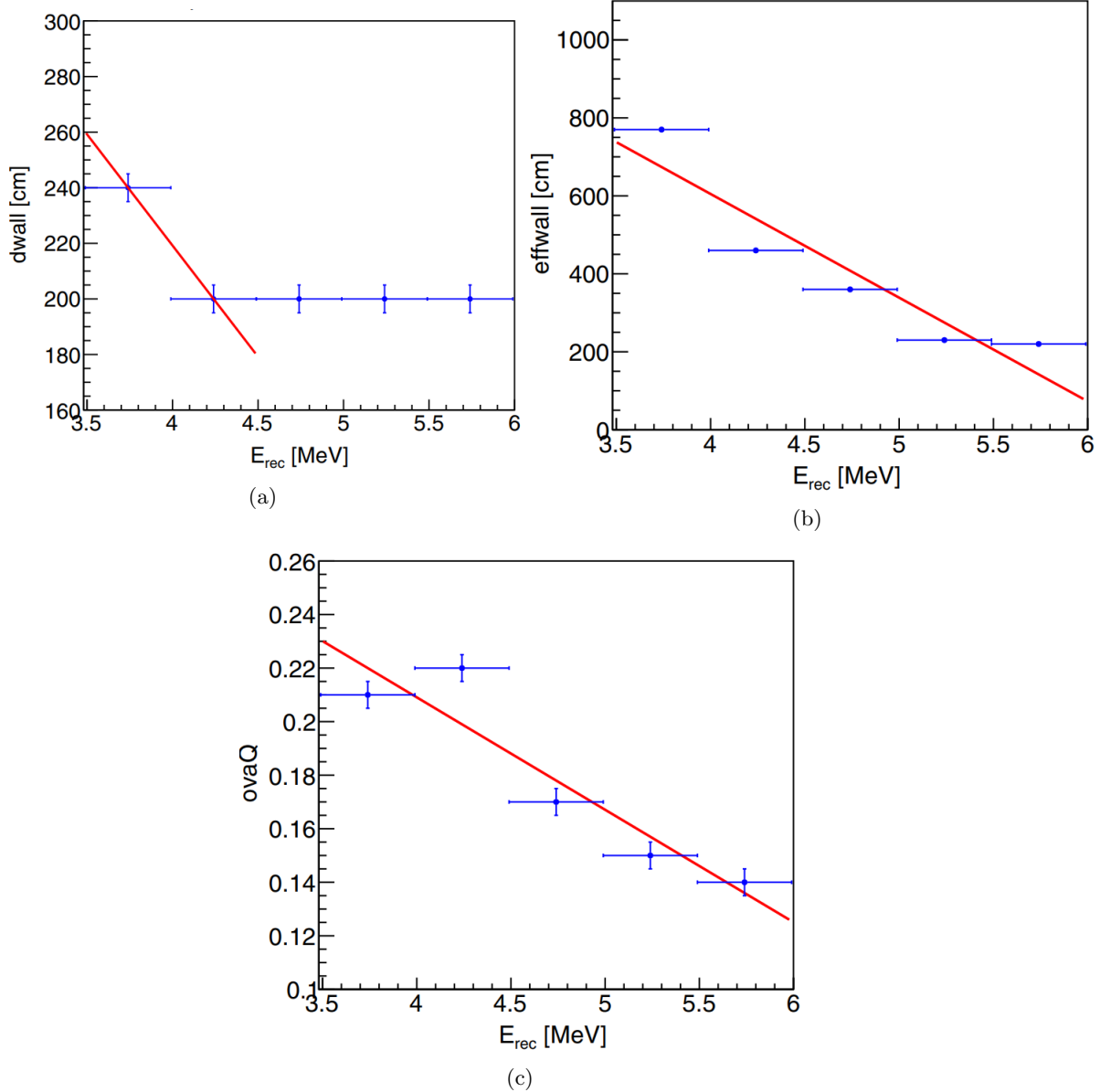


Figure 6.25: Optimised cut values for  $d_{\text{wall}}$  (top),  $e_{\text{ff}}_{\text{wall}}$  (bottom left) and  $\text{ovaQ}$  (bottom right) for Run 8 FHC mode. The red lines are linear fits to the values for these distributions, where events which have values above the lines are used in the analysis. [44].

Figure 6.26: Comparisons of stacked histograms for the  $E_{rec}$  variable between NCQE neutron tag on H analysis (left) and this analysis (right)

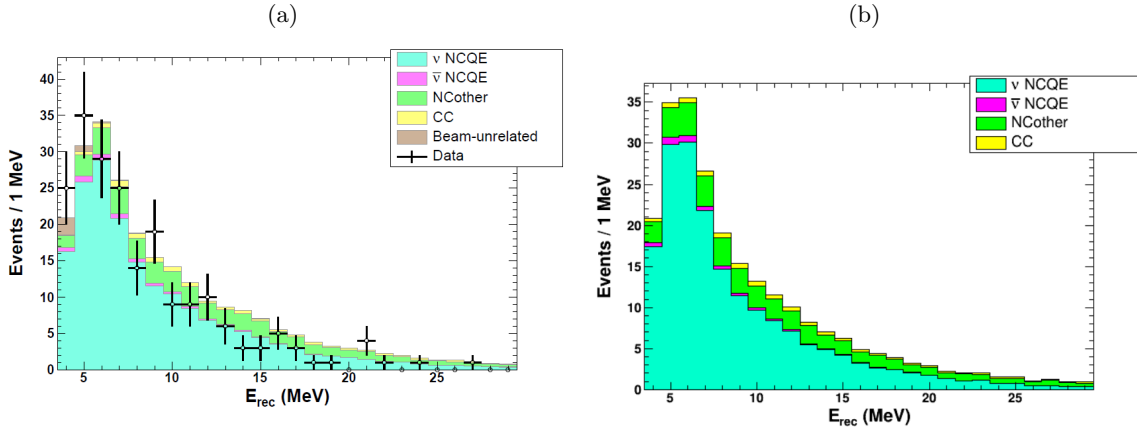


Figure 6.27: Comparisons of stacked histograms for the Dwall variable between NCQE neutron tag on H analysis (left) and this analysis (right)

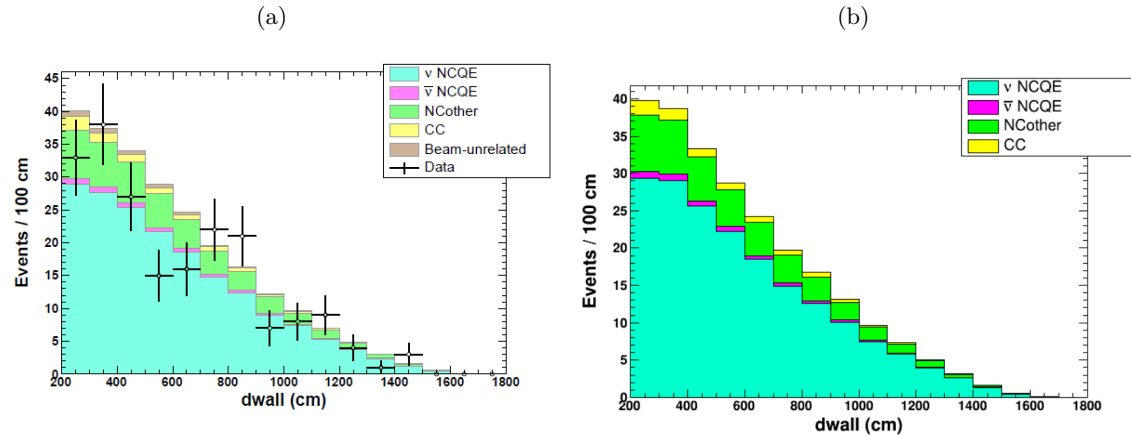


Figure 6.28: Comparisons of stacked histograms for the Effwall variable between NCQE neutron tag on H analysis (left) and this analysis (right)

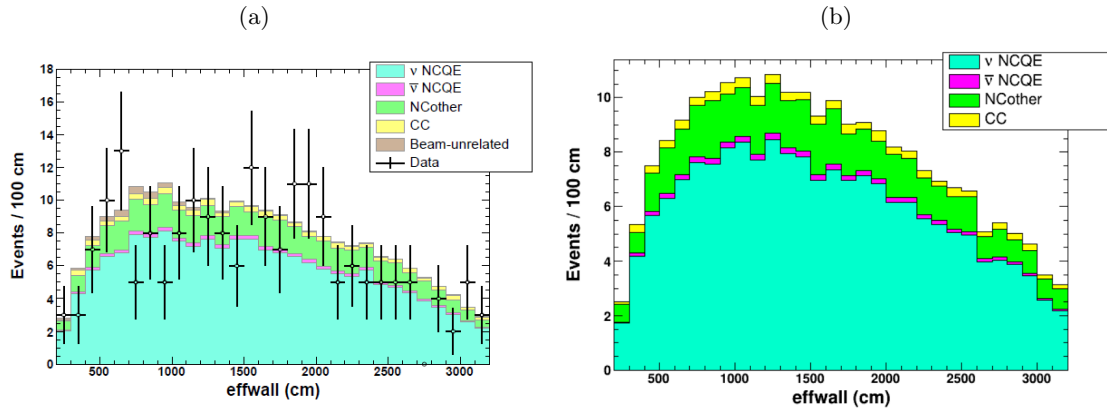


Figure 6.29: Comparisons of stacked histograms for the ovaQ variable between NCQE neutron tag on H analysis (left) and this analysis (right)

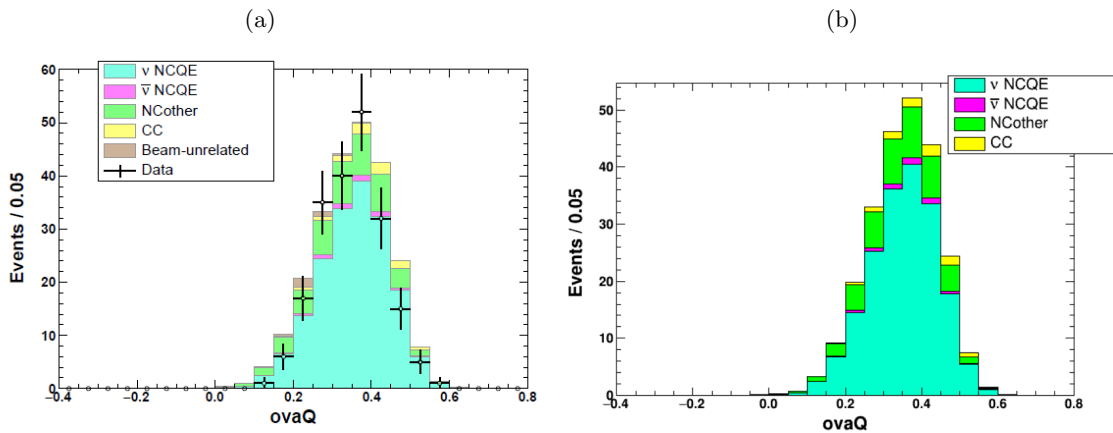
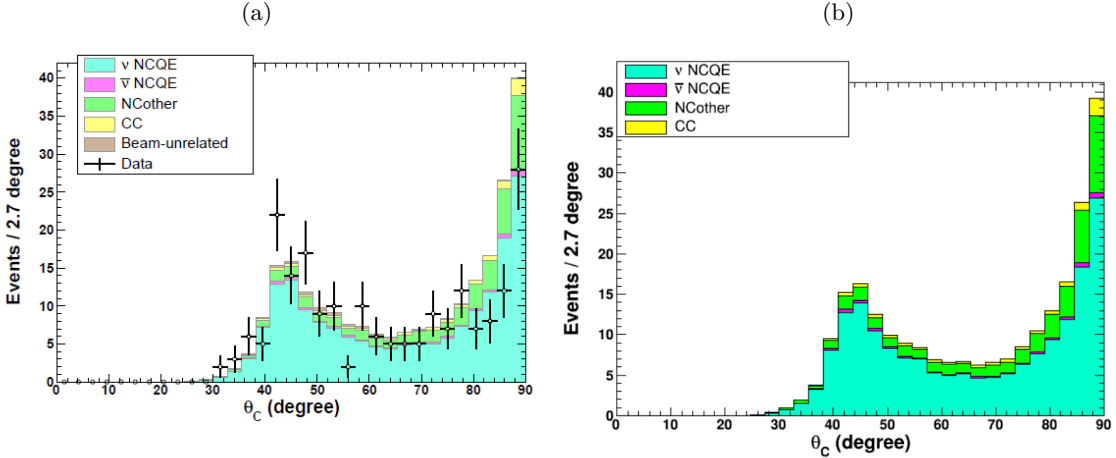


Figure 6.30: Comparisons of stacked histograms for the  $\theta_C$  variable between NCQE neutron tag on H analysis (left) and this analysis (right)



### 6.3 Secondary selection

As mentioned previously, two neutron tagging algorithms were used in this analysis, the legacy NTag code, used in previous NCQE analyses and modified to work with a version of SKDETSIM which has Gadolinium included and new NTag code which uses a slightly different neutron tagging algorithm specifically with regards to the primary and secondary selection criteria which will be discussed in later subsections.

#### 6.3.1 True neutron tagging information

Prior to defining the primary and secondary selection criteria for each neutron tagging algorithm, it is important to produce some distributions of basic variables regarding the neutron capture that occur in the simulation, such as neutron capture time, position and number. Figure 6.31 shows the distribution for the number of neutron captures and the true capture time of the neutrons for both the legacy (green) and new (red) NTag code.

In order to classify the neutron captures on hydrogen and gadolinium separately, the energy of the gammas produced from the neutron capture were used, along with the number of gammas produced from the neutron capture. If the energy of the gamma produced is 2.22 MeV and only one gamma ray was produced from the neutron capture, the neutron capture was classified as a capture on a proton. If there are multiple gamma rays produced and if the energy of the gamma cascade is 8.5 MeV in total it is classified as a neutron

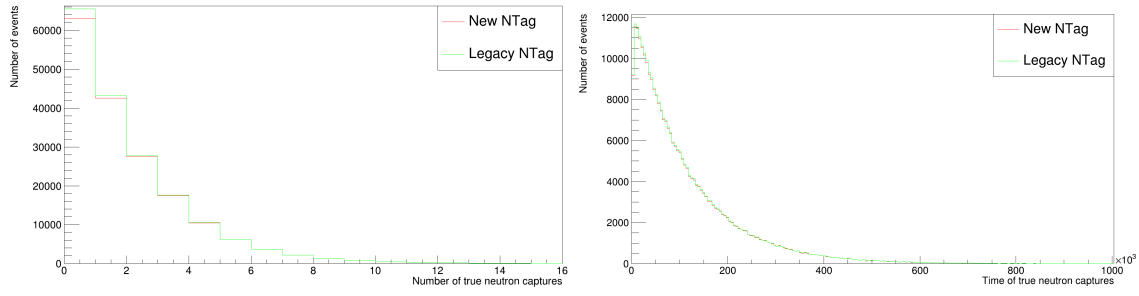


Figure 6.31: Number of events plotted against number of true neutron captures (left) and number of events plotted against the time of all neutron captures ( $\mu\text{s}$ ) (right).

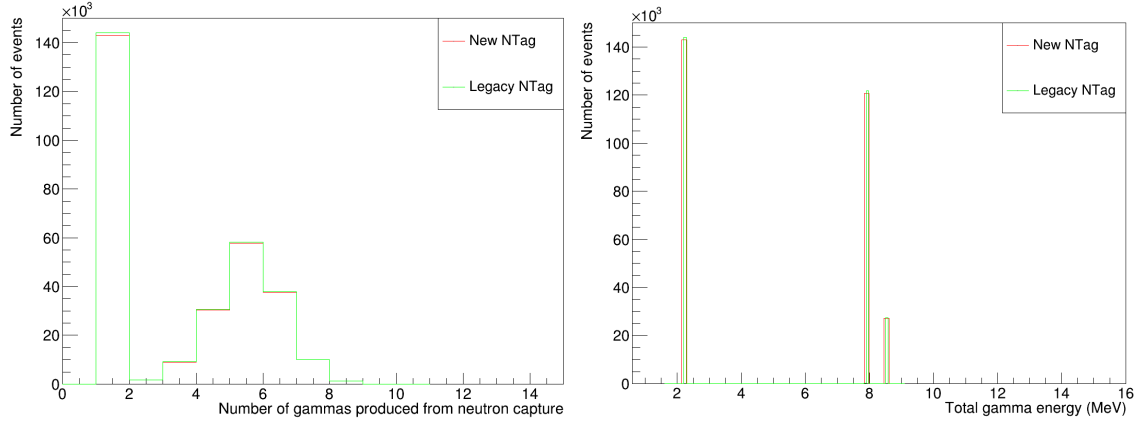


Figure 6.32: Number of gamma rays produced by neutron capture (left) and total energy of gamma rays produced by neutron capture (right) in the Monte Carlo

capture on  $^{155}\text{Gd}$  and if the energy of the gamma cascade is 7.9 MeV, it is classified as a neutron capture on  $^{157}\text{Gd}$ . Distributions of the number of gammas produced from neutron capture in the simulation, and also the energy of these gammas were plotted, shown for both the legacy (green) and new (red) NTag code, shown in Figure 6.32.

Figure 6.32 shows that both NTag algorithms have the same number of gammas produced by neutron capture on hydrogen (shown by the peak at 2.22 MeV), and the same number of gammas for the gamma cascade produced by neutron capture on the  $^{155}\text{Gd}$  and  $^{157}\text{Gd}$  isotopes of Gadolinium, where the modal number of gammas in the cascade for both NTag code is five. In addition to checking the number and energy of the gammas, and the number and time of true neutron captures, the neutron capture positions for the x,y and z directions were also plotted as shown in 6.33.

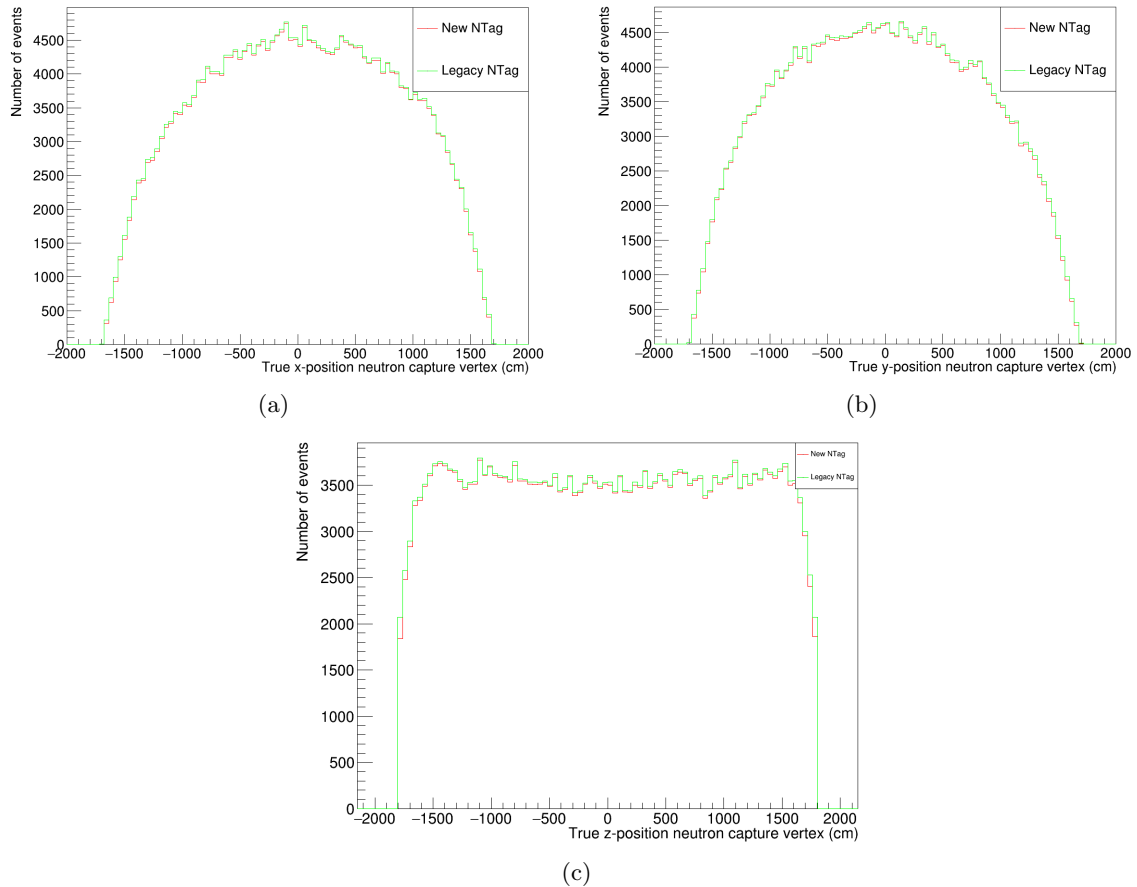


Figure 6.33: True neutron capture x-position (cm) (top left), true neutron capture y-position (cm) (top right) and true neutron capture z-position (cm)(bottom)

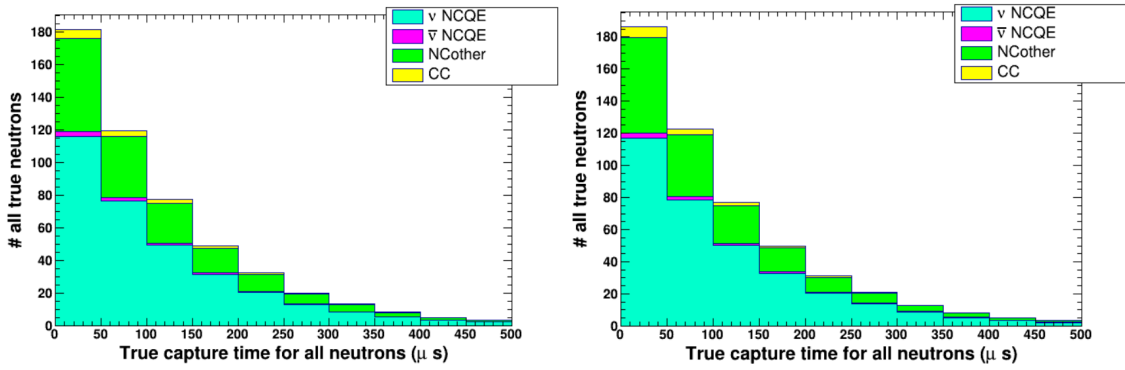


Figure 6.34: Number of true neutrons detected plotted against true neutron capture time for the legacy NTag (left) and the new NTag (right).

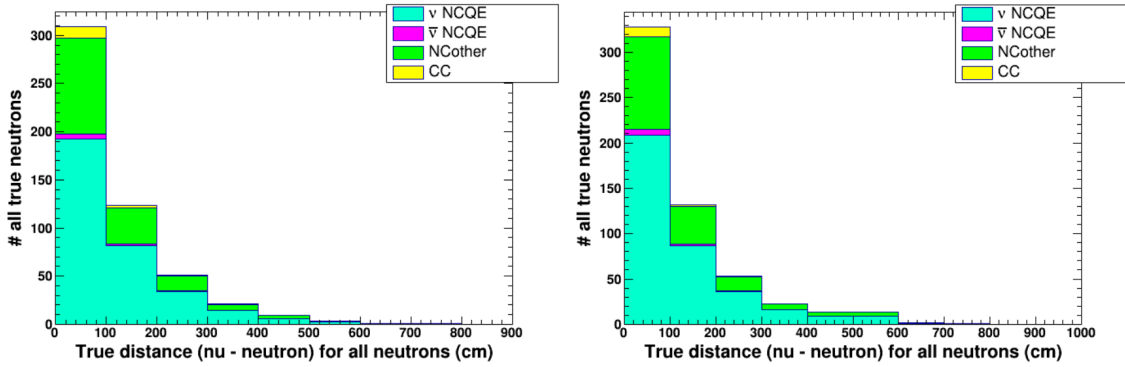


Figure 6.35: Number of true neutrons detected plotted against the distance between the neutrino and neutron capture vertices for the legacy NTag (left) and the new NTag (right).

### Truth information reduction cut plots

After ensuring that the truth neutron tagging information was the same between the legacy and new NTag versions, the next step was to produce plots with the NCQE reduction cut criteria in order to see the distribution of neutrons for certain variables which satisfy the NCQE criteria. By rewriting aspects of the new NTag code to incorporate the BONSAI variables needed for the NCQE selection, the same reduction cut criteria could be applied to the new NTag code as it was to the legacy NTag code. Figure 6.34 shows the number of true neutrons plotted against true neutron capture time for the legacy and new NTag, while Figure 6.35 shows the number of true neutrons plotted against the distance between the true neutron and neutrino capture vertices for the legacy and new NTag.

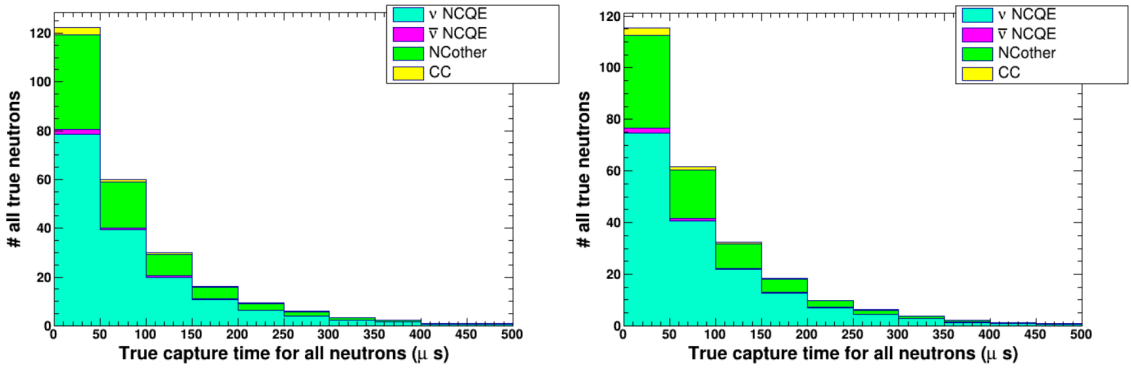


Figure 6.36: Number of true neutrons detected plotted against true neutron capture time for the new NTag, for captures on hydrogen (left) and gadolinium (right).

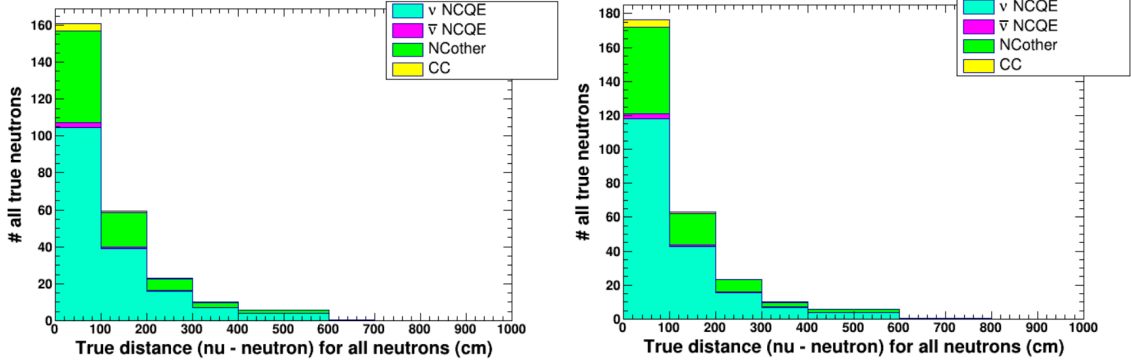


Figure 6.37: Number of true neutrons detected plotted against the distance between the neutrino and neutron capture vertices for the new NTag, for captures on hydrogen (left) and gadolinium (right)

With the level of  $\text{Gd}_2(\text{SO}_4)_3 \cdot 8\text{H}_2\text{O}$  in the simulation being 0.026%, the number of neutron captures on hydrogen and gadolinium should be approximately equal [45]. Figure 6.36 shows the the true capture time for the neutrons in the Monte Carlo seperated into captures on hydrogen and captures on gadolinium, and the distributions and the number of events look very similar, confirming this. Similarly, Figure 6.37 shows the distance between the neutrino interaction vertex and the true neutron capture vertex for captures on hydrogen and gadolinium. Once again the distributions are very similar, showing agreement with the equal number of captures.

### 6.3.2 Primary selection criteria

The rest of this Chapter focusses on analysis results from the new NTag algorithm, as this is what is currently being used by the collaboration. As input to searching for acceptable neutron candidates in the search window of 3 to 535 ns, the time of flight corrected PMT hit times is used. The reason for calculating the residual time of flight for the gamma hits is because the electrons produced from the Compton scattering of gamma rays produced by the neutron capture on hydrogen and gadolinium appear as a point-like source of Cherenkov radiation. Due to the differing optical path lengths that these photons have, there is a difference in PMT hit time. The difference in Cherenkov photon travel length before they hit different PMTs after the gamma rays from neutron capture Compton scatter off an electron needs to be taken into account via a time-of-flight (TOF) correction. Equation 6.12 gives the equation for the residual hit times  $t_i^{\text{res}}$ , where  $t_i$  is the hit time of the PMTs in the neutron search window and  $\text{TOF}_i$  is given by Equation 6.13, where  $\text{PMT}_i$  is the position vector of the hit PMT and  $\text{VTX}_\nu$  is the position vector of the reconstructed neutrino vertex and  $c_{wt}$  is the speed of light in the medium. The reason  $\text{VTX}_\nu$  is used instead of the Compton scattering vertex is because this vertex is unknown.

$$t_i^{\text{res}} = t_i - \text{TOF}_i \quad i \in \{ \text{Hit PMTs} \} \quad (6.12)$$

$$\text{TOF}_i = \frac{\left\| \overrightarrow{\text{PMT}_i} - \overrightarrow{\text{VTX}_\nu} \right\|}{c_{wt}} \quad (6.13)$$

Before the neutron candidate is passed to the secondary selection, other cuts are used to reject candidates which are not neutrons from NCQE interactions. Table 6.7 shows the three primary selection criteria. The first involves the width of the sliding window used for the neutron tagging search, which is set to 14 ns. The second is the hit tigger for the neutron candidate selection, which is set to 7 hits, which is the same for the previous NCQE Hydrogen-ntag analysis, with the maximum value of the hits set to 400. Third, the minimum time separation between the gamma hits is set to 200 ns - the reason for this is to avoid double counting the same hit from the neutron capture candidate.

One of the benefits of the addition of  $\text{Gd}_2(\text{SO}_4)_3 \cdot 8\text{H}_2\text{O}$  is that the higher visible energy improves the neutron capture vertex resolution. Figure 6.38 shows the distance between the true and reconstructed neutron capture vertices for neutron capture in water Monte Carlo (taken from [46]) on the left, and from the Monte Carlo in this analysis on the right.

Criterion	Type	New
First	Timing window width	14nsec
Second	Hit trigger and max	$7 \leq NHits \leq 400$
Third	Minimum hit separation	$\Delta t_0 \geq 200\text{nsec}$

Table 6.7: NTag primary selection criteria

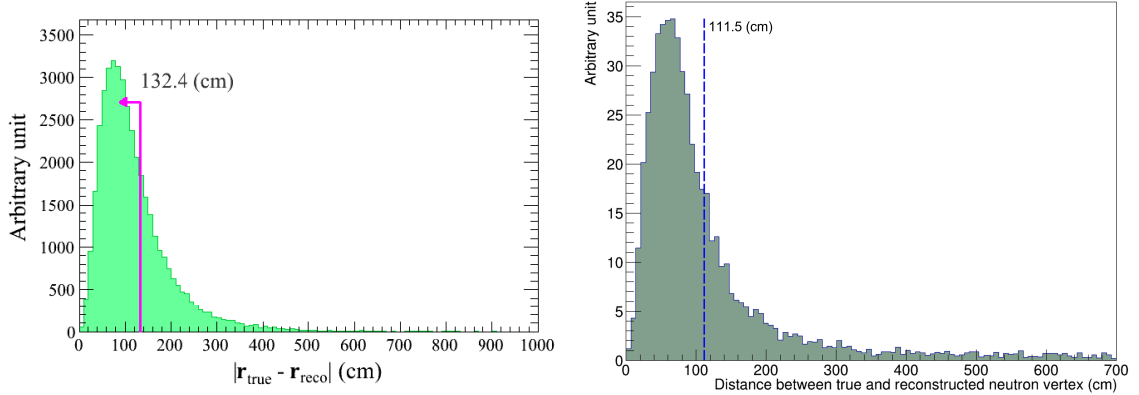


Figure 6.38: Distance between true and reconstructed neutron capture vertex in water Monte Carlo [46] (left) and from this analysis (right). The pink arrow on the left plot and the dashed blue line on the right plot shows the 68th percentile of the distributions.

It is clear that the resolution has improved, being reduced from 132.4 cm prior to the addition of gadolinium to 111.5 cm in this analysis.

### 6.3.3 Secondary selection criteria

Due to the contamination of background events still present amongst the true neutron events after primary selection, a neural network (NN) is used to efficiently remove these background events, while trying to maximise the number of true neutron events. The output of the NN is used to indicate how likely a variable is to be signal/background candidate. Each of the candidates selected during the primary selection process has an associated reconstructed Compton scattering vertex calculated for it. In order to produce residual hit times that are less spread out than TOF-corrected hits towards the neutrino vertex, the TOF-corrected hits towards the Compton scattering vertex are used instead. The aim of searching for the Compton scattering vertex is to use a method by which the

standard deviation of the residual times of the hits is minimised. Therefore the Compton scattering vertex  $n_{VTX}$  is defined as in Equation 6.14, where  $r$  is a trial vertex and  $t_i^{\text{res}}$  is the TOF-corrected hit time.

$$n_{VTX} = \underset{r}{\operatorname{argmin}} \sqrt{\frac{1}{NHits} \sum_{i=1}^{NHits} [t_i^{\text{res}}(\vec{r}) - \langle t^{\text{res}}(\vec{r}) \rangle]^2} \quad (6.14)$$

By considering a set of trial vertices on a cubic grid and calculating the standard deviation of the residual hit times the minimisation process is performed. After this minimization cycle, a new cycle is performed on a finer and smaller grid and carries on until a certain level of precision is reached.

When the Compton scattering vertex from neutron capture is found by this method, 12 variables which describe different aspects of the neutron candidate are calculated, using NTag. For each of the neutron candidates the vector of these variables are computed and fed into the neural network and this produces an output value which is between 0 and 1. These variables relate to different features regarding categorising hits from neutron capture on Gd or H, including the number of the hits from neutron capture, the isotropy of these hits, the Cherenkov angles of these hits and the position of the neutron vertex in the detector when capture occurs. The purpose of these variables is to tag the neutrons and better separate tagged neutrons from accidentals and to distinguish when a capture occurs on hydrogen or gadolinium. A description of these variables are given below.

#### NTag variables

The following twelve variables are fed into the TMVA neural network model for the secondary selection, and the TMVA reader and the input variables to get the classifier output:

#### NHits

This is defined as the number of hits in a sliding timing window for the neutron candidate, however instead of this being set to a value of 10 nsec as it was for the neutron capture on hydrogen NCQE analyses, this was increased to 14 nsec in order to accommodate for the increased number of hits from gamma cascades from neutron capture on gadolinium.

#### N200

This is the number of hits within -100 ns and +100 ns from the fitted time relative to the trigger. Signal events produce PMT hits which are close in time, while background events are more spread out, therefore alongside having the NHits variable, N200 is also

used to create a wider timing window around the capture time of the candidate event. This spread of background events is clearly visible for the N200 variable both in Figure 6.40 and Figure 6.41: the distributions associated with neutron captures on hydrogen and gadolinium (red and green lines respectively) have distinct peaks, while the background events (magenta) have a more diffuse distribution.

#### N1300

This is the number of PMT hits in a 1300 ns timing window, specifically between -520 ns and +780 ns from the fitted time relative to the trigger. Similarly to N200 this is a much broader timing window than NHits.

#### TRMS

This calculates the standard deviation of the time-of-flight corrected PMT hit times from NHits. The spread of hit times varies between signal and background events, due to background events having a larger residual time spread than signal events: this is shown for the TRMS plot in Figure 6.40.

#### DWall

DWall gives the difference from the fitted neutron vertex to the nearest wall in cm. This variable is used because the reconstructed vertex of background events are more likely to be near the inner detector wall, and therefore DWall can help distinguish background from signal events. As shown in Figure 6.40 and Figure 6.41, the fitted neutron vertex of the background events and signal events follow this pattern, with background events being close to the detector wall and signal events away from it.

#### DWallMeanDir

This gives the distance from the fitted neutron vertex to the wall in the direction of the mean of the PMT hits for the neutron candidate in cm. The reason this variable is used alongside DWall is that there is also the aspect of the directionality of the hits to consider. Background hits do not have directionality due to them being a product of noise hits but signal events do have directionality due to these hits being produced by Compton scattered electrons originating from gammas produced by neutron capture. This is shown in the DWallMeanDir distribution in Figure 6.40, where the background events have a larger spread than signal events.

OpeningAngleMean The next set of variables are related to the Cherenkov angle produced from a neutron candidate event: the first of these is OpeningAngleMean. This calculates the mean of all possible opening angles calculated from 3 PMT hits from the neutron captures. Signal events which have PMT hits originating from Compton scattered electrons

from 2.2 Mev gamma rays from neutron captures on hydrogen have Cherenkov opening angles which are centered around  $42^\circ$ , while neutron captures on gadolinium produce multiple gamma rays which would skew the value of OpeningAngleMean to be centered around higher values. This is reflected in Figure 6.40, where the background events have a slightly larger spread and therefore not such a strict angular dependence.

#### OpeningAngleStddev

This is the standard deviation of all possible opening angles calculated from 3 PMT hits from the neutron captures. This variable emphasises what is seen in the OpeningAngleMean distribution, where background events have a larger spread than signal events, shown in Figure 6.40 and Figure 6.41.

#### OpeningAngleSkew

This is the skewness of all possible opening angles from 3 PMT hits from the neutron captures, calculated using

$$\tilde{\mu}_3 = \frac{\sum_i^N (X_i - \bar{X})^3}{(N - 1) * \sigma^{1.5}} \quad (6.15)$$

where  $X_i$  is the hit PMT,  $\bar{X}$  is the mean of the 3-hit vector, N is the size of the vector of PMT hits, and  $\sigma$  is the standard deviation of the PMT hits. Signal events are shown to have more skewed opening angle distribution than background events, especially if they are neutron capture on gadolinium event.

#### MeanDirAngleMean

This variable takes the mean of angles between the direction of each hit and the mean of the direction of these hits. Again this will be generally shifted to larger values for neutron captures on gadolinium compared to captures on hydrogen, shown in Figure 6.40 and Figure 6.41.

#### MeanDirAngleRMS

This variable is simply the RMS of angles between each hit directon and mean hit direction, here we can see from Figure 6.40 that background events will have a larger spread for this variable compared to signal events.

#### $\beta_l$

This variable is used because the signal and background events have a variation in the angular distribution of the hit PMTs. The  $\beta_l$  variable defines the isotropy of the Cherenkov hits according to:

$$\beta_l = \frac{2}{N_{Hits} (N_{Hits} - 1)} \sum_{i \neq j} P_l (\cos \theta_{ij}) \quad (6.16)$$

where  $P_l$  are the Legendre polynomial's of order  $l$  and  $\theta_{ij}$  is the angle between hit PMTs relative to the neutron capture vertex.  $\beta_1, \beta_2, \beta_3, \beta_4, \beta_5$  are all used as input variables to the NN in order to investigate the geometry of the neutron candidate hits related to spherical harmonics. For the sake of brevity only  $\beta_1$  and  $\beta_5$  are shown here in Figure 6.40 and Figure 6.41. Because this variable is related to the angular distribution, just like the previous angle related variables, background events have a larger spread compared to signal events.

Figure 6.39 shows the neural network likelihood signal between 0 and 1 (TagOut), for all events, neutron capture on hydrogen candidates and neutron capture on gadolinium candidates. The blue arrow shows the cut on this variable (0.7), so that a neutron candidate that has been analysed is determined to be a signal neutron candidate if its value of TagOut  $\geq 0.7$ , and background if it is  $< 0.7$ . The value of 0.7 was chosen due to the amount of background events being sufficiently low enough past this value, while ensuring a substantial amount of neutron capture candidate signals on hydrogen and gadolinium.

Seeing the signal from neutron captures on hydrogen and gadolinium pre and post neural network is also important along with the background events: these are shown in Figure 6.40 and Figure 6.41.

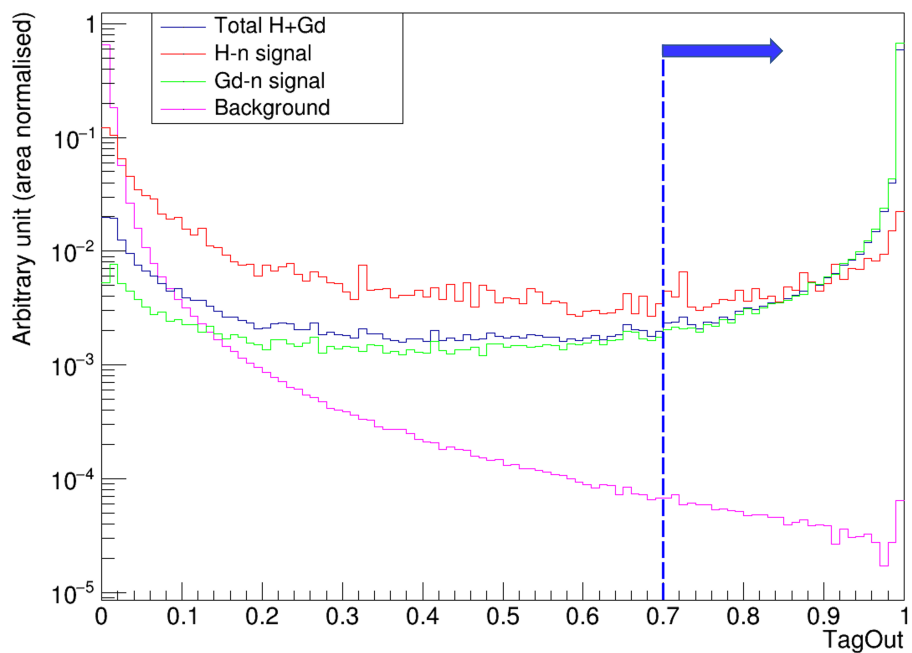


Figure 6.39: Neural network output signal likelihood

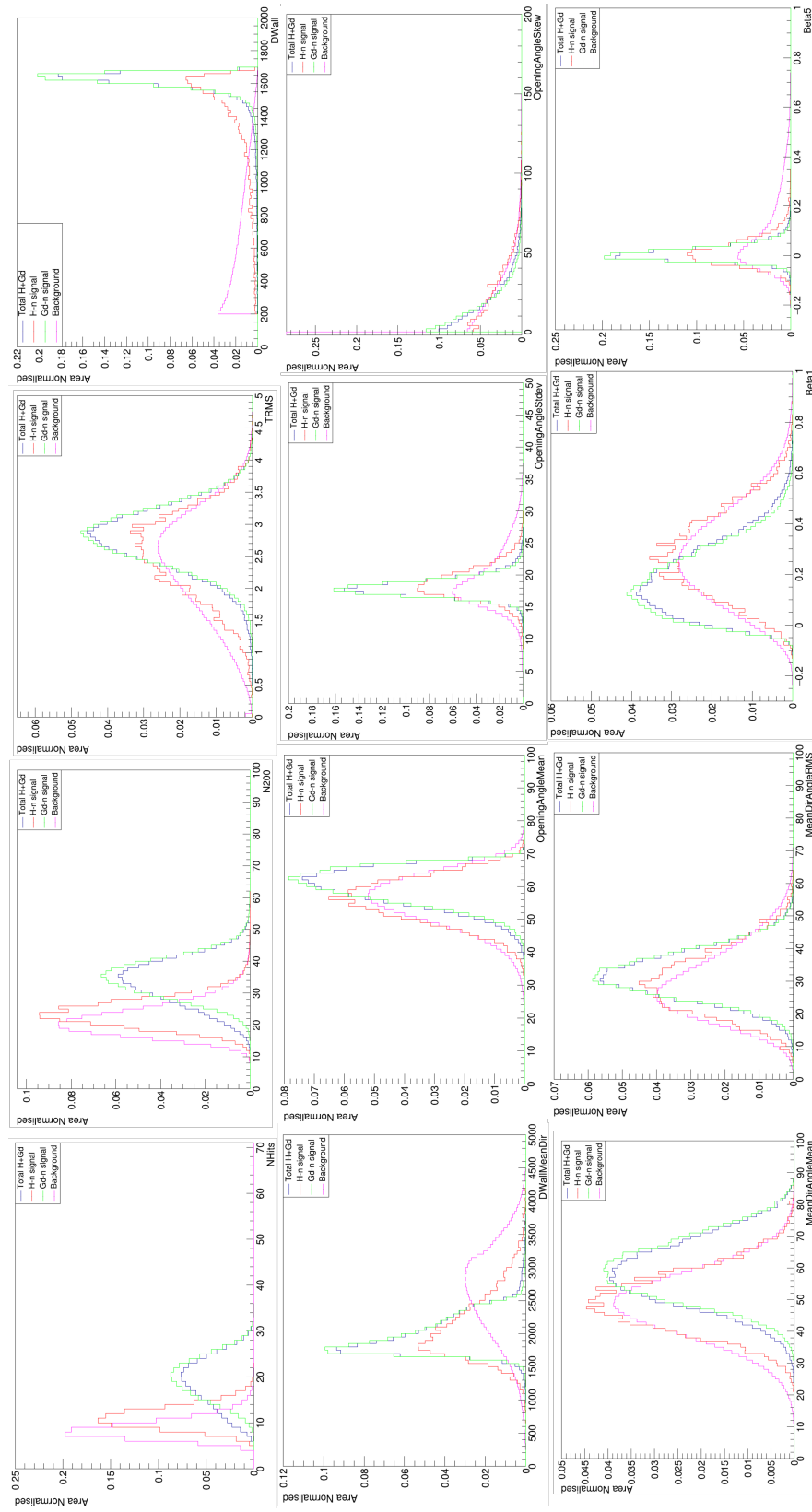


Figure 6.40: Number of events plotted against various neural network input variables prior to the neural network

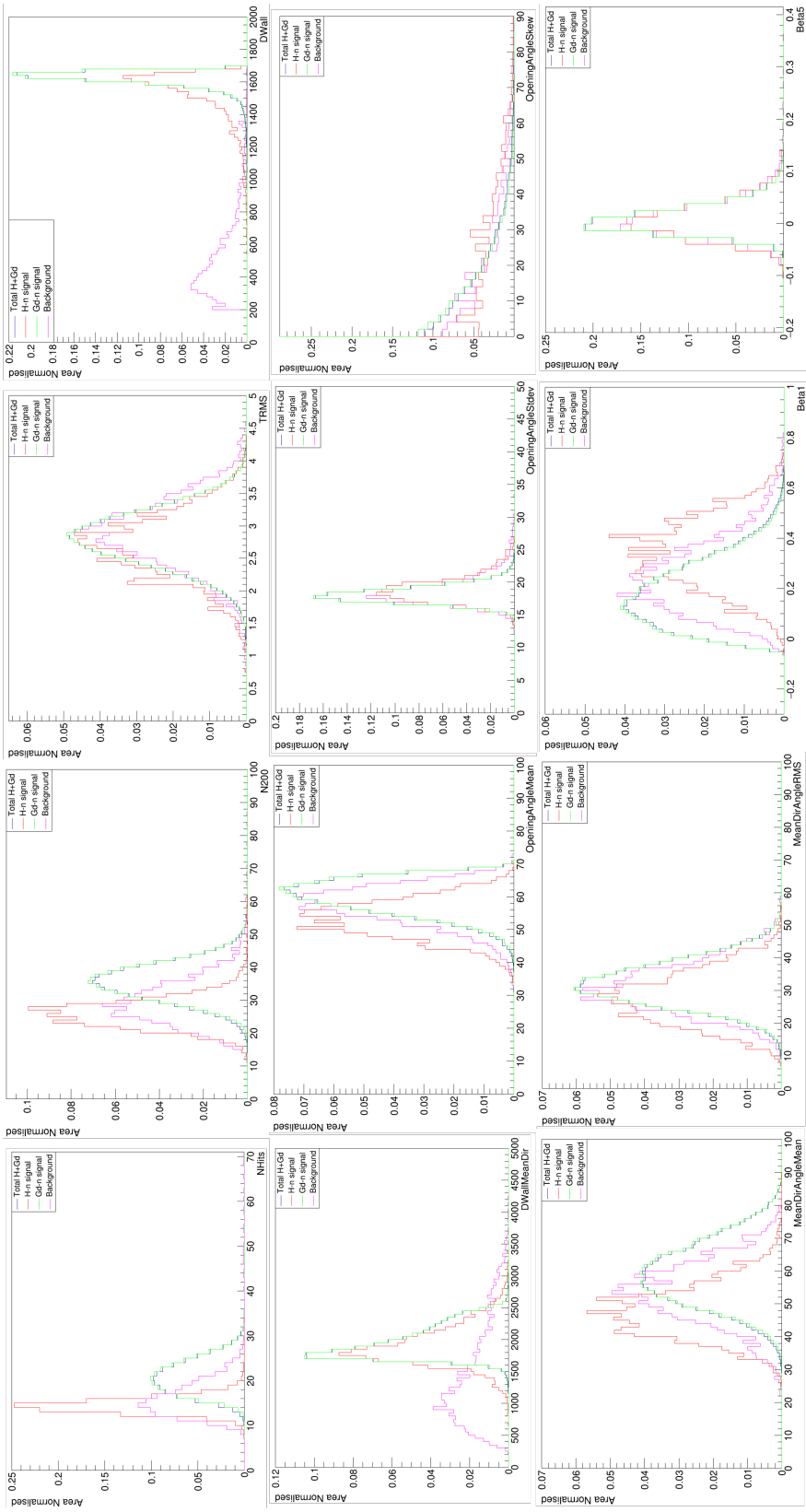


Figure 6.41: Number of events plotted against various neural network input variables after neural network output

Figure 6.39 shows that the signal likelihood output is closer to 0 for far more neutron capture on hydrogen candidates than neutron capture on gadolinium candidates - this is also shown in Figure 6.40 and Figure 6.41, where the peaks for the neutron capture on hydrogen candidates are significantly more reduced in the post-NN plots than in the pre-NN plots, showing that noise events were more likely to be misidentified as neutron captures on hydrogen. These distributions also show that the value of NHits and also N200 for a neutron capture candidate is more likely to be greater for neutron candidates which are candidates on gadolinium than on hydrogen. Additionally, these plots also show that the opening Cherenkov angle related distributions were skewed towards greater values for gadolinium capture candidates than for hydrogen, due to the presence of the hits from the gamma cascade associated with neutron captures on gadolinium.

After investigating the neutron candidates pre and post neural network to see the candidate signal distributions, it makes sense to evaluate how efficient the neutron tagging algorithm is. There are three stages at which the efficiency is calculated, pre-NN selection (i.e. searching all the truth candidates prior to NN selection), after the NN classification (to show the efficiency of the classifier), and then the combination of these (the total tagging efficiency). Equation 6.17 shows how these three stages,  $\varepsilon_{\text{Pre}}$ ,  $\varepsilon_{\text{NN}}$  and  $\varepsilon_{\text{NTag}}$  are defined.

$$\begin{aligned}\varepsilon_{\text{Pre}} &= \frac{\# \text{ of truth candidates at pre - selection}}{\# \text{ of truth neutrons}} \\ \varepsilon_{\text{NN}} &= \frac{\# \text{ of tagged truth neutrons}}{\# \text{ of truth candidates at pre-selection}} \\ \varepsilon_{\text{NTag}} &= \varepsilon_{\text{Pre}} \times \varepsilon_{\text{NN}} = \frac{\# \text{ of tagged truth neutrons}}{\# \text{ of truth neutrons}}\end{aligned}\quad (6.17)$$

The values of these efficiencies and their associated statistical uncertainties are shown in Table 6.8, and are calculated separately for captures on hydrogen and gadolinium and for both.

These efficiencies are as expected, with the efficiency of neutrons captured on gadolinium being much greater than that of captures on hydrogen, due to the gamma cascade making it better able to be differentiated from the 2.2 MeV from the neutron capture on hydrogen. However, as the errors on the efficiency in Table 6.8 are purely statistical (i.e. produced from the number of neutrons in the MC), it is beneficial to do a comparison with an efficiency measurement from actual neutron capture data. In order to assess the validity of the efficiencies from the Monte Carlo, a comparison of the efficiency with data taken from an Am/Be + 8BGO neutron source is used. As mentioned in Chapter 3, the

	Pre-selection efficiency
H + Gd	$50.00 \pm 0.10\%$
H	$13.43 \pm 0.19\%$
Gd	$84.87 \pm 0.10\%$
	NN classification efficiency
H + Gd	$80.30 \pm 0.21\%$
H	$18.96 \pm 1.26\%$
Gd	$89.64 \pm 0.26\%$
	Total efficiency
H + Gd	$40.16 \pm 0.21\%$
H	$2.55 \pm 0.16\%$
Gd	$76.17 \pm 0.20\%$

Table 6.8: NTag pre-selection, NN classification and total efficiencies

Run	Data taking time	Position (m)
85622	1 hour	(0,0,0)
85617	30 min	(0,0,+12)
85586	30 min	(-12,0,0)

Table 6.9: Am/Be data run numbers, data taking time and Am/Be source positions

Am/Be + 8BGO source produces a prompt 4.4 MeV gamma ray along with a neutron, with the same prompt and delay signal pattern as NCQE interactions, and similarly to the MC, a timing distribution of hits relative to the 4.4 MeV trigger can be produced for the Am/Be + 8BGO data. Figure 6.42 shows the Am/Be source container and the BGO scintillator that it is enclosed within, and Figure 6.43 shows the distribution of hits (NHits) within the 14 ns sliding timing window.

As shown in Figure 6.44, the efficiency of the neutron capture changes relative to the DWall cut value, and as a result it was advisable to check the efficiency of neutron capture using Am/Be + 8BGO data at different positions in the detector. Table 6.9 shows the runs and positions (x,y,z) of Am/Be + 8BGO data used in this analysis.

First, comparison was done between the MC and the Am/Be data from Run 85622,

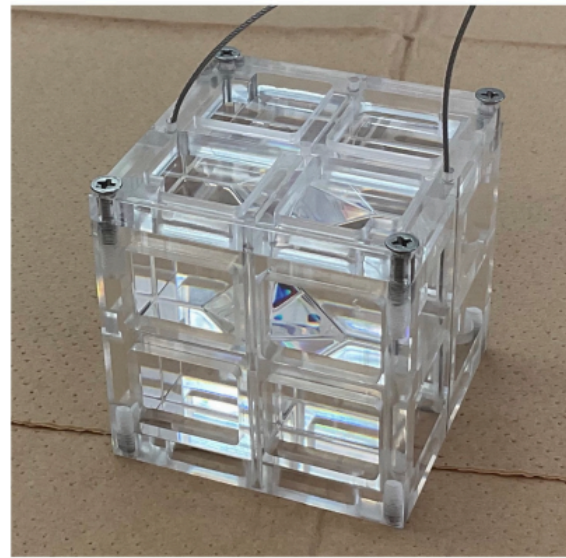


Figure 6.42: Am/Be + 8BGO source: the Am/Be source is housed at the centre of the 8 BGO crystals, which are  $2.5 \times 2.5 \times 2.5$  cm each and themselves placed inside an acrylic case. The edge of each crystal is cut so there is an inner place for the Am/Be source to be kept.

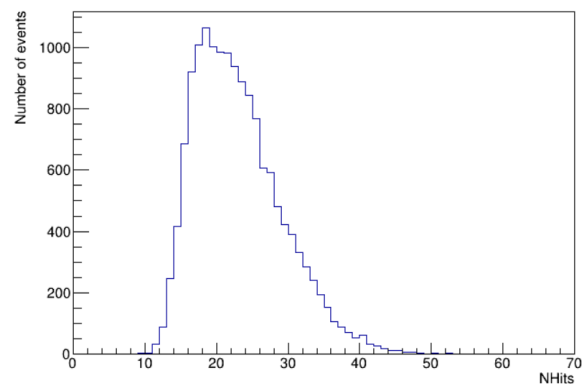


Figure 6.43: Distribution of hits from Am/Be + 8 BGO data within the 14 ns sliding timing window.

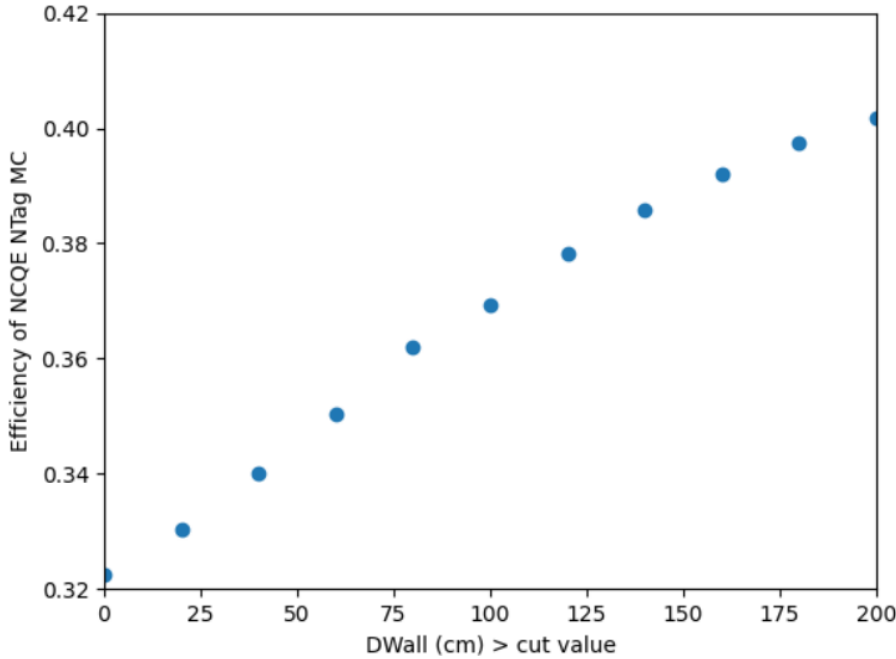


Figure 6.44: Neural network output signal likelihood

the 1 hour measurement taken in the central (0,0,0) source position, by looking at the timing distribution from the 4.4 MeV trigger signal. The same neutron tagging algorithm was used as for the tagging of neutrons from the MC, with the exact same primary and secondary selection criteria. In addition to this, the following event cuts were used in order to select neutron capture events using this data: the total event charge deposit for the inner detector PMTs to be between 850 and 1150 photoelectrons, the time difference from the previous event should be greater than 1 millisecond, and the number of outer detector PMT hits should be less than 10. In order to find the efficiency of the neutron captures and to find the fitted background with this Am/Be data, an exponential fit was made to the timing distribution (shown in Equation 6.18), and this is shown in Figure 6.45 by the red curve. Similar plots were made for the Am/Be source data taken for the (0,0,+12 m) and (-12 m,0,0) positions.

$$\text{Fit equation: } Ae^{-t/\tau} + B \quad (6.18)$$

In Equation 6.18,  $t$  is the time from the event trigger in microseconds,  $\tau$  is the expo-

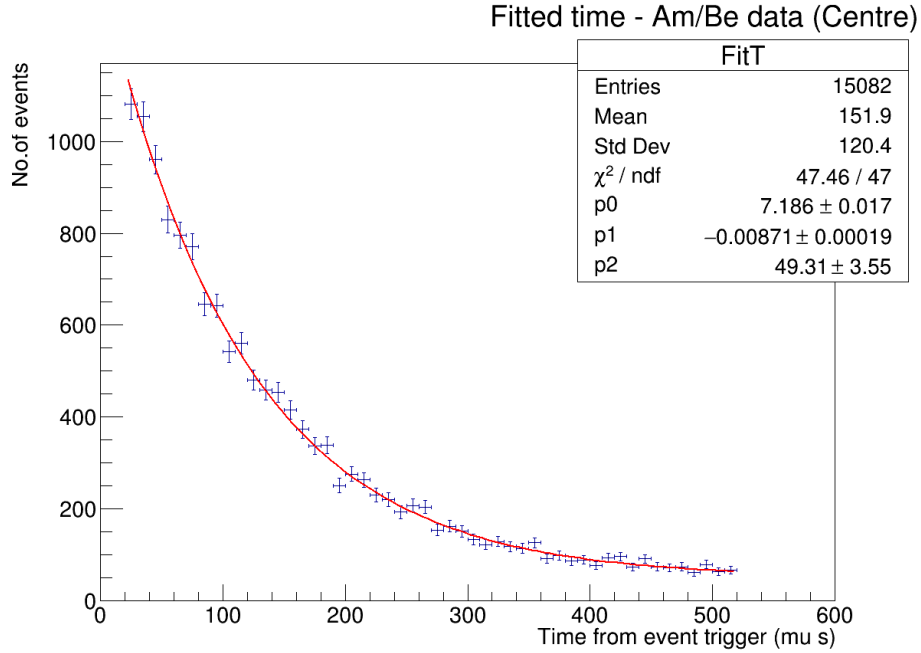


Figure 6.45: Fitted time relative to the trigger signal with exponential fit (red) for the Am/Be data taken in the centre position (0,0,0)

ponential time constant and  $b$  is the background pedestal.

Table 6.10 shows the value of tau for each of these positions, along with the  $\chi^2/\text{ndf}$  value for the exponential fit and the value of the neutron capture efficiency calculated from the Am/Be data at each of these positions. Equation 6.19 shows the method by which the efficiency for the neutron capture on Am/Be data is calculated, by subtracting the number of fitted background events from the number of tagged neutron capture events, and dividing this value by the total number of events. Here  $N$  is the number of neutron captures,  $B$  is the fitted constant background value, and NTag TMAX and NTag TMIN are the end and start times of the neutron tagging algorithm.

$$\text{Efficiency} = \frac{(N - (B \cdot \text{no. of bins} \cdot (\text{NTag TMAX} - \text{NTag TMIN}) / (\text{fit time range})))}{\text{no. of events}} \quad (6.19)$$

This level of variation for the time constant is within normal limits, especially considering the associated errors, and the  $\chi^2/\text{ndf}$  values for each shows that the exponential fit to the data is good. Figure 6.48 shows the equivalent fitted time from the prompt event

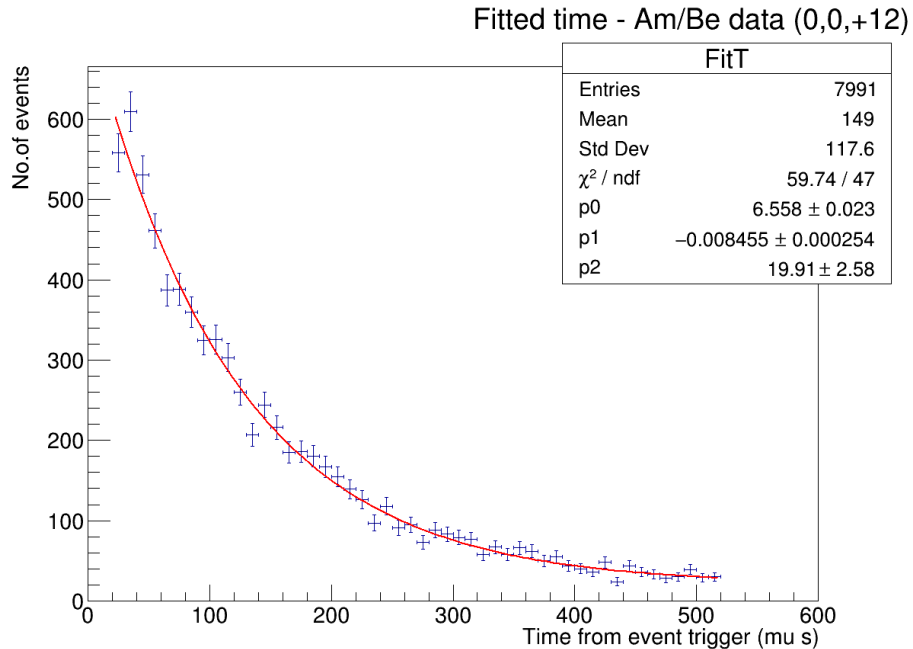


Figure 6.46: Fitted time relative to the trigger signal with exponential fit (red) for the Am/Be data taken at (0,0,+12 )

Position (m)	$(\tau)$ value ( $\mu$ s)	B	$\chi^2/\text{ndf}$	Efficiency (%)	No. tagged neutrons
Centre (0,0,0)	$114.8 \pm 2.5$	$49.3 \pm 3.6$	1.01	40.7	15082
(0,0,+12 )	$118.3 \pm 3.5$	$19.9 \pm 2.6$	1.27	39.4	7991
(-12,0,0)	$109.6 \pm 3.7$	$21.7 \pm 2.2$	1.17	40.7	6438

Table 6.10: Am/Be time constant value and efficiency values along with the  $\chi^2/\text{ndf}$  value of the exponential fit, the value of the background pedestal (B) events and the number of tagged neutrons from the Am/Be source at different positions.

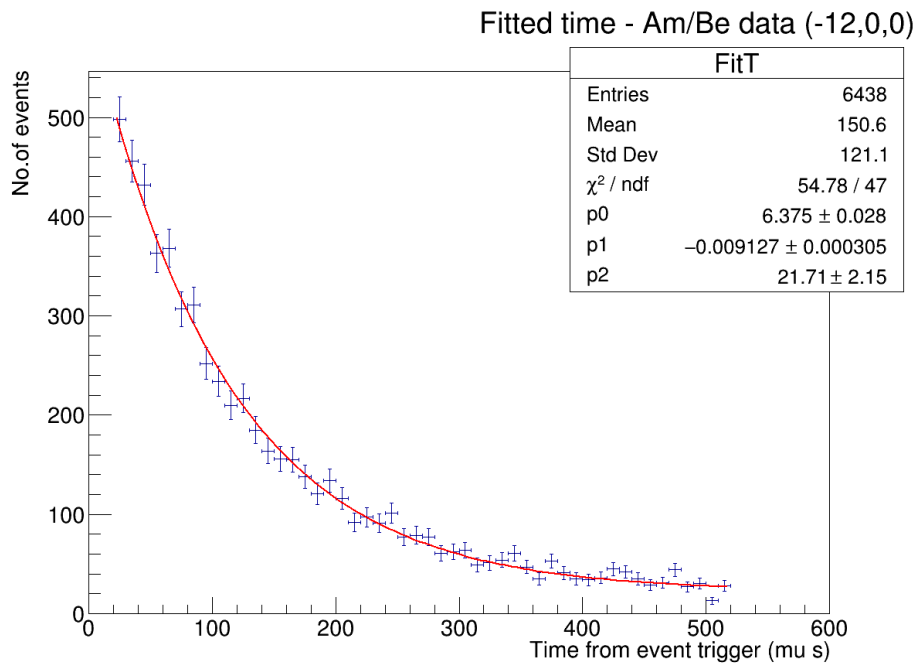


Figure 6.47: Fitted time relative to the trigger signal with exponential fit (red) for the Am/Be data taken at (-12,0,0).

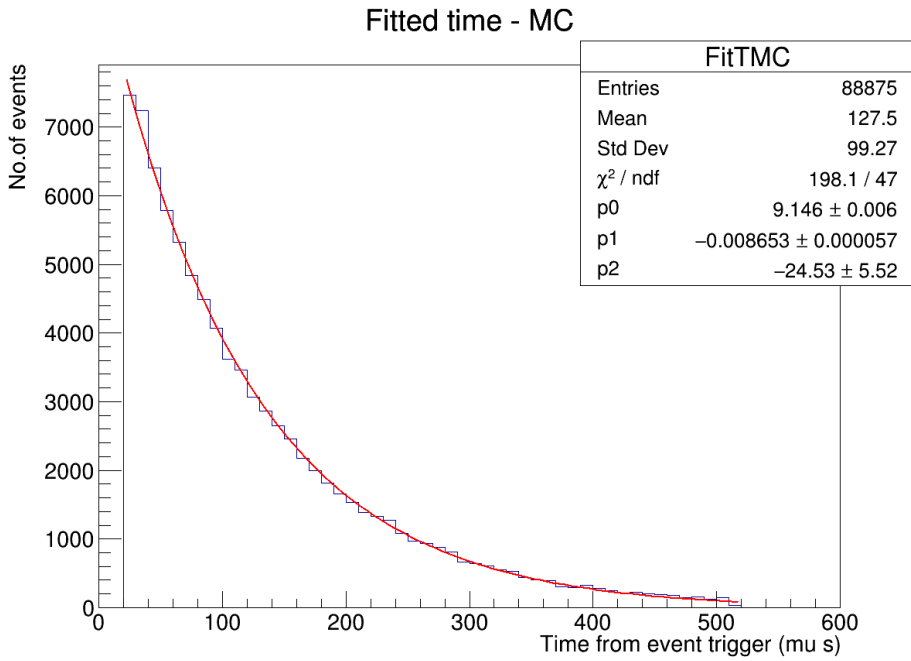


Figure 6.48: Fitted time relative to the trigger signal with exponential fit (red) for the NCQE MC

for the NCQE MC, which has a corresponding time constant value of  $115.6 \pm 0.8 \mu\text{s}$ , and a neutron tagging efficiency, as shown in Table 6.8 of 40.2%: these values are in good agreement with the values shown in Table 6.10.

In conclusion, the work in this chapter involved investigating NCQE interactions via looking at the distributions of neutrons using Monte Carlo simulations post the addition of  $\text{Gd}_2(\text{SO}_4)_3 \cdot 8\text{H}_2\text{O}$  to the Super-Kamiokande detector. Previous NCQE analyses have used pure water based Monte Carlo simulations, however my analysis extended beyond that due to the inclusion of gadolinium in the detector simulator, with neutron captures on it being modelled by the previously unused ANNRI-Gd model. Comparisons of prompt event reconstruction were carried out between pure-water and gadolinium simulation to ensure minimal changes to the prompt event as only the neutron capture in the simulation should be affected. Additionally, my analysis was the first to use a new NTag algorithm for NCQE interactions and comparisons between the legacy and new NTag algorithm were done to ensure that prompt event reconstruction and neutron truth information were consistent between the two algorithms, both prior to and after NCQE sample selection. The new NTag algorithm primary selection criteria were defined along with the algorithm method of

neutron capture vertex reconstruction, and a definite improvement to the neutron capture vertex resolution in MC was seen as a result of the addition of gadolinium to the simulation. To better improve sensitivity to signal events and to reduce background events an artificial neural network was used on neutron candidates that passed the primary selection process. These variables were related to the number of hits, neutron capture vertex position, residual hit time and angular distribution. For many of these variables background events had a distribution that differed greatly from signal events, as well as neutron capture on hydrogen events varying from neutron capture on gadolinium events, and being able to better isolate these different types of captures was interesting. The efficiency of the neutron tagging algorithm was also calculated both before and after the neural network, with the neutron captures on gadolinium having a greater efficiency as expected.

Finally in order to validate the efficiency of the NCQE MC, comparisons were made with Am/Be + 8BGO calibration data. By comparing the timing distributions fitted with an exponential, the neutron capture efficiency was calculated for the Am/Be + 8BGO data at different positions in the tank, with the values for the time constant and the efficiencies being very compatible with the NCQE MC, proving the efficiencies to be valid.

# Chapter 7

## Systematic uncertainty calculations

### 7.1 Systematic uncertainty calculation methodology

The two ways in which the systematic error for this analysis are estimated are either using MC re-weighting or MC regeneration.

For the MC-reweighting approach, weights are applied to a quantity and the tagging efficiency of the re-weighted MC is extracted. The general methodology is to have the input of a model (given by a set of parameters) and to vary them one by one and then calculate the reweighted tagging efficiencies - the set of relative discrepancies  $\delta_i$  are computed from this set of reweighted tagging efficiencies  $T_i$  and the nominal tagging efficiency  $T_{nom}$  using Equation (7.1).

$$\delta_i = \frac{T_i - T_{nom}}{T_{nom}} \quad i \in \{ \text{parameters} \} \quad (7.1)$$

These relative discrepancies  $\delta_i$  are used to calculate the one individual discrepancy  $\delta_{\text{reweighted}}$  that would describe the final deviation from the nominal tagging efficiency  $T_{nom}$  due to the systematic error. The parameter  $\delta_{\text{reweighted}}$  describes the model which has been produced through  $1\sigma$  variations of these parameters, therefore the final probability distribution function which describes the deviation from the nominal MC has a Gaussian

distribution with the standard deviation being equal to  $\delta_{\text{reweighted}}$ .

## 7.2 Gamma production from neutron capture detector response

As mentioned previously, the Americium/Beryllium (Am/Be) source produces a prompt 4.4 MeV gamma ray along with a neutron via Equation 7.2.



In Chapter 6, the tagging efficiency of the Am/Be neutron source was calculated for the source in three different positions, and are shown in Table 6.10. The systematic uncertainties in this Chapter are evaluated by calculating the difference between the nominal tagging efficiency and the tagging efficiency arising from a different process, either a different type of simulation, a different model, or in the case of this uncertainty, a difference in the source of neutrons for neutron capture. Equation 7.3 shows how this systematic is quantified; where  $\delta_{\text{Detector}}$  is the fractional discrepancy arising from variation in tagging efficiency,  $T_{\text{AmBe}}$  is the neutron tagging efficiency from the Am/Be data, and  $T_{\text{nom}}$  is the nominal tagging efficiency of the NCQE MC.

$$\delta_{\text{Detector}}^i = \frac{T_{\text{AmBe}}^i - T_{\text{nom}}}{T_{\text{nom}}} \quad (7.3)$$

However, due to Table 6.10 showing three neutron capture uncertainties for the Am/Be data dependent on position, it makes sense to calculate the deviation of each of these from the norminal, using Equation 7.3 where  $i$  denotes the position of the Am/Be source. Equation 7.4 gives the total deviation of the Am/Be tagging efficiency from the nominal, i.e. the total detector response systematic.

$$\delta_{\text{Detector}}^i = T_{\text{AmBe}}^{\text{Centre}} + T_{\text{AmBe}}^{+12z} + T_{\text{AmBe}}^{-12x} \quad (7.4)$$

Equation 7.4 gives a total Am/Be neutron tagging deviation from the nominal of  $\pm 4.47\%$  shown in Table 7.5.

### 7.3 Neutrino beam flux uncertainty

The uncertainty on neutrino beam fluxes can be evaluated by looking at the dependence of the tagging efficiency on the flux variations. The beam fluxes for the four flavour modes ( $\nu_e, \bar{\nu}_e, \nu_\mu, \bar{\nu}_\mu$ ) have the fractional uncertainties given for each mode, FHC and RHC. The binned uncertainties are shown in Figure 7.1.

Each individual bin for the flux is increased/decreased by its error, the Monte Carlo re-weighting method is then used to extract the tagging efficiency for each flux bin, and Equation 7.5 is used to calculate the fractional uncertainty.

$$\delta_i(\pm\sigma) = \frac{T_i(\pm\sigma) - T_{\text{nom}}}{T_{\text{nom}}} \quad i \in \{ \text{each flux bin} \} \quad (7.5)$$

Figure 7.2 shows the fractional errors calculated from the reweighted Monte Carlo, with the red bars showing the  $-1\sigma$  variation and the blue bars showing the  $+1\sigma$  variation. Table 7.5 contains the value for the total uncertainty resulting from the neutrino beam flux, which was calculated using Equation 7.6, where the maximum value between the increased and decreased discrepancy is taken and summed over to produce the final neutrino flux beam uncertainty.

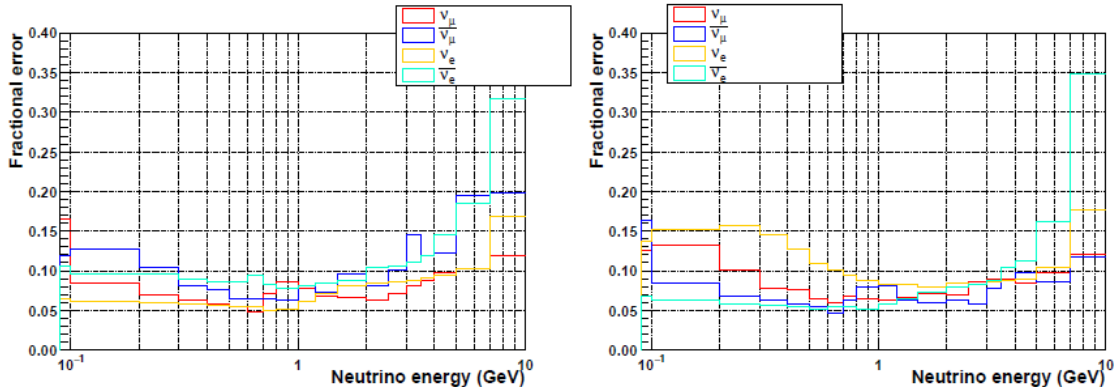


Figure 7.1: Fractional uncertainties of beam fluxes, taken from [34].

$$\delta_{\nu \text{ flux}} = \sum_{i \in \{ \text{bins} \}} \max [|\delta_i(+\sigma)|, |\delta_i(-\sigma)|] \quad (7.6)$$

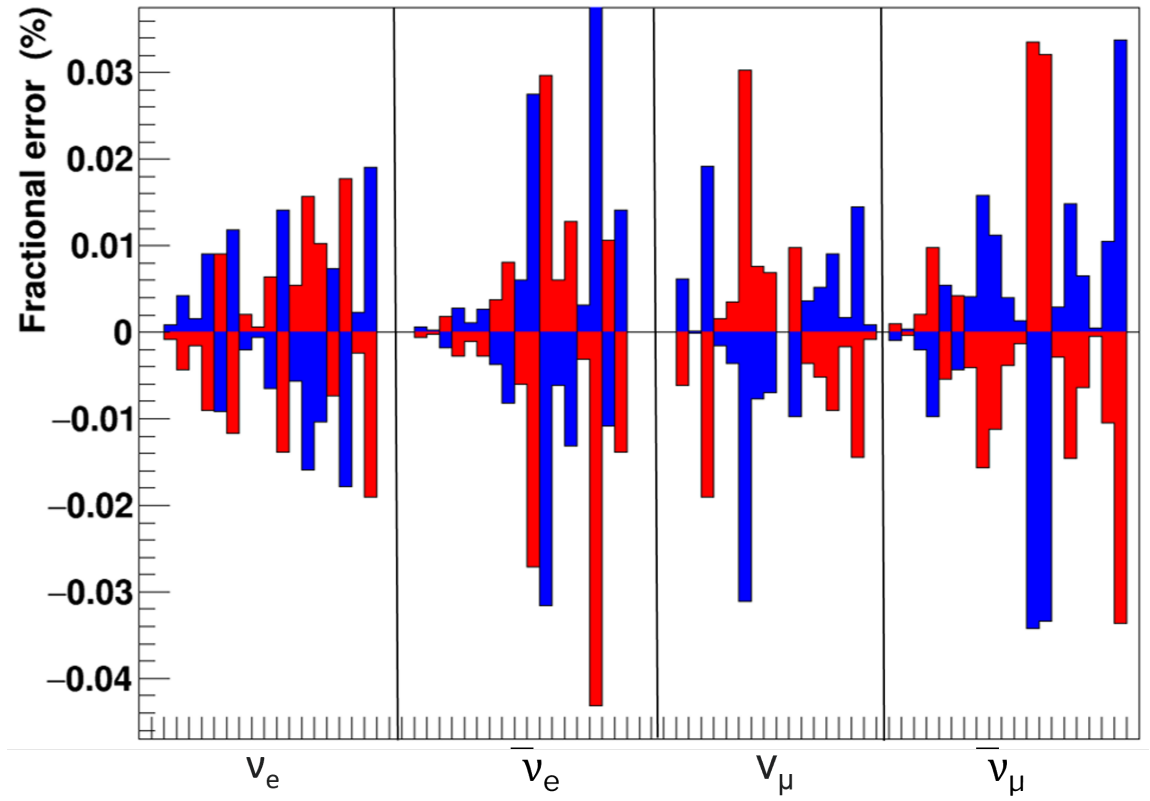


Figure 7.2: Tagging efficiency fractional uncertainties caused by neutrino beam flux discrepancies. From left to right the sections in this plot are comprised of the beam fluxes elements of  $(\nu_e \bar{\nu}_e \nu_\mu \bar{\nu}_\mu)$  respectively.

## 7.4 Neutrino cross section uncertainty

A group of default neutrino cross section values are used to make up the nominal Monte Carlo from which the tagging efficiency is calculated. The values of the parameters that determine the cross sections are shown in Table 7.1. Each of the parameter values relate to a specific interaction type and are either a normalisation parameter or a parameter which shows a kinematic dependence.

For charged current quasi-elastic interactions, the uncertainty is described by the Fermi momentum of the oxygen nucleus, ( $p_F^O$ ), the binding energy of the oxygen nucleus, ( $E_B^O$ ) and the axial mass  $M_A^{CCQE}$ . The axial mass for CCQE interactions relates to the axial

form factor which along with vector form factors is proportional to the cross section of the interactions. For neutrino interactions where two nucleons produce two holes (2p2h), an overall normalisation parameter takes the uncertainty of these interactions into account. For  $CC$  and  $NC1\pi$  interactions, the uncertainty is described by the isospin background, the axial form factor  $C_{A5}^{RES}$  which just like for CCQE interactions relates to the axial mass  $M_A^{RES}$ . For neutral current and charged current interactions (both elastic and inelastic) there are normalisation parameters and energy dependent parameters for the uncertainty to take into account. Finally, for charged current interactions with electron neutrinos, the braking radiation from the lepton in the final state is also considered when calculating the uncertainty and is treated using a normalisation parameter.

The Monte Carlo re-weighting method is used to reweight the nominal Monte Carlo on an event by event basis with each parameter value being increased and decreased by its uncertainty, and for each reweighted Monte Carlo the equivalent tagging efficiency value is extracted. Equation 7.7 shows how the fractional discrepancies are extracted from the nominal and reweighted tagging efficiency values.

$$\delta_i(\pm\sigma) = \frac{T_i(\pm\sigma) - T_{\text{nom}}}{T_{\text{nom}}} \quad i \in \{ \text{parameters} \} \quad (7.7)$$

Figure 7.3 shows the reweighted Monte Carlo fractional uncertainty plotted for the FHC sample. Since this sample contains a lot of NCother interactions, the uncertainty for this interaction type is greater than for the others.

## 7.5 Pion final state interaction (FSI) and secondary interaction (SI) uncertainties

Even though this is an analysis concerned with neutral current quasi elastic interactions, pion events are a significant contribution to the background, and as a result it is important to examine the pion interaction uncertainties both for final state interactions and secondary interactions as their trajectories span the detector.

The neutrino-nucleus interaction simulator used in this analysis (NEUT) handles pion final state interactions and secondary interactions using a cascade model. This cascade model contains parameters which will have uncertainties on them and these will be trans-

Parameter	Interaction	Type	Value
$p_F^O$	CCQE	$^{16}\text{O}$ Fermi momentum	$225 \pm 31\text{MeV}/c$
$E_B^O$	CCQE	$^{16}\text{O}$ binding energy	$27 \pm 9\text{MeV}$
$M_A^{CCQE}$	CCQE	Axial mass	$1.2 \pm 0.41\text{GeV}/c^2$
$2p2h$	2p2 h	Normalization par.	$1.0 \pm 1.0$
$C_{A5}^{RES}$	CC and NC1 $\pi$	Axial form factor	$1.01 \pm 0.12$
$M_A^{RES}$	CC and NC1 $\pi$	Axial mass	$0.95 \pm 0.15\text{GeV}/c^2$
$BG_A^{RES}$	CC and NC1 $\pi$	I = 1/2 continuum background	$1.3 \pm 0.2$
CC other	CC other	E-dependent par.	$0.0 \pm 0.4$
CC elastic	CC elastic	Normalization par.	$1.0 \pm 0.3$
NC other	NC other	E-dependent par.	$1.0 \pm 0.3$
NC elastic	NC elastic	Normalization par.	$1.0 \pm 0.3$
FSe <sup>-</sup> Bremsstrahlung	$CC\nu_e$	Normalization par.	$1.00 \pm 0.03$

Table 7.1: Neutrino cross section parameters. Taken from [47].

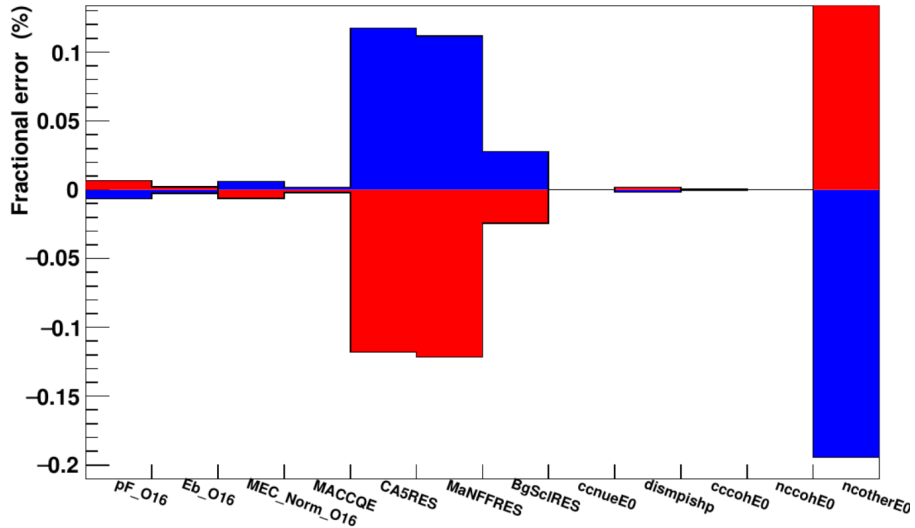


Figure 7.3: Tagging efficiency uncertainty caused by the cross-section parameters variations for the FHC mode

Parameter	Description	Momentum Region (MeV/ $c$ )
$f_{\text{ABS}}$	Absorption	< 500
$f_{\text{QE}}$	Quasi-elastic scatter	< 500
$f_{\text{CX}}$	Single charge exchange	< 500
$f_{\text{QE}H}$	Quasi-elastic scatter	> 500
$f_{\text{CX}H}$	Single charge exchange	> 500
$f_{\text{INEL}}$	Hadron ( $N + n\pi$ ) production	> 500

Table 7.2: Table showing the pion final state interaction parameters in NEUT and the pion momentum range they are used in, taken from [48].

ferred to a possible change in the tagging efficiency.

Depending on the momentum of the pions, different interaction types occur in the model. For pions with a momentum less than 500 MeV, the interactions in place are absorption (ABS), quasi-elastic scattering (QE) and charge exchange (CX).

Absorption occurs when the incident pion is absorbed by the nucleus and no pions remain in the final state. Quasi-elastic (QE) scattering occurs when there is only one pion observed in the final state and it has the same charge as the incident beam. Charge exchange occurs when the charged pion interacts wtht he nucleus and a single  $\pi_0$  can be seen in the final state.

For pions with a momentum of greater than 500 MeV, a different set of interactions are used. Inelastic interactions (INEL) can now produce hadrons and replace absorption processes, but quasi-elastic scattering (QE) and charge exchange (CX) will still occur. The final state interaction parameters and the pion momentum range they are used in can be seen in Table 7.2. Each parameter scales the relevant very small proabability of the charged pion interaction at every stage of the intra-nuclear cascade, aside from the parameter for charge exchange which scales only the fraction of low momentum QE scattering.

A set of parameter variations which determine a surface in paramater space have been estimated by pion scattering experiments, the values for which are shown in Table 7.3. The  $1\sigma$  surface has been explored using the nominal Monte Carlo re-weighting method and the analagous tagging efficiency uncertainty is shown in Equation 7.8, and the uncertainty stemming from the models shown in Table 7.3 is shown in Figure 7.4

$$\delta_i = \frac{T_i - T_{\text{nom}}}{T_{\text{nom}}} \quad i \in \text{parameter vector} \quad (7.8)$$

The pion FSI/SI uncertainty is then calculated using Equation 7.9, which calculated the standard deviation of the fractional uncertainties for each model.

$$\delta_{\pi fsi/si} = \sqrt{\frac{\sum_i (\delta_i - \bar{\delta})^2}{15}} \quad \bar{\delta} = \frac{1}{16} \sum_i \delta_i \quad (7.9)$$

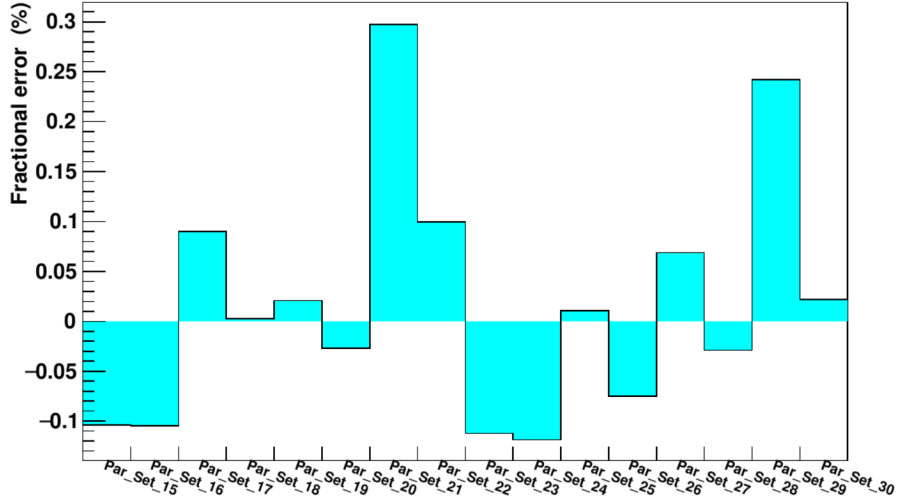


Figure 7.4: Tagging efficiency fractional uncertainty caused by the variation in the FSI/SI model parameters for the FHC mode.

## 7.6 Nucleon final state interactions

Uncertainties regarding the nucleon final state interactions can change the number of nucleons knocked out of  $^{16}\text{O}$ , therefore how the tagging efficiency is changed due to the variation in nucleon final state interactions needs to be investigated. This uncertainty is extracted using GENIE, a Monte Carlo event generator which contains the INTRANUKE (hA) intranuclear transport model. The uncertainties in the total scattering probability for hadrons inside the target nuclei ( $x_{mfp}^N$ ) and the uncertainties in the likelihood of each hadron rescattering method: elastic ( $x_{el}^N$ ), inelastic ( $x_{inel}^N$ ), charge exchange ( $x_{cex}^N$ ), pion

Set	ABS	QE	CX	INEL	QEH	CXH
Nominal	1.1	1.0	1.0	1.0	1.8	1.8
	0.7	0.6	0.5	1.5	1.1	2.3
	0.7	0.6	1.6	1.5	1.1	2.3
Hadron production Up	1.6	0.7	0.4	1.5	1.1	2.3
	1.6	0.7	1.6	1.5	1.1	2.3
	0.6	1.4	0.6	1.5	1.1	2.3
	0.7	1.3	1.6	1.5	1.1	2.3
	1.5	1.5	0.4	1.5	1.1	2.3
	1.6	1.6	1.6	1.5	1.1	2.3
	0.7	0.6	0.5	0.5	2.3	1.3
	0.7	0.6	1.6	0.5	2.3	1.3
	1.6	0.7	0.4	0.5	2.3	1.3
Hadron production Down	1.6	0.7	1.6	0.5	2.3	1.3
	0.6	1.4	0.6	0.5	2.3	1.3
	0.7	1.3	1.6	0.5	2.3	1.3
	1.5	1.5	0.4	0.5	2.3	1.3
	1.6	1.6	1.6	0.5	2.3	1.3

Table 7.3: Pion FSI/SI model parameter nominal value and variations grouped according to inelastic hadron production value, taken from [48].

Abbreviation	Description of uncertainty	Fractional uncertainty
$x_{mfp}^N$	Nucleon mean free path (total rescattering probability)	$\pm 20\%$
$x_{cex}^N$	Nucleon charge exchange probability	$\pm 50\%$
$x_{el}^N$	Nucleon elastic reaction probability	$\pm 30\%$
$x_{inel}^N$	Nucleon inelastic reaction probability	$\pm 40\%$
$x_{abs}^N$	Nucleon absorption probability	$\pm 20\%$
$x_\pi^N$	Nucleon $\pi$ -production probability	$\pm 20\%$

Table 7.4: Nucleon final state interaction parameters of the hA model executed inside GENIE.

production ( $x_\pi^N$ ) and absorption ( $x_{abs}^N$ ) are taken into account. The fractional uncertainties for these modes for pions is shown in Table 7.4.

A nominal GENIE Monte Carlo sample is generated (different from the previously used NEUT Monte Carlo) and this shifted using the re-weighting method to a varied GENIE Monte Carlo by individually increasing and decreasing the parameters in Table 7.4 by its error. For each shifted Monte Carlo produced, the fractional uncertainty can be written as in Equation 7.10.

$$\delta_i(\pm\sigma) = \frac{T_i(\pm\sigma) - T_{\text{nom}}}{T_{\text{nom}}} \quad i \in \{ \text{parameters} \} \quad (7.10)$$

The tagging efficiency fractional uncertainties are displayed in Figure 7.5, showing which parameter from Table 7.4 each uncertainty has arisen from.

Because the parameters in Table 7.4 are independent, the total uncertainty on the nucleon FSI is calculated by summing the fractional uncertainties on the parameters in quadrature, and the maximum difference between each  $\pm\sigma$  pair, as shown in Equation 7.11.

$$\delta_{\text{Nucleon FSI}} = \sqrt{\sum_i \max [\delta_i^2(+\sigma), \delta_i^2(-\sigma)]} \quad (7.11)$$

## 7.7 Muon and pion capture on Oxygen-16

Neutrons are produced from negative muon capture on  $^{16}\text{O}$  as shown in Equation 7.12.

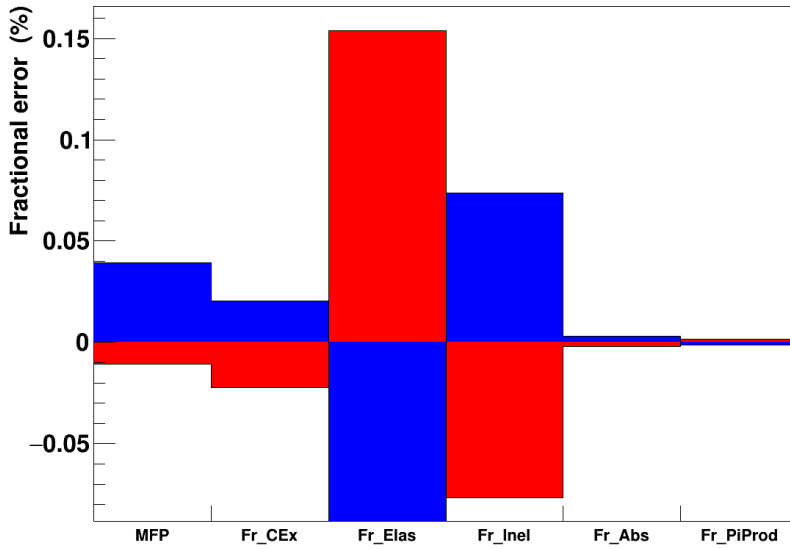


Figure 7.5: Tagging efficiency fractional uncertainties caused by the nucleon final state interaction model parameter variation for the FHC mode



Direct neutrons are produced from pion capture on  $^{16}\text{O}$ , but also a number of evaporation neutrons that leave the nucleus. For the capture of muons and pions on  $^{16}\text{O}$ , the energy spectra of the neutrons produced have been measured: for muons the spectra can range up to 15 MeV, while in the case of pions the spectra can reach up to 100 MeV.

GEANT4 simulates the capture processes for muons and pions, but there are alternate models that can be used: for example, the Chiral Invariant Phase Space (CHIPS) model for muon captures (based on non perturbative QCD) and two different routines for pion capture, one which is based on CHIPS and one based on intra-nuclear cascade.

Because any change in the model can alter the energy spectra of the neutrons, these alternative functions can be used to estimate the fractional uncertainties for the tagging efficiency. This is done by using the MC regeneration method, where the nominal Monte Carlo is regenerated by replacing the default GEANT4 routines with the alternative models. For the alterantive muon capture model and the two alternative pion capture models, the fractional discrepancies are shown in Equation 7.13.

$$\begin{aligned}\delta_{muonCHIPS} &= \frac{T_{muonCHIPS} - T_{nom}}{T_{nom}} \\ \delta_{pionCHIPS} &= \frac{T_{pionCHIPS} - T_{nom}}{T_{nom}} \\ \delta_{pionBert} &= \frac{T_{pionBert} - T_{nom}}{T_{nom}}\end{aligned}\tag{7.13}$$

Figure 7.6 shows the fractional uncertainties caused by muon and pion capture on oxygen for each model.

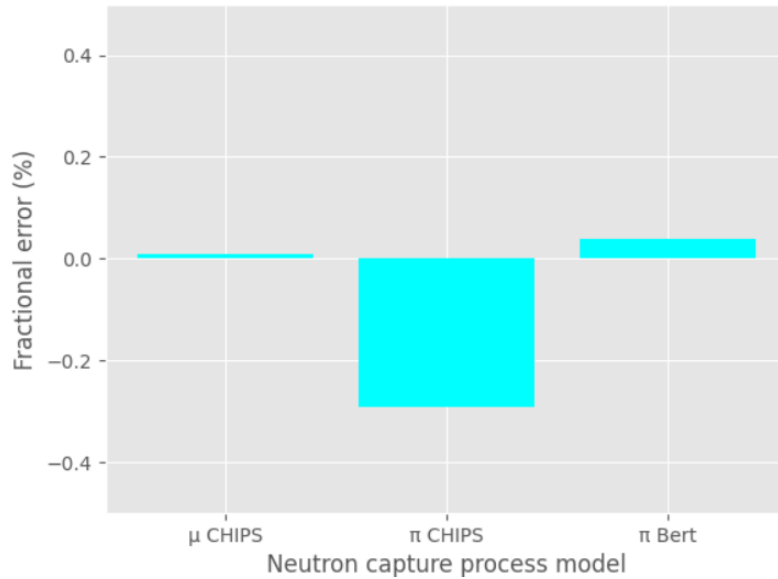


Figure 7.6: Fractional uncertainties in the tagging efficiency caused by muon and pion capture on the muon capture CHIPS model, pion capture CHIPS model and the pion capture Bertini model.

The final muon and pion capture errors are summarised in Equation 7.14 and are presented in Table 7.5.

$$\begin{aligned}\text{Muon capture on } {}^{16}\text{O} &= \delta_{muonCHIPS} \\ \text{Pion capture on } {}^{16}\text{O} &= \delta_{pionCHIPS} + \delta_{pionBert}\end{aligned}\tag{7.14}$$

## 7.8 Nucleon SI

Uncertainties in how Nucleon SI interactions are modelled can affect the tagging efficiency, due to how these uncertainties can affect the final number of nucleons present in the simulation and how far they travel in the detector medium. There are two Monte Carlo code systems used in order to determine how nucleons travel in the simulation, MICAP and HETC. These come as part of GCALOR, used to determine the energy and direction of incident hadrons, leptons and photons. MICAP (Monte-Carlo-Ionization-Chamber-Analysis-Program), which simulates interactions based on calculated cross section and angular distributions for secondary particles, and is called for neutrons with a kinetic energy below 20 MeV. HETC on the other hand, is the High-Energy-Transport-Code, and is responsible for transporting charged hadrons above 20 MeV (up to an energy of 10 GeV) through the detector medium.

### 7.8.1 MICAP uncertainty calculation

A library of cross-section data called ENDF (Evaluated Nuclear Data Files) are used by MICAP to determine what processes the neutrons go through in the detector medium, and their respective cross sections. There are two versions of libraries which are used in evaluating the uncertainty in the tagging efficiency, version B release V (released in 1978) and version B release VIII, released in 2018. There is very little difference between the total neutron on hydrogen cross sections between the two versions of the code, however, in the energy range of 0.1 MeV to 20 MeV, there are differences of up to 40% in the cross-sections of neutron on oxygen, as shown in Figures 7.7 and 7.8. Both an elastic and inelastic part comprise the total cross-section of a nucleus, and these can effect the way neutrons travel in the simulated detector medium and also the way secondary particles from these interactions are distributed. The way these inelastic processes are simulated depend on the nuclei involved: hydrogen nuclei capture the neutrons in the range ( $10^{-11}$ ,  $10^{-7}$ ) MeV, while neutron captures on oxygen mainly happen on the 4 MeV to 20 MeV energy region. To calculate the way uncertainties arise from the way MICAP simulates neutron captures, the ENDF-V library is replaced by ENDF-VIII, and the tagging efficiency using this library ( $T_{VIII}$ ) is evaluated from regenerated MC. Equation 7.15 shows the fractional uncertainty  $\delta_{MICAP}$  regarding MICAP.

$$\delta_{mcp} = \frac{T_{VIII} - T_{nom}}{T_{nom}} \quad (7.15)$$

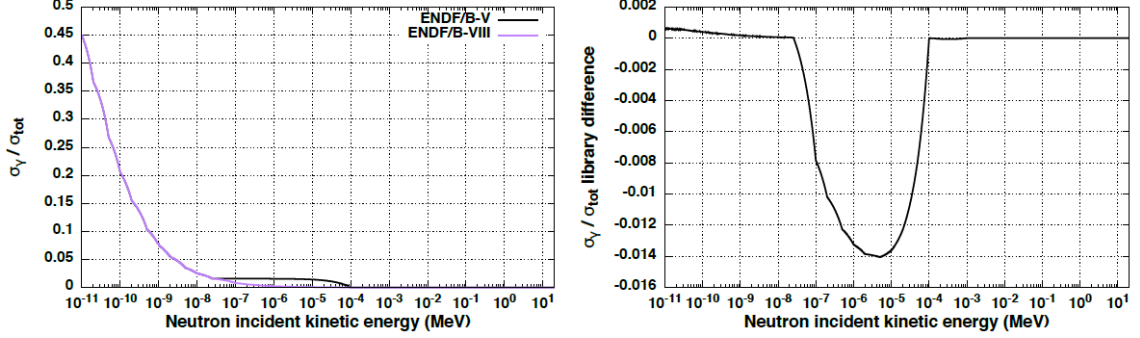


Figure 7.7: Left: Fraction of inelastic cross-section for hydrogen for both the ENDF-V and ENDF-VIII libraries. Right: Difference of the fraction of the inelastic cross-section between the two libraries. Taken from [34].

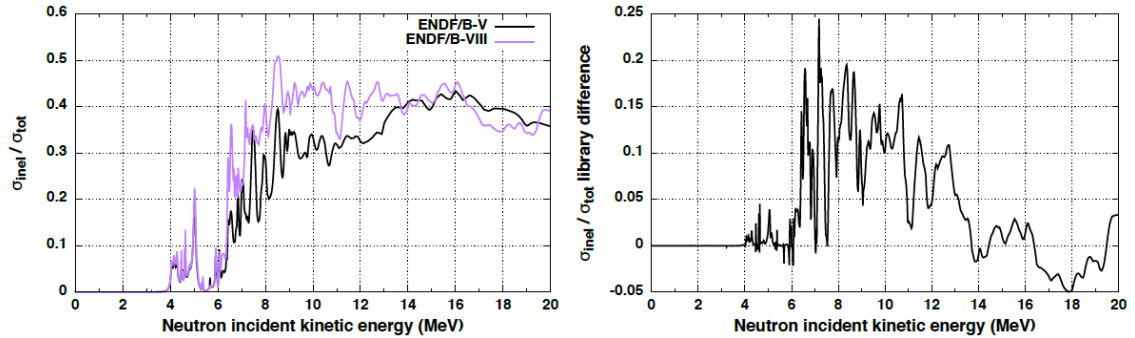


Figure 7.8: Left: Fraction of inelastic cross-section for  $^{16}\text{O}$  for both the ENDF-V and ENDF-VIII libraries. Right: Difference of the fraction of the inelastic cross-section between the two libraries. Taken from [34].

A difference in the inelastic component can change the neutron travel distance, so looking at how changing the Nucleon SI changes the distance between the prompt vertex and the neutron capture vertex is important: this is shown in Figure 7.9.

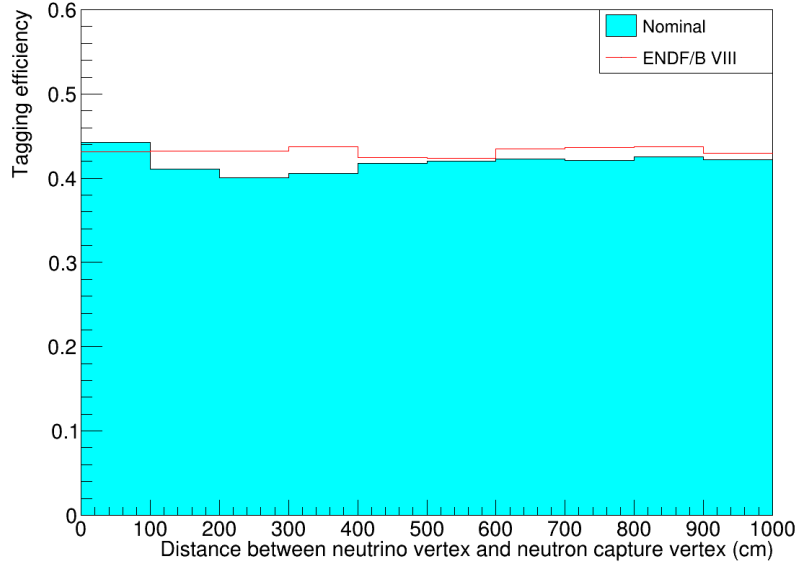


Figure 7.9: Tagging efficiency dependence of the true distance between the neutrino and neutron capture vertices between the ENDF V library (used in the nominal MC, shown in cyan) and the ENDF/B VIII library shown in red.

### 7.8.2 HETC uncertainty calculation

Due to there being no experimental data for cross-section calculations on nucleon-oxygen scattering in the energy range at which T2K functions, experimental data of proton-carbon scattering is used to assign error on the cross sections. In the proton-carbon scattering analysis, NEUT was used to evaluate the theoretical cross sections of carbon, and this uses cross sections calculated using the Bertini model, which is also used in HETC. The comparison of these calculated cross sections to other theoretical calculations as well as to data, showed that the total cross sections calculated by Bertini need to be varied by  $\pm 30\%$  in order to be consistent with them. As a result of this, the Monte Carlo is regenerated twice where the free nucleon-nucleon cross sections are scaled by  $\pm 30\%$ . Figure 7.10 shows the proton-proton(neutron-neutron) and proton-neutron cross-sections with the shaded area around the line representing the values when the cross sections are scaled by  $\pm 30\%$ . Equation 7.16 shows the fractional uncertainty  $\delta_{HETC}(\pm)$ , related to the corresponding tagging efficiencies ( $T_{HETC}(\pm)$ ).

$$\delta_{HETC}(\pm) = \frac{T_{HETC}(\pm) - T_{nom}}{T_{nom}} \quad (7.16)$$

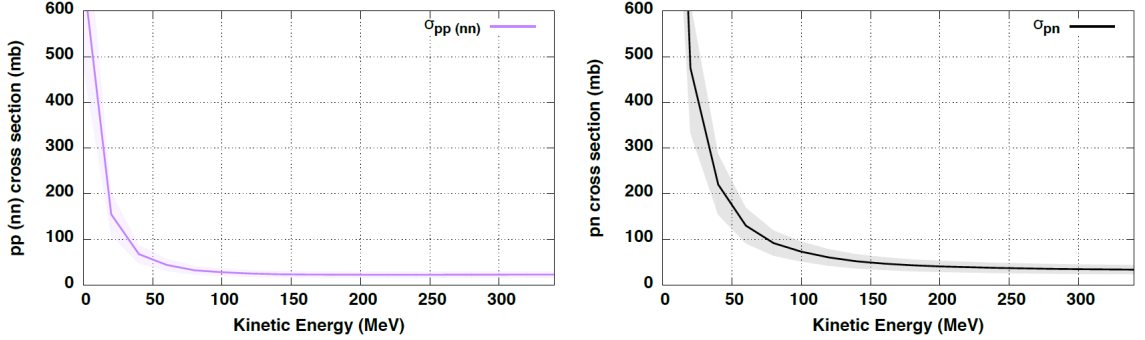


Figure 7.10: Left: proton-proton (neutron-neutron) cross sections, where the shaded area covers the values which are scaled by  $\pm 30\%$ . Right: proton-neutron cross sections, where the shaded area covers the values which are scaled by  $\pm 30\%$ . Taken from [34].

Figure 7.11 shows the dependence of tagging efficiency on the distance between the prompt vertex and neutron capture vertex for the nominal MC and the scaled cross section by  $\pm 30\%$ .

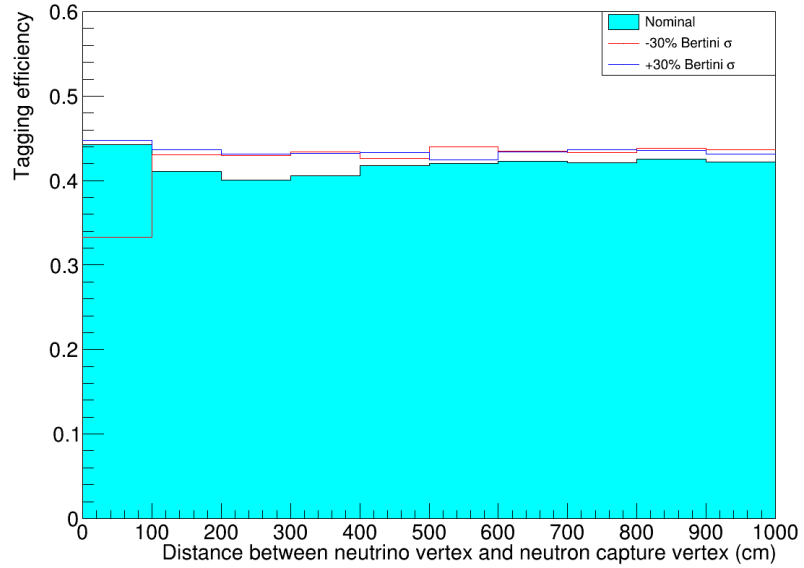


Figure 7.11: Tagging efficiency dependence of the true distance between the prompt vertex and the neutron capture vertex for the nominal MC (cyan) and the  $\pm 30\%$  cross section cases.

The fractional discrepancies regarding the HETC codes are not inherently symmetric which is why the positive and negative uncertainties stemming from the Nucleon SI are

calculated individually as shown in Equation 7.17, and these values are presented in Table 7.5.

$$\begin{aligned}\delta_{\text{Nucleon FSI}}^+ &= |\delta_{\text{MICAP}}| + |\delta_{\text{HETC}}(+\sigma)| \\ \delta_{\text{Nucleon FSI}}^- &= |\delta_{\text{MICAP}}| + |\delta_{\text{HETC}}(-\sigma)|\end{aligned}\quad (7.17)$$

## 7.9 Uncertainty due to PMT gain simulation

The change in PMT gain over time in the Super-K detector provides a systematic uncertainty for the simulations in this analysis. In SKDETSIM-SKGd the PMT gain drift is modelled by scaling the charge received by the PMT according to Equation 7.18, where  $G_0$  is the amount of average PMT gain value from June 2017.

$$Q \longrightarrow Q \times \left(1 + \frac{G(t) - G_0}{G_0}\right) \quad (7.18)$$

In addition to the gain changing over time, so does the number of PMT hits due to the gain, and this has to be adjusted by a correction factor of  $\alpha$  which has a value of 1.6, shown in Equation 7.19. This value is estimated by comparing calibration data and simulations [49]. For  $\alpha = 1$ , Equation 7.19 reduces to Equation 7.18.

$$Q \longrightarrow Q \times \left(1 + \alpha \frac{G(t) - G_0}{G_0}\right) \quad (7.19)$$

The discrepancies in tagging efficiency for this systematic uncertainty are produced by looking at the fractional uncertainty in tagging efficiencies between  $\alpha = 1.6$  and  $\alpha = 1$ , according to Equation 7.20.

$$\delta_i = \frac{T_i^{\alpha=1.6} - T_i^{\alpha=1}}{T_i^{\alpha=1}} \quad i \in \{ \text{Regeneration points} \} \quad (7.20)$$

### 7.9.1 Final systematic error

Systematic error	Value (%)
PMT gain simulation	$\pm 3.00$
$\nu$ cross section	$\pm 0.30$
$\nu$ beam flux	$\pm 0.60$
$\pi$ FSI/SI	$\pm 0.10$
Nucleon FSI	$\pm 0.20$
Nucleon SI	$\begin{array}{c} +5.40 \\ -5.40 \end{array}$
$\mu$ capture on $^{16}\text{O}$	$\pm 0.01$
$\pi$ capture on $^{16}\text{O}$	$\pm 0.33$
Det. resp. for gamma cascade	$\pm 4.47$

Table 7.5: Final systematic uncertainties for the tagging efficiency

## **Chapter 8**

# **Conclusion**

\*insert conclusion here\*

# Bibliography

- [1] M. Aker et al. Improved upper limit on the neutrino mass from a direct kinematic method by KATRIN. *Physical Review Letters*, 123(22), nov 2019.
- [2] Laurie M. Brown. The idea of the neutrino. *Physics Today*, 31(9):23–28, September 1978. Publisher: American Institute of Physics.
- [3] Luca Nanni. Fermi theory of beta decay: A first attempt at electroweak unification. *Advanced Studies in Theoretical Physics*, 13:281, 07 2019.
- [4] Jr. Cowan, C. L., F. Reines, F. B. Harrison, H. W. Kruse, and A. D. McGuire. Detection of the Free Neutrino: A Confirmation. *Science*, 124(3212):103–104, July 1956.
- [5] G. Danby, J-M. Gaillard, K. Goulian, L. M. Lederman, N. Mistry, M. Schwartz, and J. Steinberger. Observation of high-energy neutrino reactions and the existence of two kinds of neutrinos. *Phys. Rev. Lett.*, 9:36–44, Jul 1962.
- [6] G. Danby, J-M. Gaillard, K. Goulian, L. M. Lederman, N. Mistry, M. Schwartz, and J. Steinberger. Observation of high-energy neutrino reactions and the existence of two kinds of neutrinos. *Phys. Rev. Lett.*, 9:36–44, Jul 1962.
- [7] John N. Bahcall. Solar models: An historical overview. *Nuclear Physics B - Proceedings Supplements*, 118:77–86, apr 2003.
- [8] Bruce T. Cleveland, Timothy Daily, Jr. Raymond Davis, James R. Distel, Kenneth Lande, C. K. Lee, Paul S. Wildenhain, and Jack Ullman. Measurement of the solar electron neutrino flux with the homestake chlorine detector. *The Astrophysical Journal*, 496(1):505–526, mar 1998.

- [9] B. Pontecorvo. Mesonium and anti-mesonium. *Sov. Phys. JETP*, 6:429, 1957.
- [10] Ziro Maki, Masami Nakagawa, and Shoichi Sakata. Remarks on the Unified Model of Elementary Particles. *Progress of Theoretical Physics*, 28(5):870–880, 11 1962.
- [11] Hiroki Nagakura and Kenta Hotokezaka. Non-thermal neutrinos created by shock acceleration in successful and failed core-collapse supernova. *Monthly Notices of the Royal Astronomical Society*, 502(1):89–107, January 2021. arXiv: 2010.15136.
- [12] Sovan Chakraborty, Pijushpani Bhattacharjee, and Kamales Kar. Observing supernova neutrino light curve in future dark matter detectors. *Physical Review D*, 89(1):013011, January 2014.
- [13] K. Hirata and T. et al. Kajita. Observation of a neutrino burst from the supernova SN1987A. *Physical Review Letters*, 58(14):1490–1493, April 1987.
- [14] K. S. Hirata et al. Observation in the Kamiokande-II Detector of the Neutrino Burst from Supernova SN 1987a. *Phys. Rev. D*, 38:448–458, 1988.
- [15] H. A. Bethe. Supernova mechanisms. *Reviews of Modern Physics*, 62(4):801–866, October 1990.
- [16] Shin’ichiro Ando and Katsuhiko Sato. Relic neutrino background from cosmological supernovae. *New Journal of Physics*, 6:170–170, November 2004. arXiv: astro-ph/0410061.
- [17] Ll. Martí and M. et al. Ikeda. Evaluation of gadolinium’s action on water Cherenkov detector systems with EGADS. *Nuclear Instruments and Methods in Physics Research Section A: Accelerators, Spectrometers, Detectors and Associated Equipment*, 959:163549, April 2020.
- [18] K. et al. Abe. The T2K Neutrino Flux Prediction. *Physical Review D*, 87(1):012001, January 2013. arXiv: 1211.0469.
- [19] K. et al. Abe. The T2K Experiment. *Nuclear Instruments and Methods in Physics Research Section A: Accelerators, Spectrometers, Detectors and Associated Equipment*, 659(1):106–135, December 2011. arXiv: 1106.1238.

- [20] K. Abe et al. Measurements of the t2k neutrino beam properties using the INGRID on-axis near detector. *Nuclear Instruments and Methods in Physics Research Section A: Accelerators, Spectrometers, Detectors and Associated Equipment*, 694:211–223, dec 2012.
- [21] Yoichiro Suzuki. The Super-Kamiokande experiment. *The European Physical Journal C*, 79(4):298, April 2019.
- [22] S. Fukuda and Y. et al. Fukuda. The Super-Kamiokande detector. *Nuclear Instruments and Methods in Physics Research Section A: Accelerators, Spectrometers, Detectors and Associated Equipment*, 501(2-3):418–462, April 2003.
- [23] P. Fernández. Status of GADZOOKS!: Neutron Tagging in Super-Kamiokande. *Nuclear and Particle Physics Proceedings*, 273-275:353–360, April 2016.
- [24] H. Nishino, K. Awai, Y. Hayato, S. Nakayama, K. Okumura, M. Shiozawa, A. Takeda, K. Ishikawa, A. Minegishi, and Y. Arai. High-speed charge-to-time converter ASIC for the Super-Kamiokande detector. *Nuclear Instruments and Methods in Physics Research Section A: Accelerators, Spectrometers, Detectors and Associated Equipment*, 610(3):710–717, November 2009. arXiv: 0911.0986.
- [25] K Ueno. Analysis of nuclear de-excitation gamma-rays induced by neutrino-nucleon neutral-current interactions at SK using the T2K RUN-I/II data. page 87.
- [26] S Lo Meo, C Massimi, and Rocchi et al. Measurement of the neutron capture cross section for 155Gd and 157Gd for Nuclear Technology. page 8.
- [27] K. et al. Abe. First gadolinium loading to Super-Kamiokande. *Nuclear Instruments and Methods in Physics Research Section A: Accelerators, Spectrometers, Detectors and Associated Equipment*, page 166248, December 2021.
- [28] K. et al. Abe. Calibration of the Super-Kamiokande Detector. *Nuclear Instruments and Methods in Physics Research Section A: Accelerators, Spectrometers, Detectors and Associated Equipment*, 737:253–272, February 2014. arXiv: 1307.0162.
- [29] Robin M. Pope and Edward S. Fry. Absorption spectrum (380–700 nm) of pure water. ii. integrating cavity measurements. *Appl. Opt.*, 36(33):8710–8723, Nov 1997.

- [30] Duncan T. Moore. Gradient-index optics: a review. *Appl. Opt.*, 19(7):1035–1038, Apr 1980.
- [31] René Brun, F Bruyant, Federico Carminati, Simone Giani, M Maire, A McPherson, G Patrick, and L Urban. *GEANT: Detector Description and Simulation Tool; Oct 1994*. CERN Program Library. CERN, Geneva, 1993. Long Writeup W5013.
- [32] G. E. P. Box and Mervin E. Muller. A Note on the Generation of Random Normal Deviates. *The Annals of Mathematical Statistics*, 29(2):610 – 611, 1958.
- [33] G. Marsaglia and T. A. Bray. A convenient method for generating normal variables. *SIAM Review*, 6(3):260–264, 1964.
- [34] Fabio Iacob. Measurement of neutrino- and antineutrino-oxygen neutral-current quasielastic-like interaction neutron multiplicity by detecting radiative capture on hydrogen at the far detector. *T2K Technical Note*, (415), 2021.
- [35] Tomislav VLADISAVLJEVIC. Constraining the t2k neutrino flux prediction with 2009 na61/shine replica-target data. 2018.
- [36] S. Bienstock. Five sample (nu-nubar, appearance/disappearance, nue CC1pi) joint fit using Ptheta framework. *T2K Technical Note*, (367), 2019.
- [37] Artur M. Ankowski, Omar Benhar, Takaaki Mori, Ryuta Yamaguchi, and Makoto Sakuda. Analysis of gamma ray production in neutral-current neutrino-oxygen interactions at energies above 200 mev. *Physical Review Letters*, 108(5), feb 2012.
- [38] Omar Benhar, Nicola Farina, Hiroki Nakamura, Makoto Sakuda, and Ryoichi Seki. Electron- and neutrino-nucleus scattering in the impulse approximation regime. *Physical Review D*, 72(5):053005, September 2005.
- [39] G. B. King, K. Mahn, L. Pickering, and N. Rocco. Comparing event generator predictions and ab initio calculations of  $\nu - {}^{12}\text{C}$  neutral-current quasielastic scattering at 1 gev. *Phys. Rev. C*, 101:065502, Jun 2020.
- [40] Kaito Hagiwara, Takatomi Yano, Tomoyuki Tanaka, Mandeep Singh Reen, Prentam Kumar Das, Sebastian Lorenz, Iwa Ou, Takashi Sudo, Yoshiyuki Yamada, Takaaki Mori, Tsubasa Kayano, Rohit Dhir, Yusuke Koshio, Makoto Sakuda, Atsushi Kimura, Shoji Nakamura, Nobuyuki Iwamoto, Hideo Harada, Michael Wurm,

William Focillon, Michel Gonin, Ajmi Ali, and Gianmaria Collazuol. Gamma-ray spectrum from thermal neutron capture on gadolinium-157. *Progress of Theoretical and Experimental Physics*, 2019(2), 02 2019. 023D01.

- [41] Tomoyuki Tanaka, Kaito Hagiwara, and Gazzola et al. Gamma Ray Spectra from Thermal Neutron Capture on Gadolinium-155 and Natural Gadolinium. *arXiv:1907.00788 [hep-ex, physics:nucl-ex, physics:physics]*, February 2020. arXiv: 1907.00788.
- [42] M. Malek. A Search for Supernova Relic Neutrinos. *PhD Thesis, State University of New York*, 2003.
- [43] K. Bays, T. Iida, K. Abe, Y. Hayato, K. Iyogi, J. Kameda, Y. Koshio, L. Marti, M. Miura, S. Moriyama, M. Nakahata, S. Nakayama, Y. Obayashi, H. Sekiya, M. Shiozawa, Y. Suzuki, A. Takeda, Y. Takenaga, K. Ueno, K. Ueshima, S. Yamada, T. Yokozawa, H. Kaji, T. Kajita, K. Kaneyuki, T. McLachlan, K. Okumura, K. P. Lee, K. Martens, M. Vagins, L. Labarga, E. Kearns, M. Litos, J. L. Raaf, J. L. Stone, L. R. Sulak, W. R. Kropp, S. Mine, C. Regis, A. Renshaw, M. B. Smy, H. W. Sobel, K. S. Ganezer, J. Hill, W. E. Keig, S. Cho, J. S. Jang, J. Y. Kim, I. T. Lim, J. Albert, K. Scholberg, C. W. Walter, R. Wendell, T. Wongjirad, T. Ishizuka, S. Tasaka, J. G. Learned, S. Matsuno, S. Smith, T. Hasegawa, T. Ishida, T. Ishii, T. Kobayashi, T. Nakadaira, K. Nakamura, K. Nishikawa, Y. Oyama, K. Sakashita, T. Sekiguchi, T. Tsukamoto, A. T. Suzuki, Y. Takeuchi, M. Ikeda, K. Matsuoka, A. Minamino, A. Murakami, T. Nakaya, Y. Fukuda, Y. Itow, G. Mitsuka, M. Miyake, T. Tanaka, J. Hignight, J. Imber, C. K. Jung, I. Taylor, C. Yanagisawa, A. Kibayashi, H. Ishino, S. Mino, M. Sakuda, T. Mori, H. Toyota, Y. Kuno, S. B. Kim, B. S. Yang, H. Okazawa, Y. Choi, K. Nishijima, M. Koshiba, Y. Totsuka, M. Yokoyama, Y. Heng, S. Chen, H. Zhang, Z. Yang, P. Mijakowski, K. Connolly, M. Dziomba, and R. J. Wilkes and. Supernova relic neutrino search at super-kamiokande. *Physical Review D*, 85(5), mar 2012.
- [44] K. Abe et al. Measurement of neutrino and antineutrino neutral-current quasielastic-like interactions on oxygen by detecting nuclear deexcitation gamma-rays. *Physical Review D*, 100(11), dec 2019.

- [45] Hiroyuki Sekiya. The super kamiokande gadolinium project. *Journal of Physics: Conference Series*, 1342(1):012044, jan 2020.
- [46] R. Akutsu. A Study of Neutrons Associated with Neutrino and Antineutrino Interactions on the Water Target at the T2K Far Detector. *PhD Thesis, The University of Tokyo*, 2019.
- [47] K. Mahn. *For Summer 2016 XSEC analyses and onward*, 2018.
- [48] P. Perio. NEUT Systematic Studies for 2010a Analysis. *T2K Technical Note*, (32), 2011.
- [49] L. Wan. Experimental Studies on Low Energy Electron Antineutrinos and Related Physics. *PhD Thesis, Tsinghua University*, 2018.

## **Appendix A**

## **Appendix A**

Figure A.3 shows the occupancy plots for the B1 - B5 collimators from the UKLI Autocalib July 2020 run, while Figure A.4 shows the occupancy plots for the B1 - B5 diffusers from the UKLI Autocalib July 2020 run.

Figure A.5 shows the complete PDFs and CDFs for the B1 - B5 collimator data taken from the test stand at Warwick and Figure A.6 shows the complete PDFs and CDFs for the B1 - B5 diffusers. Figure A.7 show the inverse CDF fits for the collimator, and Figure A.8 shows the inverse CDF fits for the diffuser.

Figure A.9 shows the Monte Carlo simulations of the B1 - B5 collimators and Figure A.10 shows the Monte Carlo simulations of the B1 - B5 diffusers.

Figure A.11 shows the inverse cdf checks for the B1 - B5 diffusers.

Figure A.1: Occupancy plot for the diffuser optics from the UKLI Autocalib July 2020 run

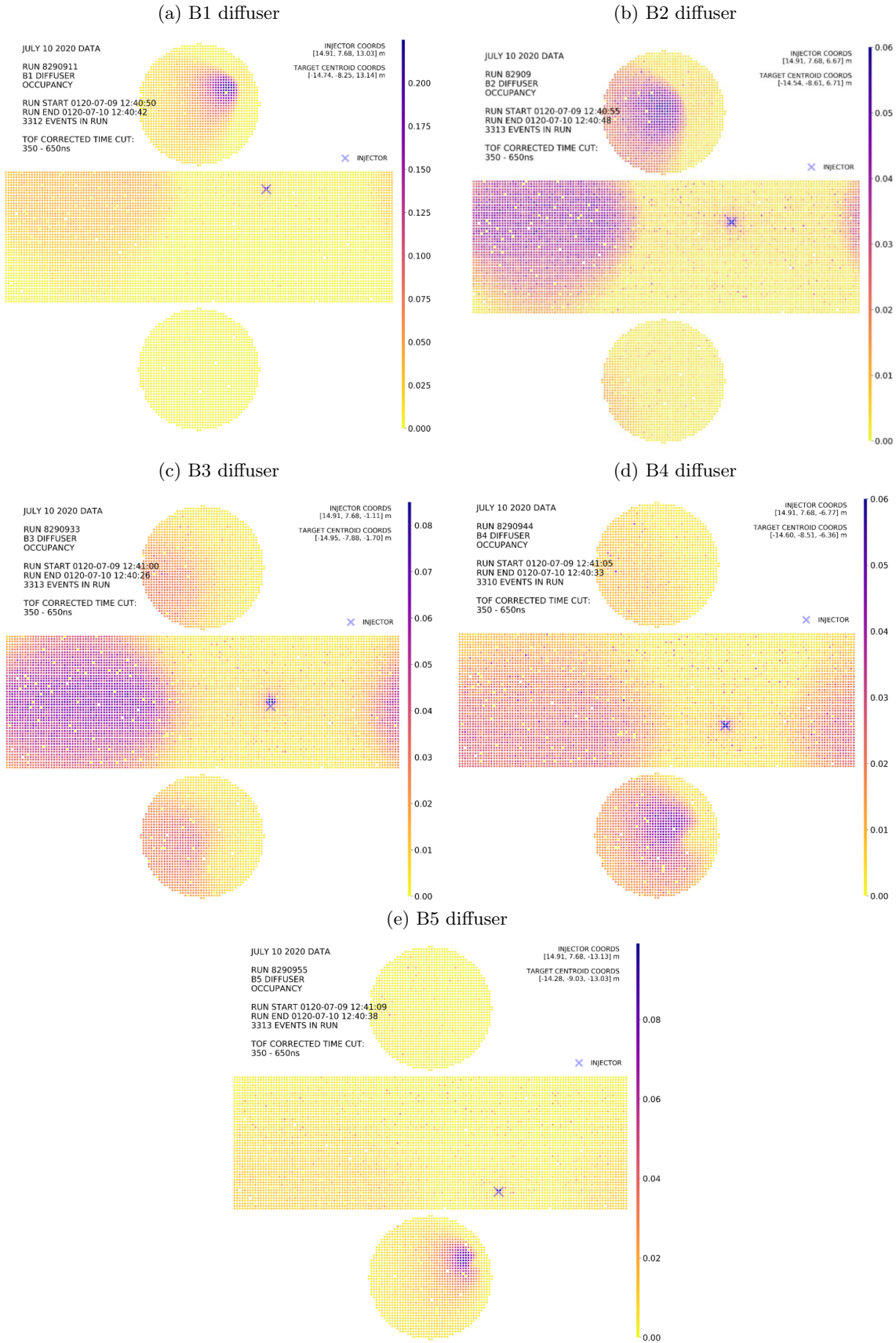


Figure A.2: Occupancy plot for the diffuser optics from the UKLI Autocalib July 2020 run

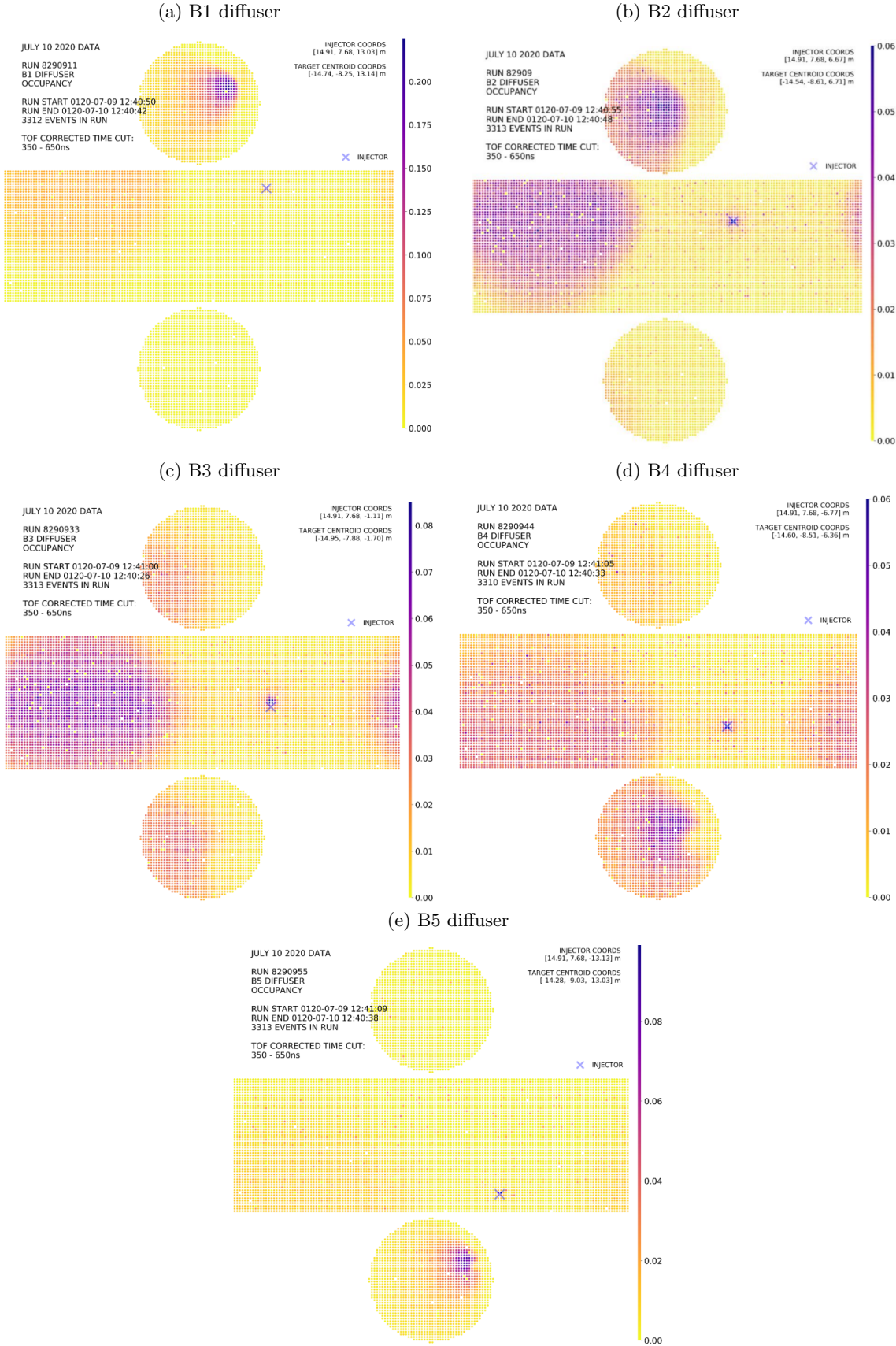


Figure A.3: Occupancy plot for the collimator optics from the UKLI Autocalib July 2020 run



Figure A.4: Occupancy plot for the diffuser optics from the UKLI Autocalib July 2020 run

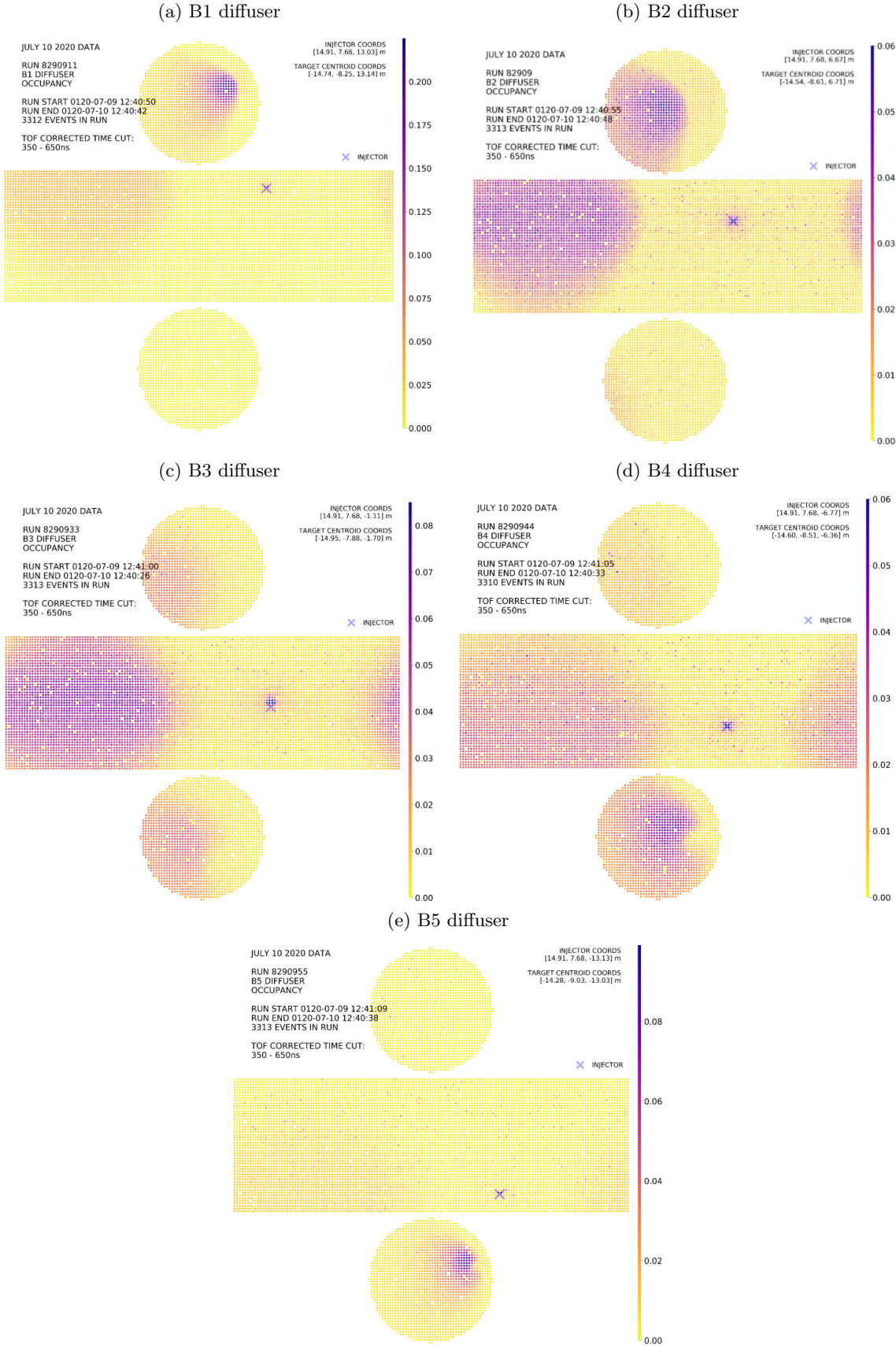
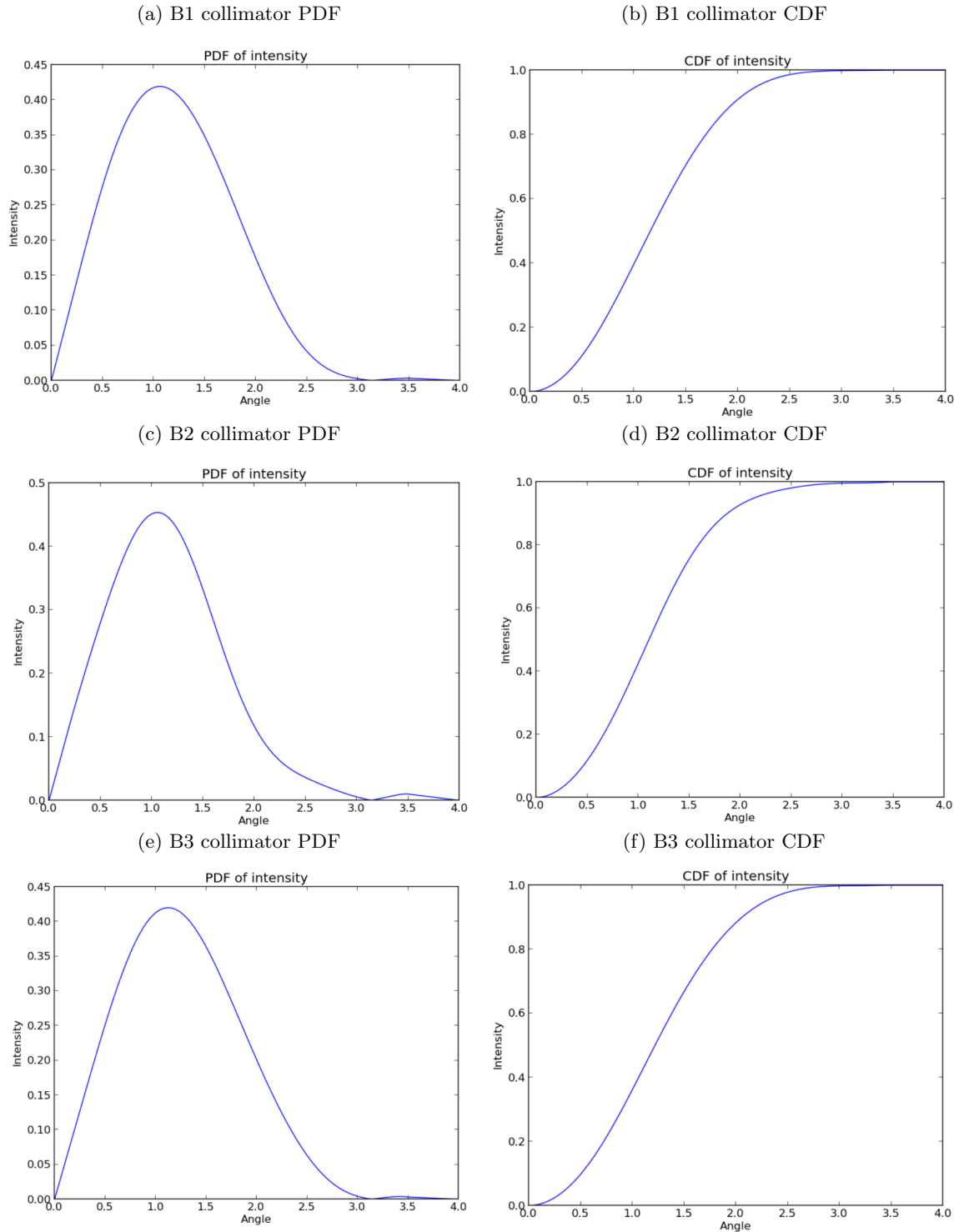
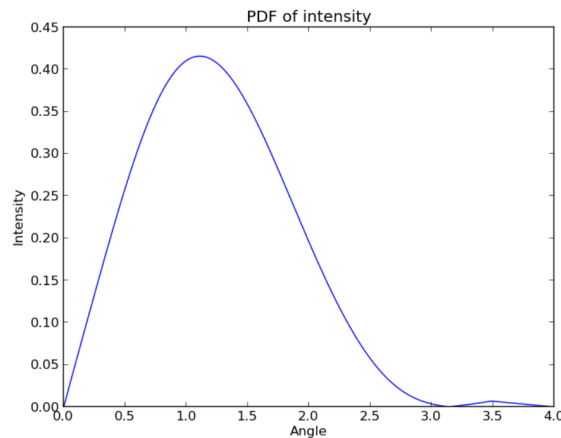
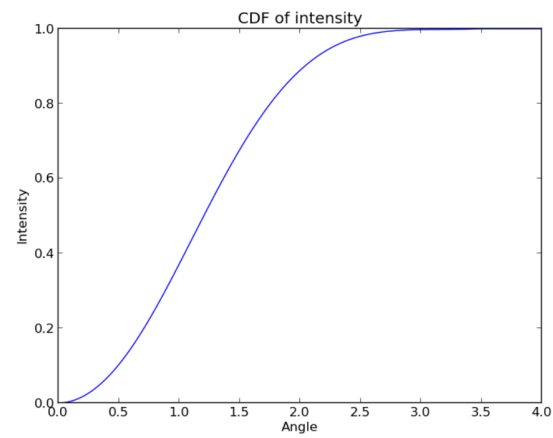


Figure A.5: PDFs and corresponding CDFs for the B1 - B5 collimators

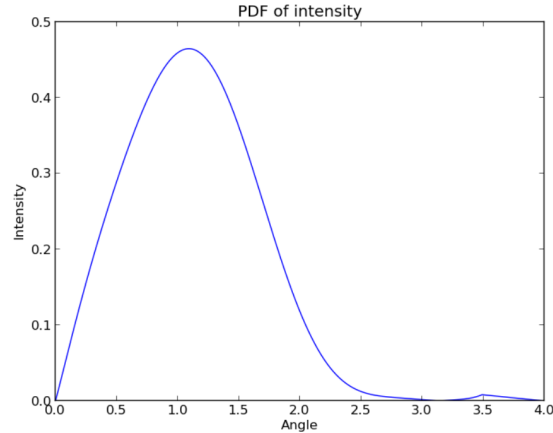




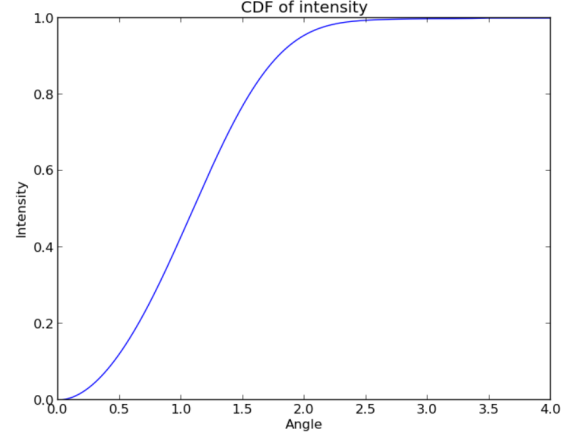
(g) B4 collimator PDF



(h) B4 collimator CDF

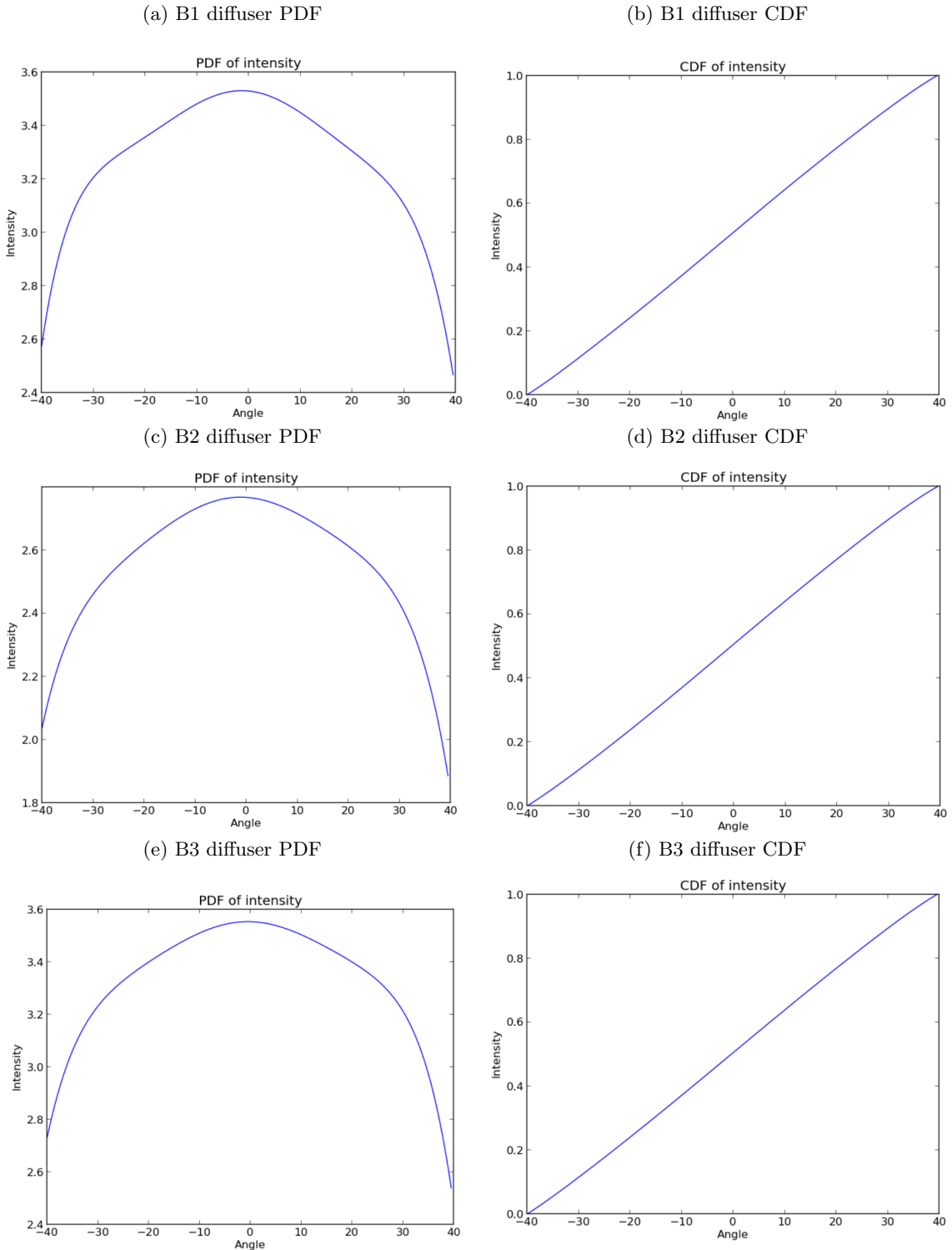


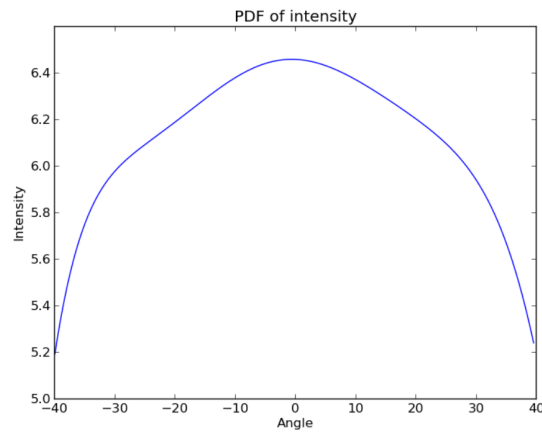
(i) B5 collimator PDF



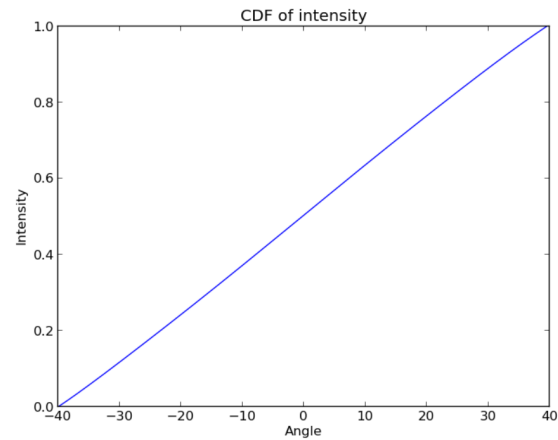
(j) B5 collimator CDF

Figure A.6: PDFs and corresponding CDFs for the B1 - B5 diffusers

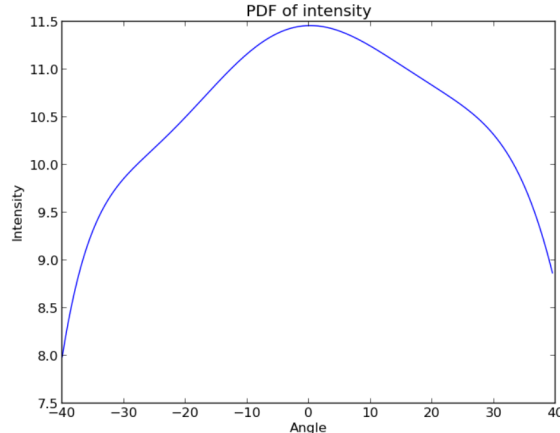




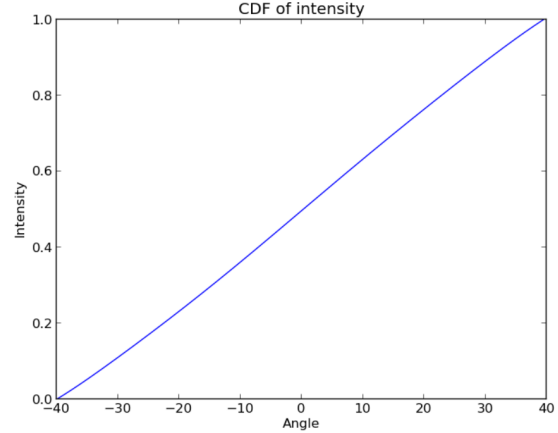
(g) B4 diffuser PDF



(h) B4 diffuser CDF



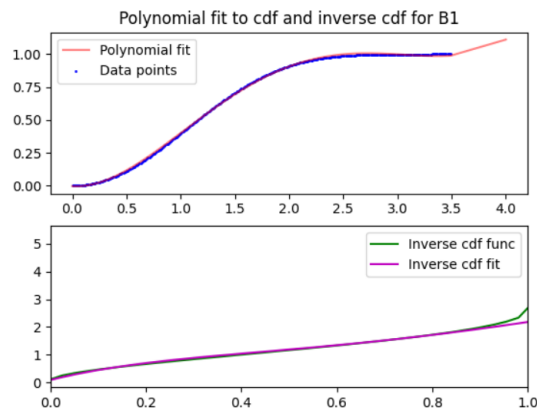
(i) B5 diffuser PDF



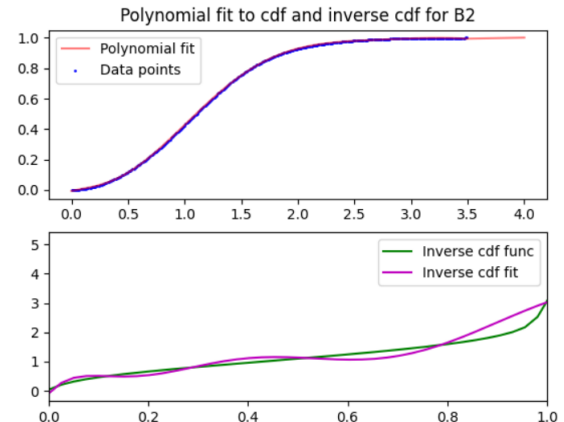
(j) B5 diffuser CDF

Figure A.7: CDF and inverse CDF fits for the B1 - B5 collimator PDFs

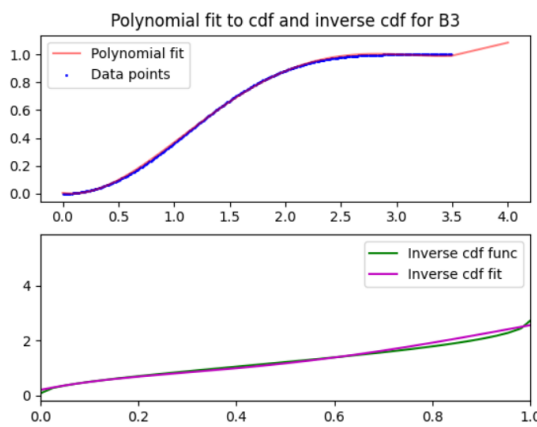
(a) B1 inverse collimator CDF



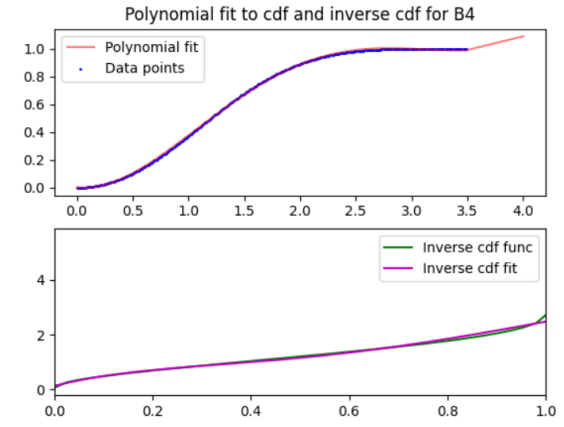
(b) B2 inverse collimator CDF



(c) B3 inverse collimator CDF



(d) B4 inverse collimator CDF



(e) B5 inverse collimator CDF

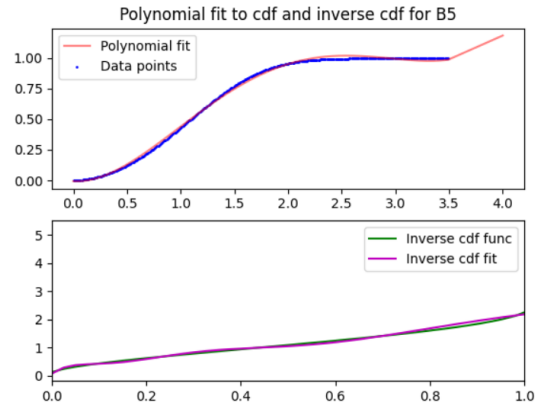


Figure A.8: CDF and inverse CDF fits for the B1 - B5 diffuser PDFs

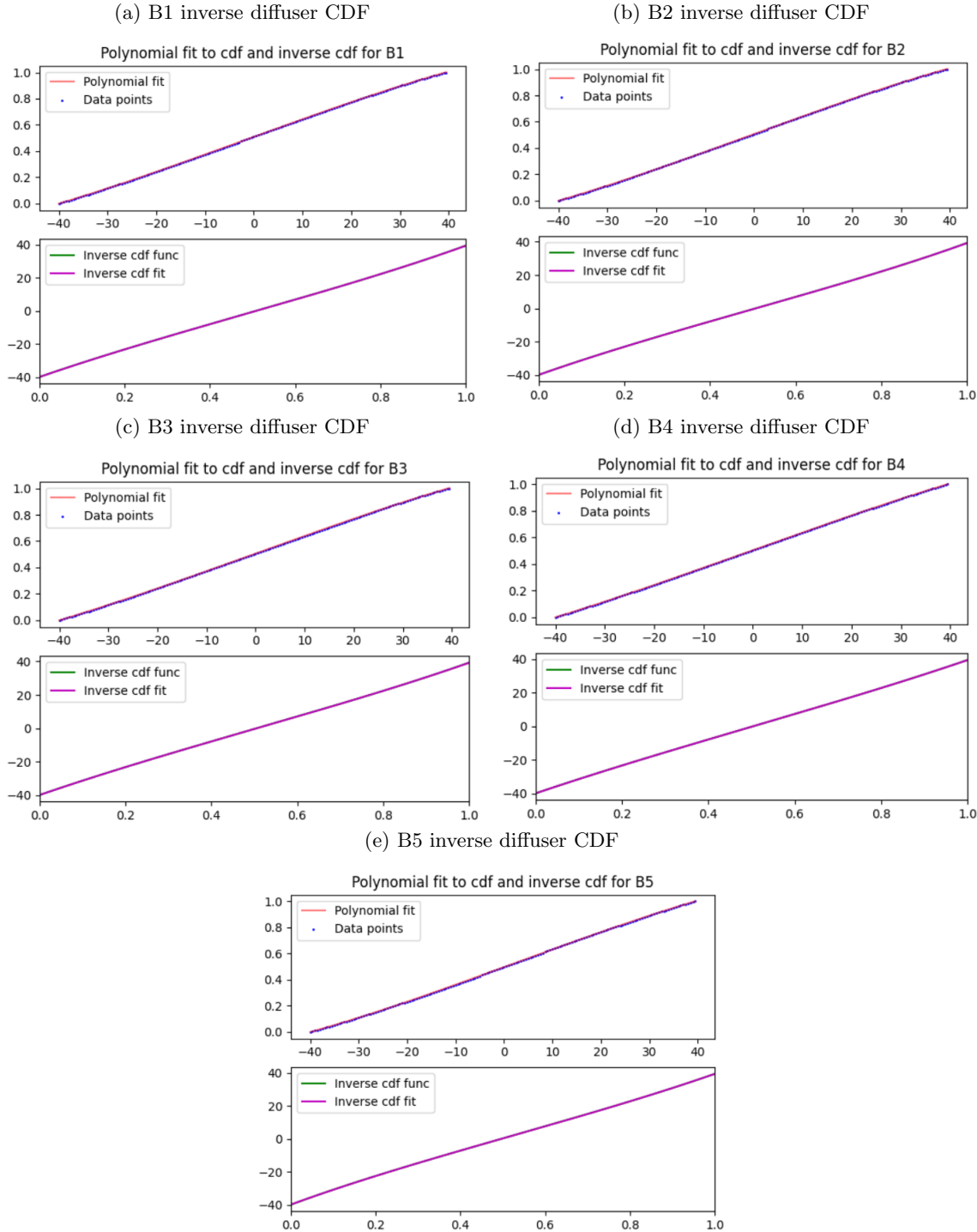


Figure A.9: MC simulations of the B1 - B5 collimators

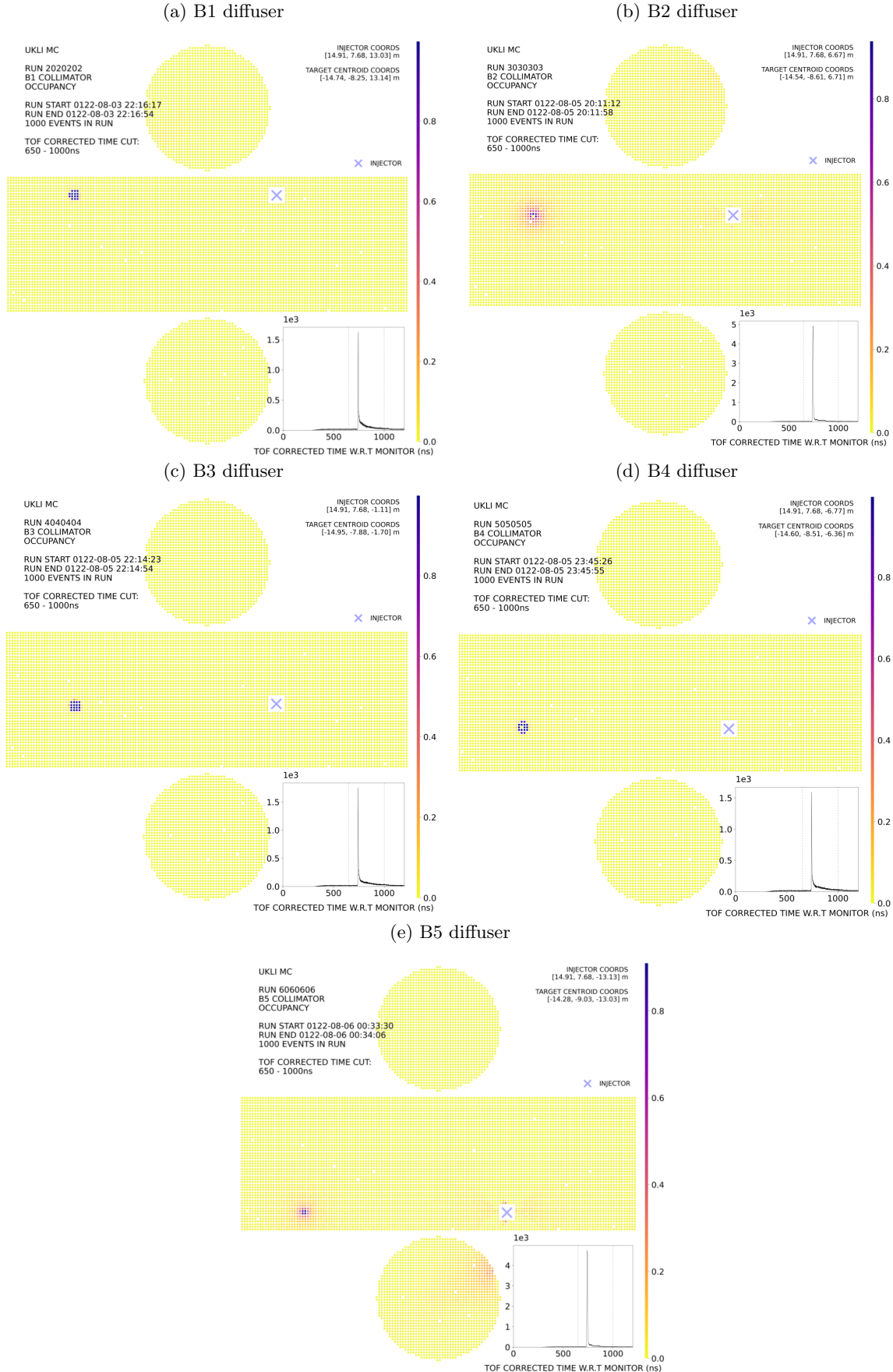


Figure A.10: MC simulations of the B1 - B5 diffusers

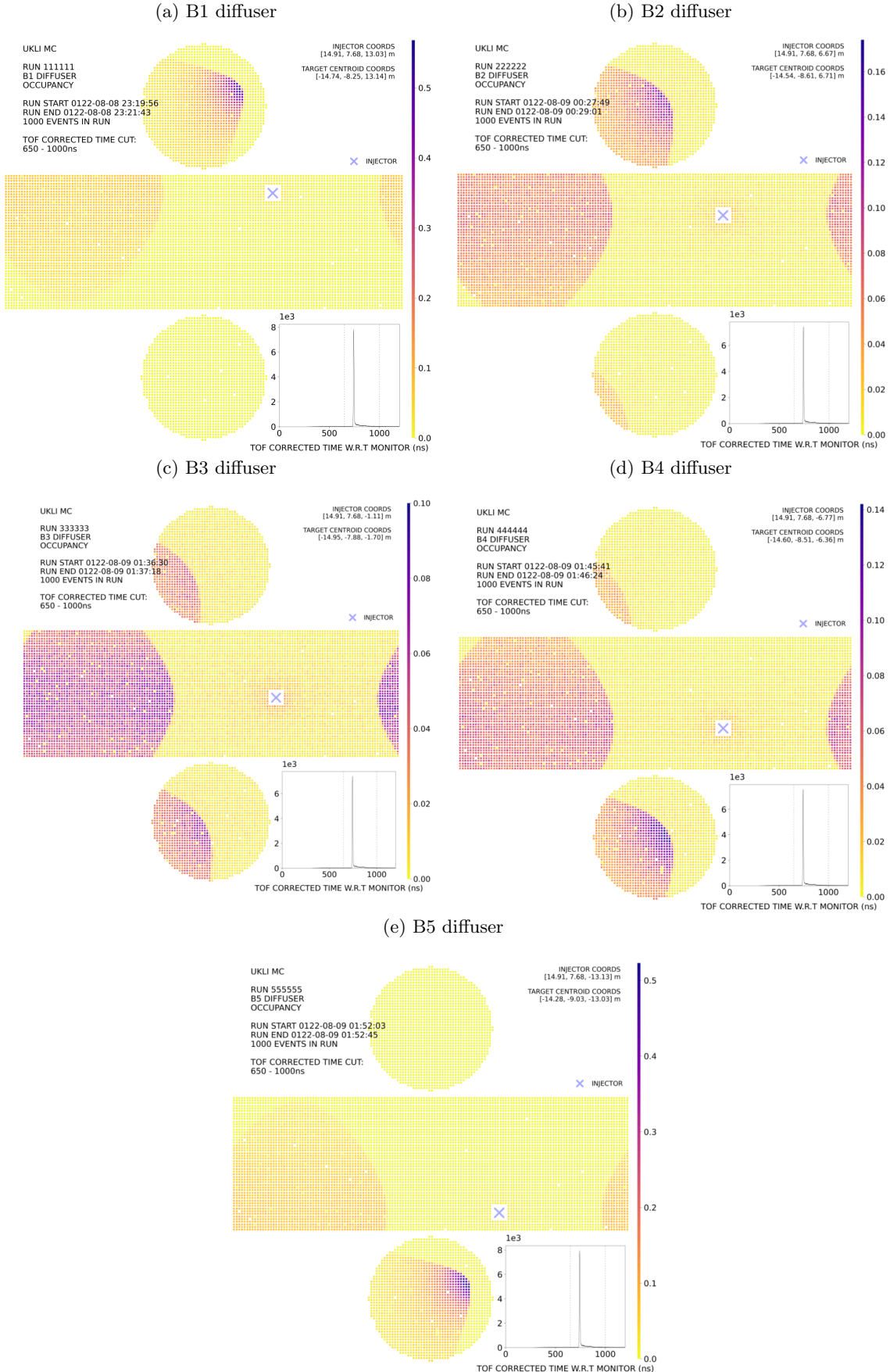


Figure A.11: Inverse CDF checks of the B1 - B5 diffusers

